# Quantum tunneling fusion reactions with impact on massive stars with STELLA

Jean Nippert

# UNIVERSITÉ DE STRASBOURG

*ÉCOLE DOCTORALE ED182 - Physique et Chimie-Physique*

**[ UMR 7178 ]**

# THÈSE présentée par :

**Jean Nippert**

soutenue le : **28 septembre 2023**

pour obtenir le grade de : **Docteur de l'université de Strasbourg**

Discipline/ Spécialité : Physique Subatomique

# Quantum tunneling fusion reactions with impact on massive stars with STELLA

**THÈSE dirigée par :**

| | |
|---|---|
| **Mme COURTIN Sandrine** | Professeure, Université de Strasbourg |

**RAPPORTEURS :**

| | |
|---|---|
| **Mme MONTAGNOLI Giovanna** | Professeure, Universita degli studi di Padova |
| **Mme REDON Nadine** | Directrice de Recherches, CNRS |

---

**AUTRES MEMBRES DU JURY :**

| | |
|---|---|
| **M BAUDOT Jérôme** | Professeur, Université de Strasbourg |
| **M HENNING Grégoire** | Chargé de recherches, CNRS |

# Acknowledgements

Je tiens tout d'abord à exprimer ma gratitude envers les membres du jury. Un grand merci aux rapporteurs Giovanna Montagnoli et Nadine Redon pour avoir accepté de rapporter et prodiguer des conseils très pertinents sur mon travail. Mes remerciements vont également à Greg Henning pour nos discussions enrichissantes et à Jerome Baudot pour l'honneur de présider le jury.

Je souhaite ensuite exprimer ma profonde reconnaissance envers Sandrine Courtin, qui a dirigé ma thèse avec confiance et soutien tout au long du processus. Marcel Heine mérite également mes remerciements pour ses conseils au cours de ces quatre années, partageant son savoir et sa méthodologie scientifique qui ont conduit aux résultats présentés dans ce manuscrit. Un merci spécial à Mohamad Moukaddam pour son accompagnement dans le domaine de l'instrumentation et de l'expérimentation.

En conclusion, je remercie l'ensemble de l'équipe pour les discussions et réflexions fructueuses sur les résultats, ainsi que le groupe DNE pour les pauses café souvent constructives.

Je tiens également à mentionner mes collègues de bureau, Margaux, Emma et Kieran, avec qui j'ai partagé ces années de thèse. Nos discussions et rires ont rendu cette période très agréable et ont donné naissance à de belles amitiés. Un merci particulier à mes amis du goshindo et à tout le dojo le samouraï, qui ont contribué activement à mon équilibre de vie.

Je souhaite également citer mes amis, toujours présents pour moi : mon partenaire de pâtes et précieux ami Rémi, mes mousquetaires Alexis, Calvin et Clément, et mes amies de longue date Marion, Mériam et Joséphine. Enfin, des remerciements spéciaux à Jérémy, mon ami de toujours, pour tous les moments divertissants qui ont égayé mon parcours, et à Maria qui m'a vaillamment soutenu durant les derniers mois intenses.

Enfin, mes plus sincères remerciements vont à ma famille, ma mère, mon père, ma sœur, et mon frère, pour m'avoir permis de poursuivre ces longues études et m'avoir soutenu tout au long de ce périple. Mes remerciements s'étendent également à l'ensemble de ma famille, trop nombreuse pour être citée individuellement : grands-parents, oncles et tantes, cousins et cousines. Merci à tous pour votre soutien indéfectible !

# Contents

# List of abreviations

- STELLA : STELlar LAboratory
- UK-FATIMA : FAst TIMing Array
- S3F : S3 type detector in the forward direction with respect to the beam.
- S3B : S3 type detector in the backward direction with respect to the beam.
- DSSSD : Double Sided Silicon Strip detector
- PMT : PhotoMultiplier Tube
- FWHM : Full Width at Half maximum
- MIDAS : Multi Instance Data Acquisition System
- EDF : Energy Density Functionnal
- CC-calculations : Coupled Channels calculations
- FHF : Frozen Hartree-Fock
- DCFHF : Density Constrained Frozen Hartree-Fock
- TDHF : Time Dependents Hartree-Fock
- DCTDHF : Density Constrained Time Dependents Hartree-Fock
- GLIB : Gigabit Link Interface Board

# Introduction

The $^{12}C + ^{12}C$ fusion reaction arose interest of many scientists around the world since the discovery of many resonances at energies above the Coulomb barrier in the early 1960s, and got even more intense after the first hint of a hindrance phenomenon from Jiang *et al.* [1] in the $^{60}Ni + ^{89}Y$ and other systems in the early 2000nd. The $^{12}C + ^{12}C$ fusion excitation function shows behaviour that is very much debated. Oscillation on the cross-section appears becoming sharper under the Coulomb barrier. Hypothesis were made about molecular states in the $^{24}Mg$ being responsible for the resonance structure observed in the cross-section. On the theoretical side, a recent work from Ebran *et al.* [2] reproduces cluster formation with Energy Density Functionnal (EDF) calculations resulting in molecular configurations in the investigated nucleus emerging naturally from first principles. Those states would be good candidate to explain the presence of sharp resonances in the fusion cross-section. The idea behind is not new and comes from Hoyle [3] in the 1950's who postulated that a state in the $^{12}C$ must exist, composed of three $\alpha$ particles, that resembles a molecule, but on nucleus scales, that might foster fusion through the triple-alpha reaction. More recently, Adsley *et al.* [4] investigated experimentally $0^+$ states in $^{24}Mg$ through $^{24}Mg(\alpha, \alpha')^{24}Mg$ and found $^{12}C + ^{12}C$ cluster-states candidate for a potential resonance at $E_{cm} = 1.5$ MeV in the $^{12}C + ^{12}C$ fusion cross-section. The $^{12}C + ^{12}C$ fusion reaction contains a lot of information on nuclear structure, but is challenging to apprehend. Up to date, no theoretical reaction model is able to reproduce the resonances observed at low energy, and most of them only reproduce the top them. However, this knowledge of this regime is crucial for stellar evolution models, which have to rely on extrapolations and make significant approximations.

Work have been done by Pignatari *et al.* [5] to highlight the impact of artifically increased or lowered cross-section on the stellar evolution and nucleosynthesis. And more specifically, Monpribat *et al.* [6] and Gasques *et al.* [7] studied the impact of the hindrance phenomenon demonstrating that the hindrance phenomenon and resonances change non-negligibly the astrophysical implications of the nuclear physics impact.

This calls for further studies of the cross-sections in the astrophysical region of interest. As for carbon fusion experiments, the cross-section in the energy region

of astrophysical interest is below the nanobarn level and thus, extremely difficult to measure in an approach directly detecting $^{12}C + ^{12}C$. Most of the experiments focus on measuring charged particles or gammas from the de-excitation of the daughter nuclei after decay of the compound nucleus $^{24}Mg$. However, at very low energies, background reactions render the measurement almost impossible with enormous uncertainties. The STELLA (STELlar LAboratory) experiment uses a coincident technique measuring charged particle and gamma at the same time allowing to achieve efficient background suppression using the gamma detection array UK-FATIMA (FAst TIMing Array) [8] and customized Double Sided Silicon Strip Detector.

The work presented here describes the measurement of the $^{12}C + ^{12}C$ fusion cross-section with the STELLA experiment at deep sub-barrier energies and focuses on the datas analysis of the 2019 experimental campaign. The first aim was to investigate energies around a resonance at $E_{cm} = 3.2$ MeV and the relative sharing into the alpha and proton channels in this region. A second goal was to probe a lower energy region close to the astrophysical region of interest, at the tail of a supposed resonance structure first measured by Spillane *et al.* [9] at $E_{cm} = 2.14$ MeV, that could have a strong effect of stellar evolution calculations.

The first chapter will discuss the motivation of the study of the $^{12}C + ^{12}C$ fusion reaction in terms of astrophysics importance and nuclear structure, with a description of the different burning phases occurring in stars. Then follows the theoretical attempt to reproduce the specific behaviour observed in the reaction at sub-barrier energies with the explanation of the hindrance phenomenon.

Then the strength of the coincidence technique and in particular the STELLA experiment will be discussed in Chapter 2, with details on the experimental device, *i.e.* the reaction chamber and the various types of detectors used: the gamma detection array, the normalization with the beam integration, the target thickness measurement and the data acquisition system. I participated to two extended data taking periods with $^{12}C$ beam on $^{12}C$ target during my PhD. One took place in 2019 for three months, with three other months in 2022, where I took the responsibility of the setup and maintenance of charged particle detection system, including classification and surveilling of the DSSSDs and pre-amplifiers. I was also deeply involved in the target thickness measurement experiment and its upgrades.

In the Chapter 3, the analysis of the data provided by the experiment is presented, detailing the energy spectrum and specific timing features of the coincidence experiment. After the analysis, the event selection and the resulting cross-section are discussed in Chapter 4. The $S$-factors are finally presented and the results in the energy ranges investigated are discussed, along with the astrophysical impact of low energy resonances, hindrance and alpha-proton decay-channel branching.

# Chapter 1

# $^{12}C + {}^{12}C$ : Impact on stellar evolution and hindrance phenomenon

Stars are the objects in the universe that create the surrounding elements. As the Big-Bang generated a universe mostly composed of hydrogen, helium, and lithium, to generate the composition of the universe that can be observed today, those initial elements have to be transformed. To better understand the evolution, the closest observable available is the sun. It is composed of 73% if hydrogen, 25% of helium and 2% of heavier elements [10]. This chapter will cover the formation of a star, overview the most important burning phases and then focus on the nuclear physics aspects of stellar evolution more specially for the $^{12}C + {}^{12}C$ fusion reaction. The resonant structures of the $^{12}C + {}^{12}C$ fusion cross-section will be discussed as well as the hindrance phenomenon which is observed in most of the medium-heavy fusion reaction systems, but still debated for lighter nuclei systems like the $^{12}C + {}^{12}C$.

## 1.1 Stellar evolution

### 1.1.1 Formation of stars

Stars are formed by gravitational contraction of a gas cloud in the interstellar medium. Inside the cloud, the temperature $T$ and the density $\rho$ are not fully homogeneous. It means that gradients of pressures inside the cloud render it gravitationally unstable. Eventually, the gravitation overcomes the pressure of internal forces and the cloud starts collapsing. Three phases of the formation of the star can be identified, making the pressure going from $10^{-23}$ g.cm$^{-3}$ to an average core density of 150 g.cm$^{-3}$ (value of the sun). The first phase corresponds to the contraction and fragmentation of the cloud under its own gravitation. It is the pre-stellar phase, the temperature remains globally constant due to a cooling of the dust grains. Then follows the proto-stellar

phase, with an increase of the pressure inside the central core until the fast contraction and the fragmentation stop to reach a hydrostatic equilibrium. During the following pre-main sequence phase, the evolution from the proto-star to the main sequence star is marked by accreting matter from the interstellar environment, dust and gas, until the temperature and the pressure are sufficient to ignite hydrogen fusion [11].

When hydrogen is ignited, it will create helium with a $Q$-value of $Q_{4^1\mathrm{H}\rightarrow{}^4\mathrm{He}} = 26.731$ MeV. This energy released inside the star increases the temperature until it reaches a new hydrostatic equilibrium (Eq. 1.1). It can be described with the pressure in a shell between a radius $r$ and $r + \mathrm{d}r$ where $\mathrm{d}r$ is an infinitesimal distance. The difference of pressure $\mathrm{d}P$ can be described as :

$$\frac{\mathrm{d}P}{\mathrm{d}r} = -\frac{GM_r}{r^2}\rho, \tag{1.1}$$

where $\rho$ is the density, $G$ the gravitational constant and $M_r$ is the mass inside a sphere of a radius $r$ [11]. The energy loss through radiation is given by the luminosity :

$$\frac{\mathrm{d}L(r)}{\mathrm{d}r} = 4\pi r^2 \rho(r)\epsilon(r), \tag{1.2}$$

where $\mathrm{d}L(r)$ is the energy loss through emission of light and $\epsilon(r)$ the energy rate function at the radius $r$ of the star. After the hydrogen burning phase, the pressure generated by reactions decreases and the star starts contracting, until the helium phase starts and a new equilibrium establishes. This process continues for the different burning phases depending on the mass of the stars.

Stars can be categorized by luminosity and surface temperature in the Hertz-Sprung-Russell diagram (Figure 1.1). More massive the stars are, the higher is their surface temperature and luminosity during the main sequence. The inner temperature also increases with the mass, and it is the reason massive stars will more likely access to advanced burning phases, like carbon burning and oxygen burning.

### 1.1.2 Reactions in stars

Inside stars, the energy of particles comes from thermal motion following a Maxwell-Boltzmann distribution given by the temperature of the shell. The distribution of the velocity of the particles can be described by the formula :

$$\Phi\left(\nu_i\right) = 4\pi\nu_i^2 \left(\frac{m_i}{2\pi k_\mathrm{B} T}\right)^{3/2} \exp\left(-\frac{m_i \nu_i^2}{2k_\mathrm{B} T}\right), \tag{1.3}$$

with $m_i$ and $\nu_i$ the mass and the velocity of the nucleus $i$, respectively, $k_\mathrm{B}$ the Boltzmann constant and $T$ the plasma temperature. This energy is low on nuclear

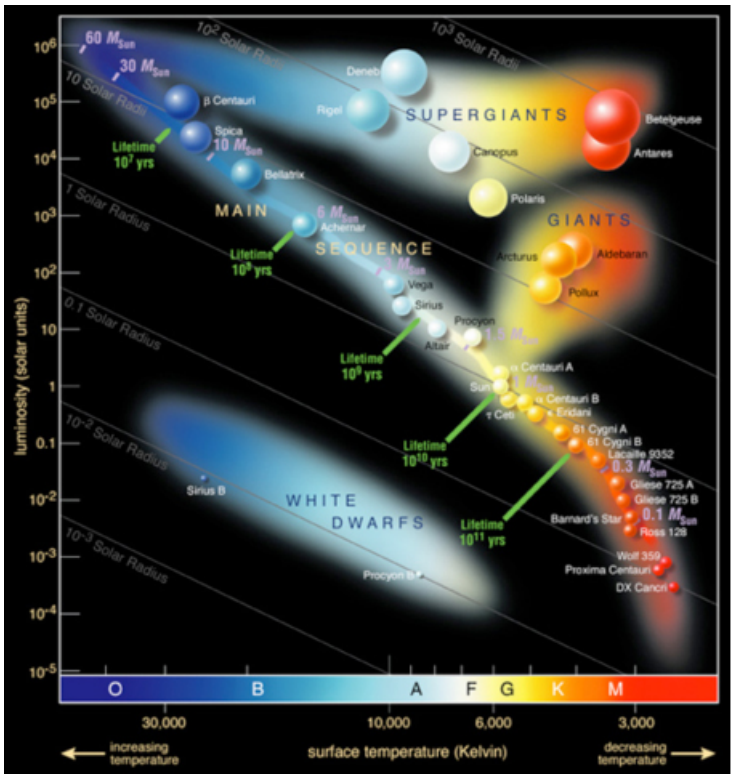


Figure 1.1: Hertzsprung-Russell diagram arranging the stars according to their surface temperature and luminosity ($x$-axis and $y$-axis, respectively) [12].

scales, and for most reactions in stars the energy is not high enough to surpass the Coulomb repulsion between the nuclei,

$$U_{\text{Coulomb}} = k\frac{Z_1 Z_2}{r_a}, \tag{1.4}$$

with $k$ the Coulomb constant, $Z_1$ and $Z_2$ the electric charge of the two nuclei involved in the reaction and $r_a$ distance between the nuclei. Thus, a fusion reaction can happen only by quantum tunneling.

Figure 1.2 shows the resulting potential for nuclear reactions (red curve) *versus* the distance with the three main contributions. The nuclear potential is short ranged (in dashed black), whereas the centrifugal and Coulomb barriers extend significantly further (dashed blue and green, respectively). The red curve shows that before falling into the attractive potential well from the attractive nuclear force, the particle have to face a barrier generated mainly by the Coulomb repulsion. The shape of the barrier and thus the probability of quantum tunneling through it, is strongly dependent on the studied reaction.

The effective energy at which fusion in stars occurs can be described by the Gamow

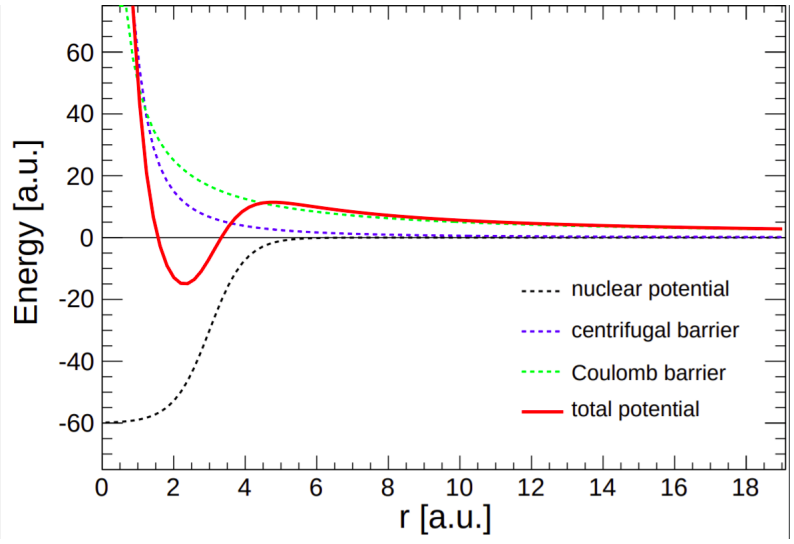


Figure 1.2: Effective potential for nuclear reactions with the three contributions:, nuclear potential, centrifugal barrier and Coulomb barrier.

peak. Figure 1.3 is a scheme that shows three curves relating a probability *versus* the energy. The blue one represents the energy distribution of the particles in the star's shell involved in the burning phase considered, the red one represents the probability of tunneling through the barrier. The Gamow peak is the convolution of the two previous contributions. The Gamow energy is the mean energy associated to the Gamow peak with a characteristic width that defines the energy interval (Gamow window) where most of the reactions of a certain nature occur in stars. The Gamow window depends on the mass of the star, its inner temperature and the type of reaction involved in the burning phase.

### 1.1.3 Burning phases

#### Hydrogen burning

The first burning phase in stars, the main sequence, corresponds to hydrogen burning. It transforms four $^{1}$H nuclei into on one $^{4}$He Nucleus. There are multiple steps in the consumption of hydrogen, represented in three pp (proton-proton) chains (see Table 1.1).

The temperature will mostly define which chain is active. The pp1 mostly happens for temperatures $T < 18$ MK while the pp2 and pp3 occurs at temperature $T = 18$-25 MK and $T > 25$ MK, respectively. As an example, the Sun's energy is produced at around 90% by the pp1 chain [13]. Looking at the different reactions of the chains, the first two are identical for all chains, transforming three $^{1}$H nuclei into a $^{3}$He nucleus.

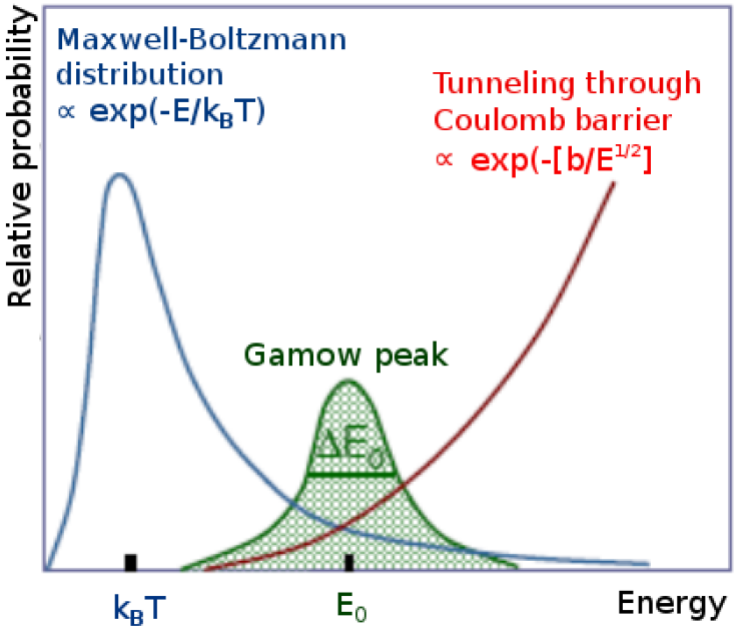


Figure 1.3: Scheme of the relative probability *versus* the energy, with the Maxwell-Boltzmann distribution of the particle energy inside stars in blue and in red the probability of tunneling through the Coulomb barrier. The green curve is their convolution, defining the energy region where most of the reactions occur in stars, the so called Gamow window.

Table 1.1: Three proton-proton chains are displayed in the Table, describing the different steps with the first one on the top and the last one on the bottom [13].

| pp1 chain | pp2 chain | pp3 chain |
|---|---|---|
| p(p,$e^+\nu$)d | p(p,$e^+\nu$)d | p(p,$e^+\nu$)d |
| d(p,$\gamma$)$^3$He | d(p,$\gamma$)$^3$He | d(p,$\gamma$)$^3$He |
| $^3$He($^3$He,2p)$\alpha$ | $^3$He($\alpha$,$\gamma$)$^7$Be | $^3$He($\alpha$,$\gamma$)$^7$Be |
| | $^7$Be($e^-$,$\nu$)$^7$Li | $^7$Be(p,$\gamma$)$^8$B |
| | $^7$Li(p,$\alpha$)$\alpha$ | $^8$B($\beta^+\nu$)$^8$Be |
| | | $^8$Be($\alpha$)$\alpha$ |

The first step not only relies on nuclear and electromagnetic forces, but also on the weak force through a process that resembles $\beta$-decay transforming a proton into a neutron contrasting most of the other stellar fusion reactions. Thus, the absolute cross-section is limited by the weak interaction and is low.

To take again the example of the Sun, the main sequence lasts around nine billion years. For the pp1 chain, the last step consumes two $^3$He nuclei to release an $\alpha$ and two protons, while for the two other chains, it consumes an alpha at the third step to release two alphas at the end. It means that the surrounding medium has to be already $^4$He enriched [13].

Most of the stars also contain heavier elements such as carbon, nitrogen or oxygen, coming from earlier stars rejecting a part of the elements created at the end of its life. Even in low amount compared to the hydrogen and helium, those elements can be responsible for a non-negligible amount of energy released to the plasma [13]. They act as catalysts transforming four hydrogen nuclei into one helium nucleus. The processes are called CNO (Carbon Nitrogen Oxygen) cycles and are described in the Table 1.2. The amount of heavy elements involved in the processes stays constant once an equilibrium is reached. Depending on the mass of the star and the temperature of the shell where the reactions occur, a CNO cycle gets more favored than a pp-chain. As the Coulomb barrier is wider for reactions in the CNO cycles than for pp-chains, they are acting more efficiently only at higher temperatures. As an example, the CNO1 cycle will release more energy into the star than the pp1-chain when the temperature exceeds 20 MK [13].

Table 1.2: Four CNO-cycles are displayed in the Table, describing the different steps with the first one on the top and the last one on the bottom [13].

| CNO1 | CNO2 | CNO3 | CNO4 |
|---|---|---|---|
| $^{12}$C(p,$\gamma$)$^{13}$N | $^{14}$N(p,$\gamma$)$^{15}$O | $^{15}$N(p,$\gamma$)$^{16}$O | $^{16}$O(p,$\gamma$)$^{17}$F |
| $^{13}$N($\beta^+\nu$)$^{13}$C | $^{15}$O($\beta^+\nu$)$^{15}$N | $^{16}$O(p,$\gamma$)$^{17}$F | $^{17}$F($\beta^+\nu$)$^{17}$O |
| $^{13}$C(p,$\gamma$)$^{14}$N | $^{15}$N(p,$\gamma$)$^{16}$O | $^{17}$F($\beta^+\nu$)$^{17}$O | $^{17}$O(p,$\gamma$)$^{18}$F |
| $^{14}$N(p,$\gamma$)$^{15}$O | $^{16}$O(p,$\gamma$)$^{17}$F | $^{17}$O(p,$\gamma$)$^{18}$F | $^{18}$F($\beta^+\nu$)$^{18}$O |
| $^{15}$O($\beta^+\nu$)$^{15}$N | $^{17}$F($\beta^+\nu$)$^{17}$O | $^{18}$F($\beta^+\nu$)$^{18}$O | $^{18}$O(p,$\gamma$)$^{19}$F |
| $^{15}$N(p,$\alpha$)$^{12}$C | $^{17}$O(p,$\alpha$)$^{14}$N | $^{18}$O(p,$\alpha$)$^{15}$N | $^{19}$F(p,$\alpha$)$^{16}$O |

### Helium burning

When the hydrogen fuel is exhausted, the star contracts and the temperature in the core increases to the point where helium burning occurs. This balances the gravitational contraction to reach a new equilibrium. Helium is the second most abundant chemical element in the universe and $^4$He burning occurs through three main reactions. The first one is the triple-$\alpha$ reaction ($\alpha(\alpha\alpha,\gamma)^{12}$C). It starts with the reaction,

$$^4\text{He} +^4 \text{He} \leftrightarrow^8 \text{Be}, \tag{1.5}$$

with a $Q$-value of -91.84 $\pm$ 0.04 keV, but $^{8}$Be is unstable with a half-life of $T_{1/2} = 8.2 \times 10^{-17}$s and decays back. At equilibrium the creation and the decay rates are equals, and a small amount of $^{8}$Be allows another $\alpha$-particle to create the $^{12}$C through the reaction,

$$^{8}\mathrm{Be}(\alpha,\gamma)^{12}\mathrm{C}, \tag{1.6}$$

with a $Q$-value of 7366.57 $\pm$ 0.04 keV. The triple-alpha process is also of interest regarding nuclear structure questions with the so called "Hoyle" state. It will be discussed in the section 1.2. As $^{8}$Be is unstable, the two reaction of the triple-$\alpha$ (Equations 1.5 and 1.6) reaction were not directly measured yet, but investigated by time reversed process. The triple-$\alpha$ reaction, with subsequent gamma decay, generates $^{12}$C in the stellar medium, allowing the next helium burning reaction to occur,

$$^{12}\mathrm{C}(\alpha,\gamma)^{16}\mathrm{O}, \tag{1.7}$$

consuming the $^{12}$C created by the triple-$\alpha$ reaction.

Figure 1.4 shows the abundance of the chemical elements in the solar system and the ratio of the abundances $N(^{12}\mathrm{C})/N(^{16}\mathrm{O}) \approx 0.4$ meaning that only a fraction of $^{12}$C created is formed into $^{16}$O.

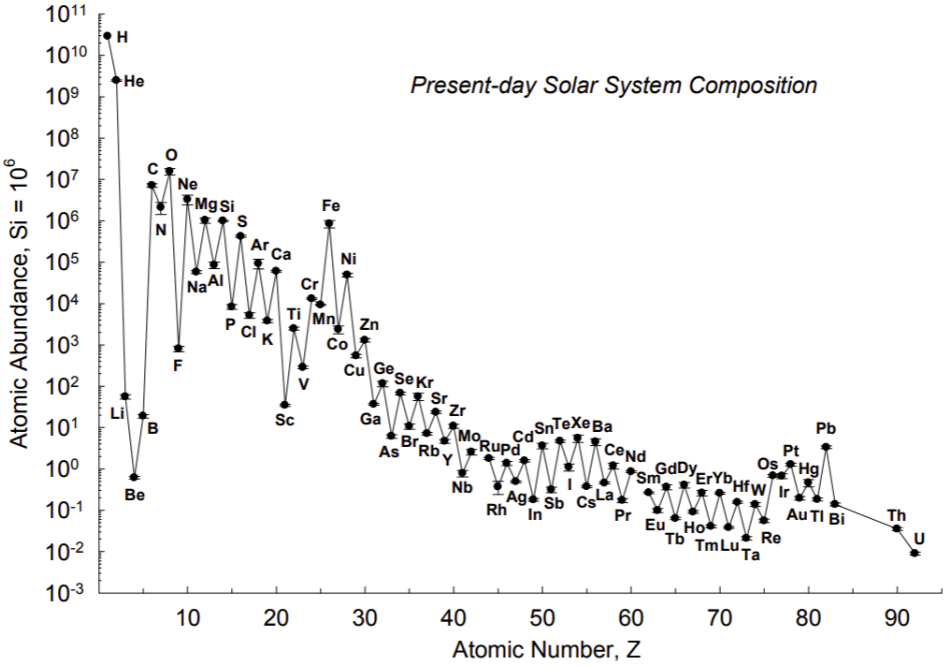


Figure 1.4: Abundance of the chemical elements in the solar system as a function of the atomic number [14].

With the typical temperature of the He-Burning of $T = 0.2$ GK, the Gamow peak for

the $^{12}C(\alpha,\gamma)^{16}O$ reaction is centered around $E_0 \approx 315$ keV with a width $\Delta_{E_0} = 170$ keV. Figure 1.5 shows the energy levels of the nuclei involved in the triple-$\alpha$ reactions and the $^{12}C(\alpha,\gamma)^{16}O$ reaction. Considering the Gamow energy, the excitation reached in $^{16}O$ is around $E_{ex} \approx 7.4$ MeV. The absence of states in this energy region makes the non-resonant radiative capture cross-section of the alpha by the $^{12}C$ more difficult. Lower lying excited states at $E_{ex} = 7117$ keV ($J^\pi = 1^-$) and $E_{ex} = 6917$ keV ($J^\pi = 2^+$) contribute slightly on the tail of the resonances [13].

Experimentally, the lowest energy investigated for the reaction cross-section measurement is at $E_{cm} = 1000$ keV, because vanishing cross-sections make the measurement yet impossible in the Gamow window. The cross-section of the $^{12}C(\alpha,\gamma)^{16}O$ reaction is extrapolated through theoretical calculations to $\sigma_{^{12}C(\alpha,\gamma)^{16}O} = 10^{-14}$ mb [13]. This explains why a significant amount of $^{12}C$ is left at the end of the helium burning phase.

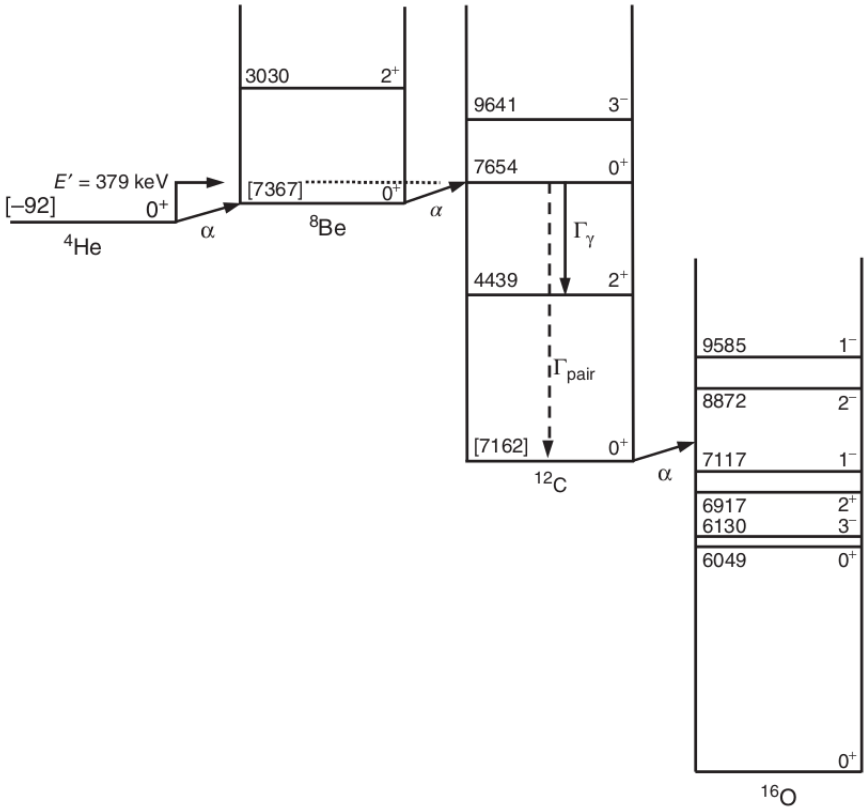


Figure 1.5: Energy levels with excitation energy and spin-parity of the nuclei involved in the Triple-$\alpha$ and the $^{12}C(\alpha,\gamma)^{16}O$ reactions [13].

If the inner temperature is high enough, the next reaction, is burning oxygen with the helium through the reaction:

$$^{16}\mathrm{O}(\alpha,\gamma)^{20}\mathrm{Ne}. \tag{1.8}$$

For the same reason than the $^{12}\mathrm{C}(\alpha,\gamma)^{16}\mathrm{O}$ reaction, it would be expected that most of the oxygen would get destroyed. However, as the oxygen is the third most abundant element in the solar system; the reaction must be slow. For the typical temperature of helium burning $T = 0.2$ GK, a Gamow window $E_0 \pm \Delta/2 = 390 \pm 90$ keV, and a $Q$-value of $Q = 4730$ keV, three excited states in the $^{20}$Ne can be populated. The first one is at $E_{\mathrm{ex}} = 4967$ keV with a $J^\pi = 2^-$. This parity is unatural with respect to the reaction and thus, the state cannot be populated. Two resonant states are at $E_{cm} = 893$ keV [15] and $E_{cm} = -482$ keV with respective energies and parities: $E_{ex} = 5621$ keV with $J^\pi = 3^-$ and $E_{ex} = 4967$ keV $J^\pi = 4^+$, but they are far from the Gamow window, and as they are formed *via* incoming $f$-waves ($l = 3$) ang $g$-waves ($l = 4$), they face a strong centripetal barrier. With those arguments, the cross-section is expected to be low. However, the lack of experimental data at energies below $E_{\mathrm{cm}} = 1000$ keV makes the reaction rates rely on theoretical model calculations [13].

### Carbon burning

At the end of helium burning, the most abundant nuclei in the core of the star are $^{16}$O and $^{12}$C. Again the core of the star contracts gravitationally and its temperature rises. The next burning phase to occur is carbon burning. It mainly occurs through the $^{12}$C + $^{12}$C fusion reaction. However, the $^{12}$C + $^{12}$C reaction face a Coulomb barrier of 6.6 MeV. Thus, not all stars might be able to start the burning phase, it is estimated that the minimal mass to start it is around 9 $M_\odot$ [13]. Experimentally, cross-section measurements at astrophysical energies are very challenging. However, its measurement is necessary as the knowledge of it can drastically change how astrophysicists understand and compute star evolution and element abundances through the nuclear rates and the impact of resonances in the cross-sections in the Gamow window, but also the limit mass of stars that can start the carbon burning phase.

The $Q$-value in $^{12}$C + $^{12}$C fusion reaction is around $Q = 14$ MeV, leading to high excitation levels in $^{24}$Mg. The $^{12}$C + $^{12}$C fusion reaction has three exit channels:

$$^{12}\mathrm{C}(^{12}\mathrm{C},p)^{23}\mathrm{Na}, \tag{1.9}$$

$$^{12}\mathrm{C}(^{12}\mathrm{C},\alpha)^{20}\mathrm{Ne}, \tag{1.10}$$

$$^{12}\mathrm{C}(^{12}\mathrm{C},n)^{23}\mathrm{Mg}, \tag{1.11}$$

with respective $Q$-values $Q_p = 2241$ keV, $Q_\alpha = 4617$ keV and $Q_n$ = -2599 keV.

The excitation energy reached in $^{24}$Mg is very high. Thus, the energy is more efficiently released by evaporating a light particle than through $\gamma$-ray emission, making the $^{12}$C($^{12}$C, $\gamma$)$^{24}$Mg reaction negligible. The evaporated particles are released into the stellar medium.

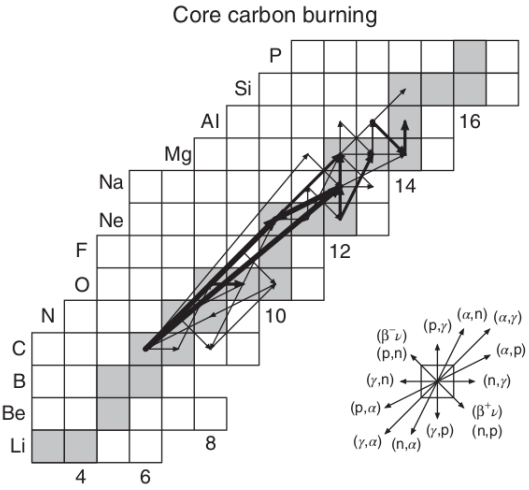


Figure 1.6: Partial nuclear chart showing the nuclei with the number of protons in the $y$-axis and the number of neutron in the $x$-axis. The width of the arrows indicate the net abundance flows integrated over the carbon burning phase for a Temperature of $T = 0.9$ GK and a core density of $\rho = 10^5$ g/cm$^3$, typical for 25 $M_\odot$ stars [13].

As the temperature of C-burning phase is between $T = 0.6$ and $T = 1.0$ GK, the light particles emitted by $^{12}$C + $^{12}$C fusion reaction will rapidly be consumed in secondary reactions. Figure 1.6 shows the main and secondary reactions in the core of the star for a temperature of $T = 0.9$ GK and a core density of $\rho = 10^5$ g/cm$^3$, typical for 25 $M_\odot$ stars [13]. It is represented on a partial chart of nuclei. The width of the arrows indicates the net abundance of the elements transformed during the carbon burning phase, i.e. the difference of the abundances after and before the burning phase. It shows that the two main exit channels of the $^{12}$C + $^{12}$C fusion reaction are the proton and the alpha channels. The main reason is that the neutron channel has a negative $Q$-value $Q = -2599$ keV and thus the reaction is forbidden at this energy. For a 25 $M_\odot$ star, the Gamow peak is around $E_0 = 2200$ keV so only the upper tail of the Gamow peak will participate in the neutron channel.

Figure 1.7 shows the chemical evolution of a 25 $M_\odot$ star with a core density of $\rho = 10^5$ g/cm$^3$ and a core temperature of $T_{\text{core}} = 0.9 \times 10^9$ K during the carbon burning phase. The width of the arrows in Figure 1.6 are related to this graph. A significant increase of the $^{20}$Ne and $^{23}$Na can be observed. The $^{24}$Mg also shows as strong increase.

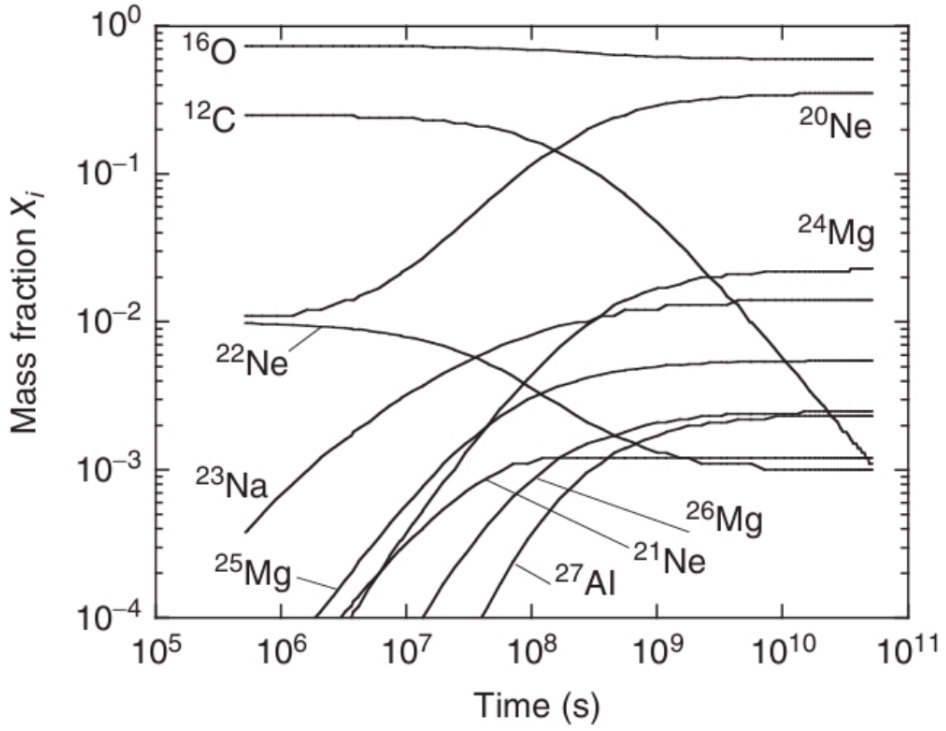


Figure 1.7: Chemical composition evolution of a 25 $M_\odot$ star with a core density of $\rho = 10^5$ g/cm$^3$ and a core temperature of $T_{\rm core} = 0.9 \times 10^9$ K during the carbon burning phase. [13]

However, the reaction $^{12}$C($^{12}$C, $\gamma$)$^{24}$Mg is not favorable due the excitation reached in the $^{24}$Mg ($\geq$ 14 MeV). But the secondary reactions $^{23}$Na$(p,\gamma)^{24}$Mg and $^{20}$Ne$(\alpha,\gamma)^{24}$Mg are mostly responsible for the production of $^{24}$Mg during the burning phase [13].

The $^{22}$Ne is releasing neutrons in the stellar medium *via* the $^{22}$Ne$(\alpha,n)^{25}$Mg reaction. The neutrons are not repelled by the electromagnetic forces, thus they are not sensitive to the Coulomb barrier, and then will start a series of secondary reactions producing heavier isotopes of the chemical elements. In Figure 1.6, the horizontal arrows show neutron capture,(n,$\gamma$) reactions. Nuclei in the core will capture the neutrons as for example the $^{20}$Ne or the $^{23}$Na but also products of the helium burning phase as $^{12}$C into $^{13}$C and the $^{16}$O into $^{17}$O. The last one can explain the small decrease of the $^{16}$O during the carbon burning phase [13].

## 1.2 Fusion and the structure of $^{24}$Mg

### 1.2.1 $^{12}$C + $^{12}$C fusion reaction

As discussed in the Section 1.1.3, the main reaction during the carbon burning phase is the $^{12}$C + $^{12}$C fusion reaction. It has three exit channels at astrophysical energies :

$$^{12}\mathrm{C} + ^{12}\mathrm{C} \rightarrow ^{24}\mathrm{Mg}^* \rightarrow ^{20}\mathrm{Ne} + \alpha + \gamma \quad (Q_\alpha = 4.62\mathrm{MeV}), \tag{1.12}$$

$$^{12}\mathrm{C} + ^{12}\mathrm{C} \rightarrow ^{24}\mathrm{Mg}^* \rightarrow ^{23}\mathrm{Na} + p + \gamma \quad (Q_p = 2.24\mathrm{MeV}), \tag{1.13}$$

$$^{12}\mathrm{C} + ^{12}\mathrm{C} \rightarrow ^{24}\mathrm{Mg}^* \rightarrow ^{23}\mathrm{Mg} + n + \gamma \quad (Q_n = -2.6\mathrm{MeV}). \tag{1.14}$$

The equation 1.12, 1.13 and 1.14 will be called alpha, proton and neutron channel, respectively. At astrophysical energies, the $^{24}$Mg compound nucleus is populated at energy levels above 14 MeV. To release the excitation energy, it evaporates particles (alpha, protons, neutrons). The daughter nucleus can also be in an excited state and emit a gamma ray to propagate in its ground state.

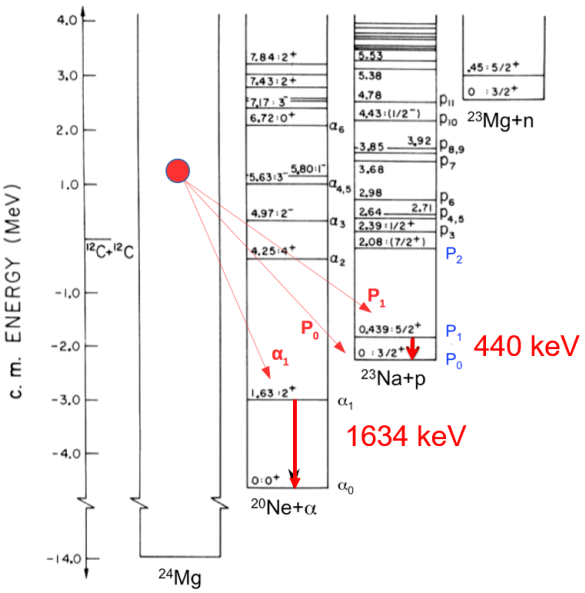


Figure 1.8: Energy level diagram showing the decay of the $^{24}$Mg excited after a $^{12}$C + $^{12}$C fusion reaction at ≈ 1.3 MeV in the center of mass system, modified from Nuclear data Tables.

Figure 1.8 shows the energy diagram for the $^{24}$Mg decay after $^{12}$C + $^{12}$C fusion reaction at ≈ 1.3 MeV in the center of mass system. This energy is estimated to be

the lower limit of the Gamow window for 25 $M_\odot$ star [13]. Figure 1.8 also shows the excitation energy in the daughter nuclei. The most interesting ones in the context of this work are the first excited states, with a 1634 keV and a 440 keV de-excitation gamma energy, respectively for the $^{20}$Ne and $^{23}$Na. The associated particle energy in the laboratory system can be obtained using kinematic calculations (eq. 1.15 [16]), and depends on the laboratory angle $\theta_3$ as:

$$E_3(\theta_3) = \frac{A_1 A_3 E_i}{A_2\,(A_1 + A_2)} \frac{\left[\gamma_3 \cos(\theta_3) \pm \left(1 - \gamma_3^2 \sin^2(\theta_3)\right)^{1/2}\right]^2}{\gamma_3^2}, \tag{1.15}$$

with $E_i$ the center of mass energy, $A_1$ and $A_2$ the mass number of the interacting nuclei, $A_3$ the mass number of the detected product of the reaction and $\gamma_3 = \left(\frac{A_1 A_3}{A_2 A_4} \frac{E_i}{E_i + Q}\right)^{1/2}$ with $Q$ the $Q$-value, taking into account the excitation level of the daughter nuclei.

### 1.2.2 Fusion cross-section

The detailed knowledge of the alpha and protons energies serves identifying the reaction channel, monitoring the detectors performance over time (drift, degrading etc...).

The differential cross-sections $\frac{d\sigma}{d\Omega}$ is computed through equation (1.16), where $S$ is the number of counts in the exit channel measured, $I$ the number of beam particles measured from the integrated intensity, $N_t$ the number of nuclei in the target per surface and $\Delta\Omega$ the solid angle of the detector's strip.

$$\left(\frac{d\sigma}{d\Omega}\right)_{\text{lab}} = \frac{S}{I \times N_t \times \Delta\Omega}\ . \tag{1.16}$$

The measurements have to be transformed from the laboratory frame to the center of mass frame [16]. Starting with the polar angle:

$$\theta_{\text{cm}} = \arcsin\left[\sin\theta_{\text{lab}} \left(\gamma_3 \cos\theta_{\text{lab}} \pm \left(1 - \gamma_3^2 \sin^2\theta_{\text{lab}}\right)^{1/2}\right)\right]\ , \tag{1.17}$$

where $\theta_{\text{lab}}$ is the angle in the laboratory frame, and the kinematic factor $\gamma_3 = \left(\frac{A_1 A_3}{A_2 A_4} \frac{E_i}{E_i + Q}\right)$ with $A_i$ the mass number of the different nuclei involved in the reaction ($A_1 + A_2 \rightarrow A_3 + A_4$), $E_i$ being the center of mass energy and $Q$ the Q-value of a specific final state of reaction. To transform the differential cross-section from the laboratory to the center of mass system, the following formula is used,

$$\left(\frac{d\sigma}{d\Omega}\right)_{\text{cm}} = \left(\frac{d\sigma}{d\Omega}\right)_{\text{lab}} \frac{|1 + \gamma_3 \cos\theta_{\text{cm}}|}{\left(1 + \gamma_3^2 + 2\gamma_3 \cos\theta_{\text{cm}}\right)^{3/2}}. \tag{1.18}$$

The exit channel of interest is extracted by fitting the associated peaks in the energy spectrum (see figure 3.8) with a gaussian, and a linear function is used to approximate

the background in the spectrum. Doing so, exclusive cross-sections can be extracted. The fitting of the experimental distribution can be performed with the function:

$$\left(\frac{d\sigma}{d\Omega}\right)_{\text{cm}} = \sum_{k=0}^{k_{max}} a_k P_k(\cos\theta_{\text{cm}}), \tag{1.19}$$

with $a_k$ the adjusted coefficients and $P_k$ the Legendre polynomial for the order $k$. The total cross-section for one excited state will be determined with $\sigma^i_{\text{tot}} = 4\pi a_0$, i.e. a constant integrated over all the solid angle. The total cross-section for the alpha/proton channel is the sum of the cross-sections of all excited states available at the energy of the reaction. If they cannot all be extracted from experimental data (background, energy threshold, energy resolution), a branching correction has to be applied,

$$\sigma_{\text{tot}} = \left[\sum^{i} \sigma^i_{\text{tot}}\right] \Gamma, \tag{1.20}$$

where $\sigma^i_{\text{tot}}$ is the total cross-section for an excited state and $\Gamma$ is the branching correction for the missing excited states. In this work, excited states $p_1$ and $\alpha_1$ were mostly analysed and the branching correction have been extracted from that work (Becker *et al.* [17]).

The cross-section for the $^{12}$C + $^{12}$C fusion reaction shows interesting structures that seem to be correlated in all the exit channels. Figure 1.9 shows the intensity for all the main exit channels of the $^{12}$C + $^{12}$C fusion reaction in arbitrary units as a function of the energy. Oscillations can be observed in the entire energy range measured, but the effect becomes pronounced under the Coulomb barrier, represented by the arrow at 6.6 MeV [18]. Between 5 and 7 MeV, the resonant structures look correlated in all the channels. The width of the resonances indicates that they might be linked to molecular states in the $^{24}$Mg [18].

### 1.2.3 Molecular states

The story of molecular states begins in the 1950's with F. Hoyle [3] who predicted an excited state in the $^{12}$C. The Gamow energy for the $^{8}$Be$(\alpha,\gamma)^{12}$C reaction at the typical temperature of helium burning ($T \approx 10^8$ K) is between 200 and 230 keV. Considering it and the $Q$-value of the reaction, there should be a state in the $^{12}$C should be around $E_{\text{ex}} = 7.6$-$7.7$ MeV, for the reaction to occur. A bit later, a $0^+$ state at $E_{\text{ex}} = 7654$ keV has been measured. The nuclear structure for this excited state is still debated [19].

Figure 1.10 shows the intrinsic one-body densities of four states computed with a Fermionic Molecular Dynamics (FDM) approach and their contribution to the Hoyle state. The densities give informations on the structure of the $^{12}$C nucleus and all those

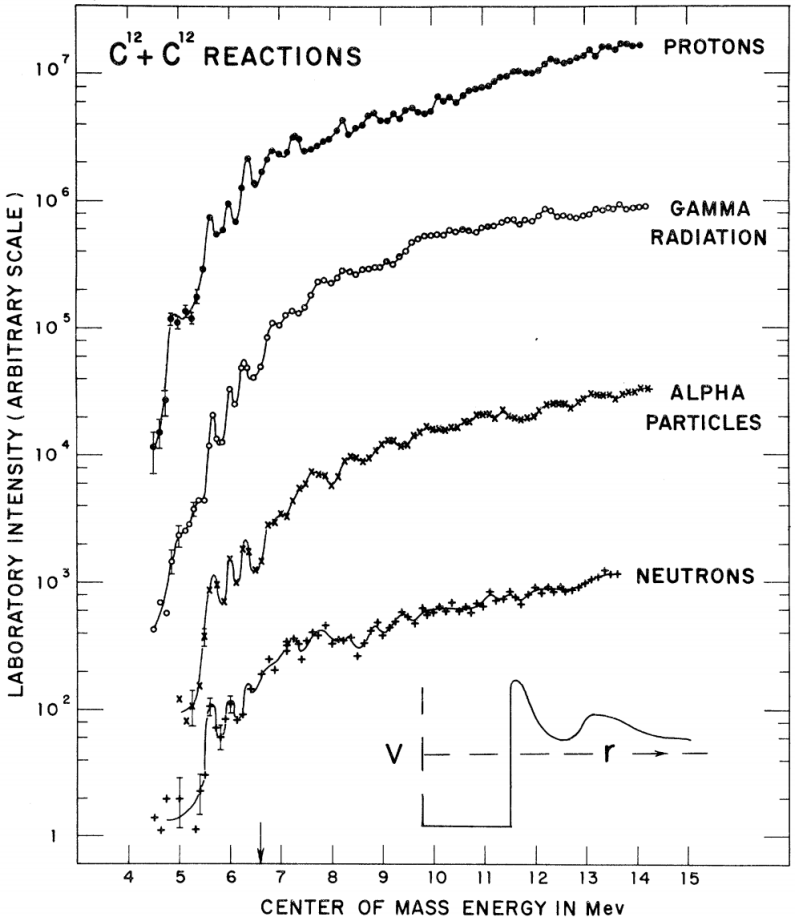


Figure 1.9: Experimental results for the population of the main exit channels of the $^{12}$C + $^{12}$C reaction in arbitrary units as a function of the energy. The arrow at 6.6 MeV indicates the Coulomb barrier. [18]

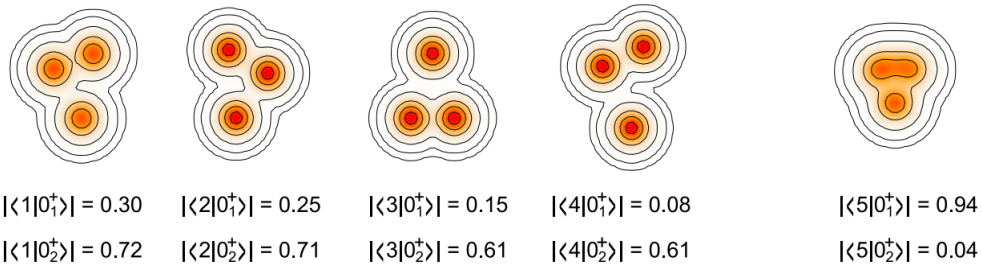


Figure 1.10: One-body densities of Fermionic Molecular Dynamics states with their amplitude for the ground state ($0_1^+$) and the Hoyle state ($0_2^+$) [19].

configurations with a triple-alpha molecular structure. Experimental works are still needed to deeply understand the shape of the Hoyle state, which is closely linked to its population and decay properties.

The fusion cross-section resonances in the $^{12}C + ^{12}C$ spectrum are linked to molecular configurations as well [4], near the Coulomb barrier with a width of $\Gamma \approx 150$ keV, which is related to the lifetime $\tau$ of the populated state in the $^{24}$Mg of $\tau \approx 4.5 \times 10^{-21}$ s, $\tau = \frac{\hbar}{\Gamma}$. The time for a nucleon to cross the nucleus at the Fermi energy is $\approx 1.1 \times 10^{-22}$ s. Thus, the lifetime of the state is sufficiently long and might be even longer, as the energy loss in the thin target ($\approx 100$ keV) restricts the energy resolution of experiments, so that the resonances might be narrower. However, it is a short time compared to the time for a nucleus to stabilize after a fusion reaction ($\approx 10^{-18}$ s). At the bottom of the Figure 1.9 is shown a potential that takes into account molecular effect in the nucleus. This effect as been studied in 1960 by Vogt [20] and a nucleus interpreted as a configuration made of a molecule of two carbon nuclei. The shape of the potential (Figure 1.9) reveals a well at outer radii believed to be generated by the two carbon molecular configuration. In such additional potential well, the fused nucleus exists as a molecular configuration, before fully fusing into $^{24}$Mg.

This kind of state is believed to exist at the threshold of the emission of the particle composing the molecular state. The best example of it are the $^{8}$Be in the triple-alpha reaction, that is unstable and disintegrates back to two alphas particles with a lifetime of $\tau = 8 \times 10^{-17}$ s, and the Hoyle state at $E_{ex} = 7.65$ MeV in the $^{12}$C previously presented [4]. This idea has been expanded to other nuclei, developing $\alpha$-cluster states, with their adjusted energy level (Ikeda *et al.* 1968)[21].

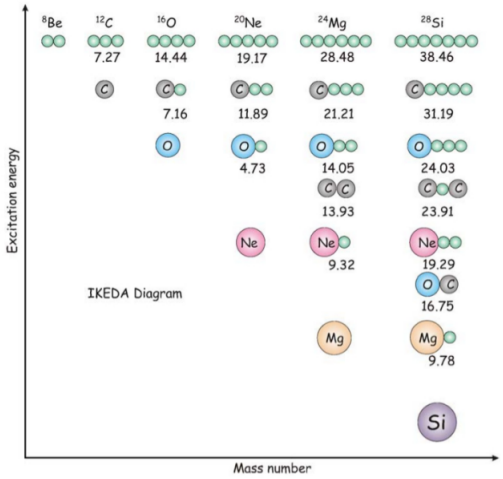


Figure 1.11: Ikeda diagram showing $\alpha$-cluster states in several nuclei with their associated energy in MeV [21].

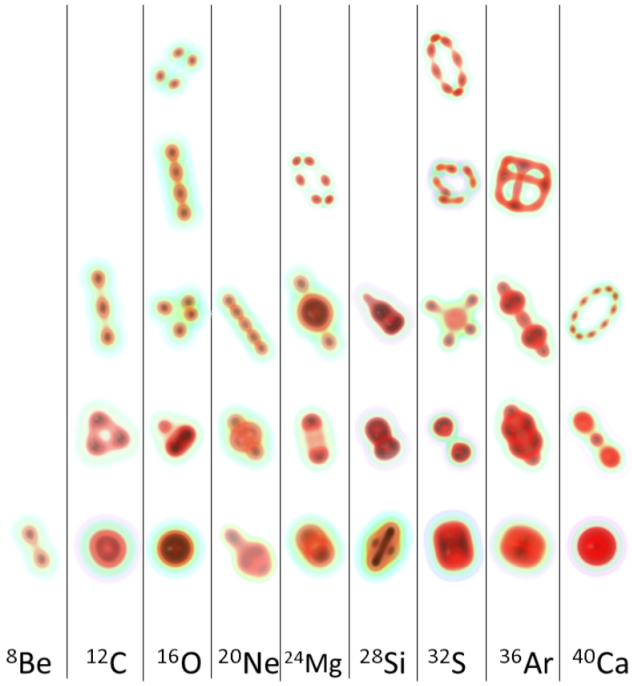


Figure 1.12: Molecular configurations in $N = Z$ nuclei computed with theory. The bottom line for each nuclei corresponds to their equilibrium configuration [21][2].

More recently, theoretical calculation using Energy Density Functional theory (EDF) derived molecular states in several nuclei from first principle calculations. Figure 1.12 shows densities of states in N = Z nuclei, where $\alpha$-clusters appear. It has been shown that a deeper binding potential is more likely to be linked to a cluster configuration as the nucleonic single-orbitals tend to be more localised [2].

Figure 1.13 shows the binding energy function of the quadrupole deformation, and density calculations are attributed to different potentials in $^{36}$Ar. The three graphs shown use different potentials (Sly4, D1S and DD-ME2 for a, b and c respectively), and the third one (c) shows deeper potential depth, with a clearer cluster configuration [2].

### 1.2.4 $^{24}$Mg Level Density

Another way to approach the resonant structure of the carbon fusion cross-section is analysing the level density in $^{24}$Mg. Comparing the trend of the $S$-Factor in the carbon fusion reactions $^{12}$C + $^{12}$C, $^{12}$C + $^{13}$C and $^{13}$C + $^{13}$C, Figure 1.14 shows the measurement, with Coupled-Channels (CC) calculations. Firstly, the $S$-factors are smooth for the $^{12}$C + $^{13}$C and $^{13}$C + $^{13}$C while the $^{12}$C + $^{12}$C $S$-factors shows the oscillations previously discussed. In the coupled channels calculations data are well

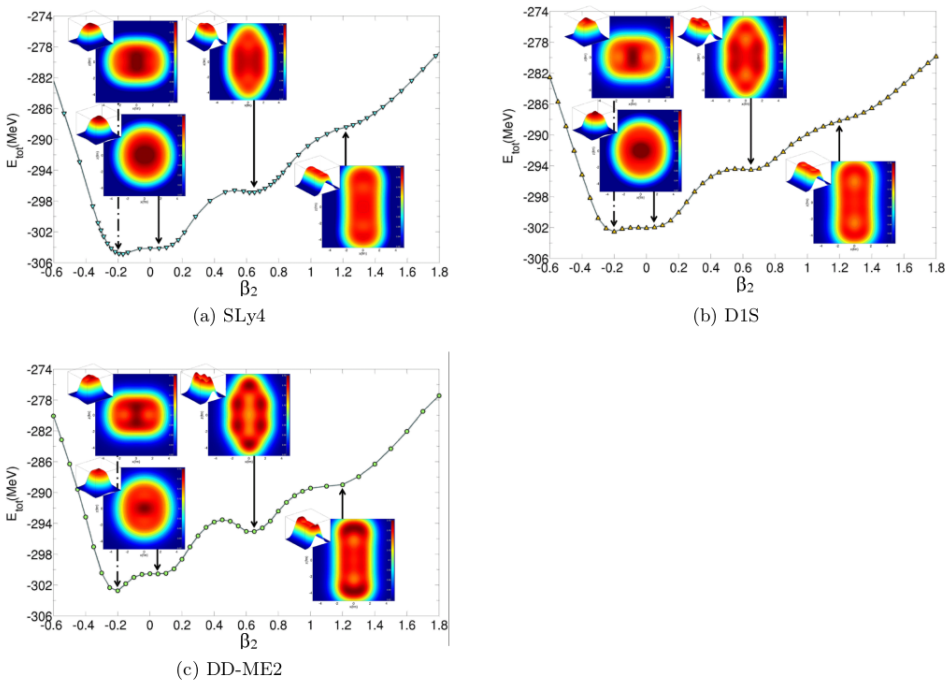


(a) SLy4

(b) D1S

(c) DD-ME2

Figure 1.13: Binding energy of the $^{36}$Ar *versus* the quadrupole deformation, the associated nuclear densities from EDF calculations are displayed [2].

reproduced for the $^{12}$C + $^{13}$C and $^{13}$C + $^{13}$C fusion reactions but only the top of the oscillations match the calculations in $^{12}$C + $^{12}$C.

A hypothesis to explain the missmatch is based on differences in the energy density levels in the $^{24}$Mg and $^{25}$Mg. Jiang *et al.* (2013 [28]) describe the spacing density level for specific spins and parity using the following equation,

$$\rho\left(U, J^{\pi}\right) = \frac{\left(2J+1\right) e^{-(J+1/2)^2/2\sigma^2}}{4\sigma^3\sqrt{2\pi}} \rho\left(U\right), \tag{1.21}$$

with $\rho = 1/D$ the level density and $D$ the spacing, $J$ the spin, $U$ the excitation energy and $\sigma^2 = 0.088aTA^{2/3}$ the spin cutoff parameter, where the nuclear temperature $T = \sqrt{U/a}$ depends on the level density parameter $a$. Then the total level density can be expressed as,

$$\rho\left(U\right) = \frac{\sqrt{\pi}}{12} \frac{\exp 2\sqrt{aU}}{a^{1/4}U^{5/4}}. \tag{1.22}$$

The function from Equation 1.22 is used in Figure 1.15 to reproduce experimental data level densities $\rho$ for the excitation energy $U$. The hypothesis investigated here is that the level spacing and the width of the levels impacts the $S$-factor (which allows to show the cross-section without the exponential decrease generated by the tunnel effect

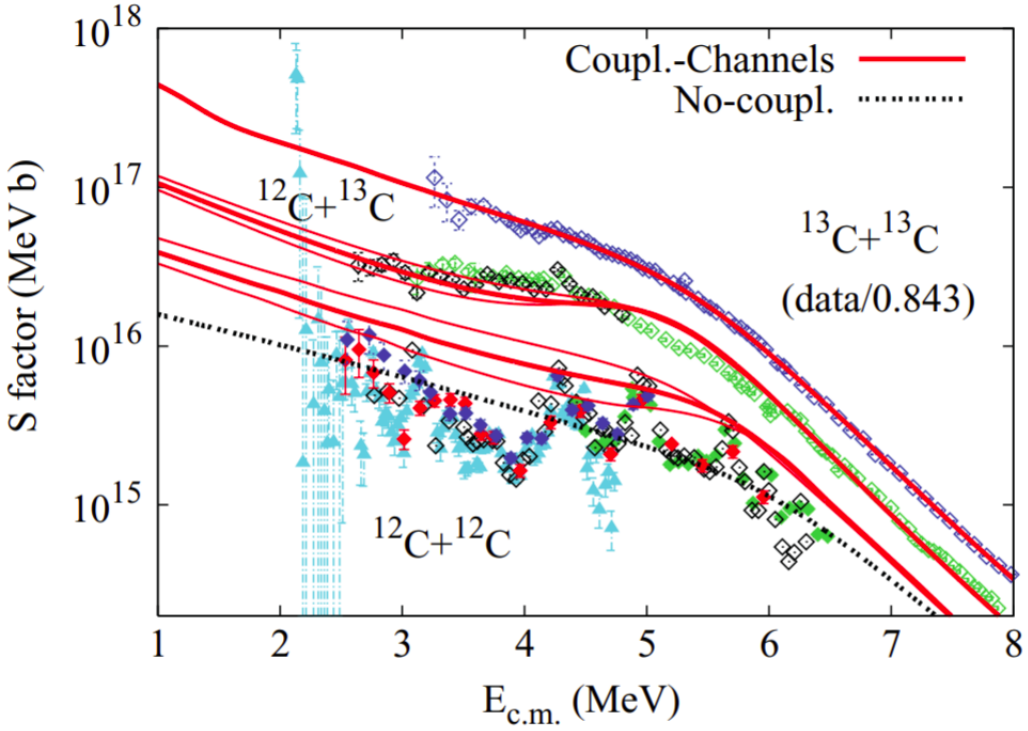


Figure 1.14: *S*-Factor *versus* the center of mass energy for $^{12}$C + $^{12}$C [22][23][24][17][9], $^{12}$C + $^{13}$C [25][26] and $^{13}$C + $^{13}$C [27] with CC-calculations [27].

when the energy decreases) and generates the resonant shape in the $^{12}$C + $^{12}$C fusion reaction that is not observed in the $^{12}$C + $^{13}$C. Figure 1.15 shows that the density level in the $^{24}$Mg is approximately three times lower than in the $^{25}$Mg. The analysis for $^{32}$S is also shown, with a lower density than in $^{25}$Mg. The $^{16}$O + $^{16}$O fusion reaction creating the $^{32}$S also exhibit resonance behaviour, but less pronounced than in the $^{12}$C + $^{12}$C fusion reaction.

The other aspect related to carbon fusion is that with two $J^{\pi}(^{12}\mathrm{C}) = 0^{+}$ nuclei in the entrance channel, only even spin states with natural parity can be populated in the compound nucleus, reducing the amount of available states. Finally, it is estimated that below 7 MeV in the center of mass system, the widths of the compound stated are smaller than the average spacing of the states [28][24]. Combined to a small *Q*-value with respect to the other carbon based reactions, those characteristics of the $^{12}$C + $^{12}$C fusion reaction make it unique with rich features in the excitation spectrum.

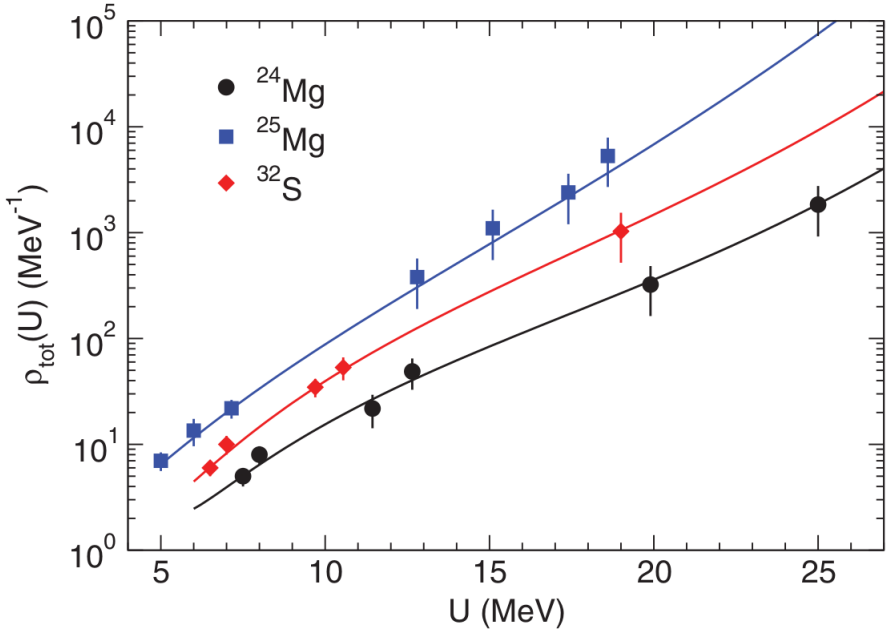


Figure 1.15: Total level densities *versus* the excitation energy $U$ in $^{24}$Mg, $^{25}$Mg and $^{32}$S [28].

## 1.3 Hindrance phenomenon

### 1.3.1 Discovery

The first hint of this phenomenon appears in the work of Jiang *et al.* in 2002 [1], where they observed cross-section at deep sub-barrier energies that were lower than the predictions of theoretical models, CC-calculations and the Wong formula [29], that described very well cross-sections in heavy ion fusion like the $^{58}$Ni + $^{58}$Ni and $^{90}$Zr + $^{92}$Zr. Figure 1.16 shows experimental data points, dots for the $^{58}$Ni + $^{58}$Ni and full triangles for the $^{90}$Zr + $^{92}$Zr Fusion reactions. The lower panel shows the ratio between experimental and theoretical cross-sections, and the Wong formula is used to calculate the ratio. It is observed that the tendencies of the experimental results start to diverge at deep sub Coulomb Barrier energies.

The discovery was confirmed in 2004 for another system of heavy nuclei [30]. Figure 1.17 shows the results as a logarithmic derivative $L(E) = \mathrm{d}\ln(\sigma E)/\mathrm{d}E$ in the upper part and the $S$-Factor on the bottom of the figure, *versus* the energy in the center of mass system for $^{58}$Ni + $^{58}$Ni (empty dots) and $^{64}$Ni + $^{64}$Ni (full dots) fusion reactions. Hindrance can be observed in both systems with a maximum of the $S$-Factor that is taken as an indication of the fusion hindrance. It is also pointed out that the position of the maximum is specific for the two reactions, 94 MeV for the $^{58}$Ni + $^{58}$Ni fusion reaction and 87.7 MeV for the $^{64}$Ni + $^{64}$Ni one. It shows the impact of the nuclear

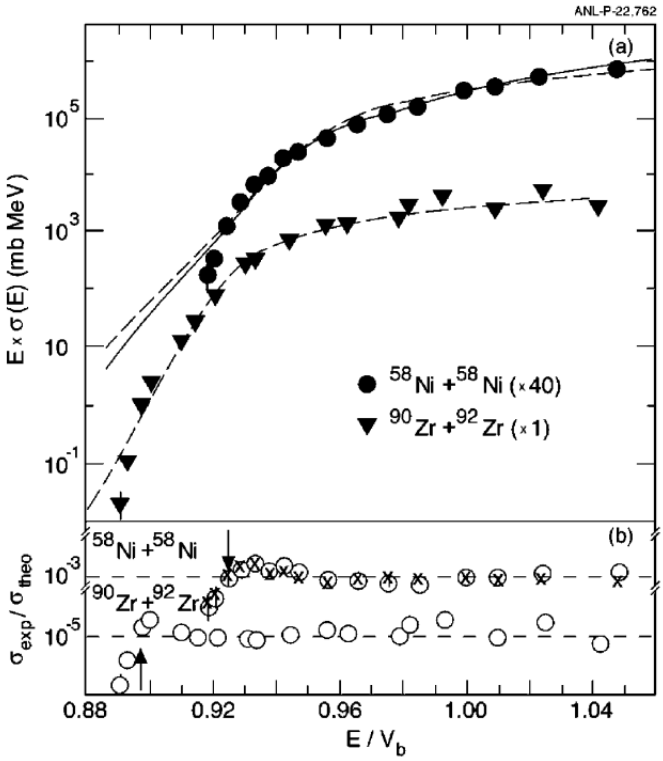


Figure 1.16: Cross-section (upper panel) plotted as $\sigma E$ *versus* the energy normalized to the Coulomb barrier $E/V_b$ with associated CC-calculations (solid line) and a phenomenological model using the Wong formula (dashed line) [29], used for the comparison between experimental and theoretical cross-section [1] (lower panel).

structure on the hindrance phenomenon and the stiffness of the nucleus is a hint to understand it. The $^{58}$Ni + $^{58}$Ni reaction involves stiffer nuclei than the $^{64}$Ni + $^{64}$Ni.

The position of the maximum can be approximated with the formula [31]:

$$E_s = 0.356\,(Z_1 Z_2 \sqrt{\mu})^{3/2}\,, \tag{1.23}$$

with $Z_1$ and $Z_2$ the charge numbers of the two involved nuclei and $\mu = A_1 A_2 / (A_1 + A_2)$ the reduced mass with $A_1$ and $A_2$ the atomic number of the nuclei. The hindrance phenomenon has meanwhile been observed in a vast sample of the fusion reactions, and theoretical approaches are developped to interpret it based on a rich survey of experimental data.

### 1.3.2 Theoretical approaches of the hindrance phenomenon

A first attempt to explain the hindrance phenomenon was introduced in 2006 [32], based on the M3Y (Michgan-3-Yukawa-Reid) portential with a repulsive core that

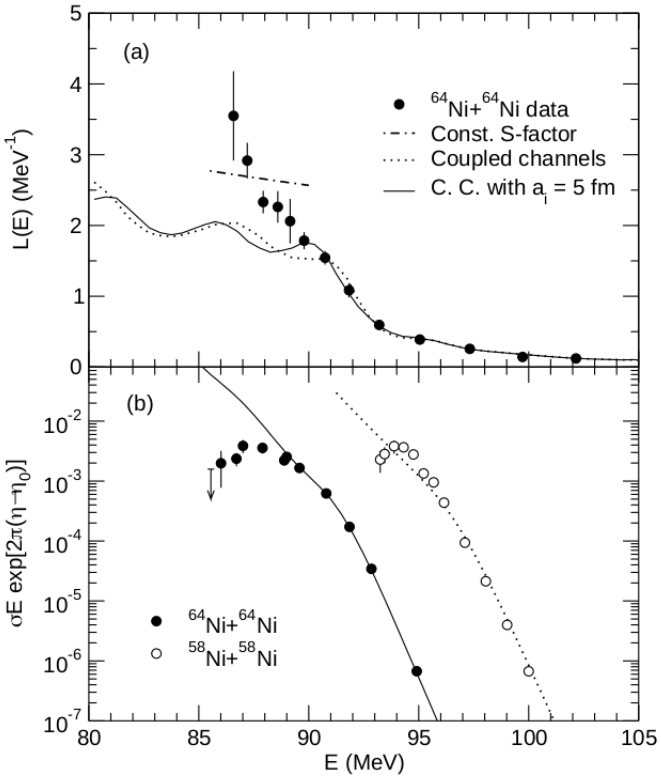


Figure 1.17: Logarithmic derivative $L(E) = \mathrm{d}\ln(\sigma E)/\mathrm{d}E$ on the top and the $S$-Factor on the bottom *versus* the energy for the $^{64}$Ni + $^{64}$Ni [30] and the $^{58}$Ni + $^{58}$Ni [1] reactions with associated CC-calculations.

reproduce the nuclear incompressibility. The associated potential is shown in Figure 1.18 in red *versus* the distance, with two other conventionnal potentials in dashed blue and black that do not take into account nuclear incompressibility for Akyuz-Winther and Proximitty '77 potentials, respectively. The dashed band represents the experimental boundaries. It appears that the M3Y + repulsion potential strongly diminishes the depth of the potential well from a local minimum at around $V_L \approx$ 70 MeV with the Akyuz-Winther potential to $V_L \approx 85$ MeV and fusion reactions are forbidden below these threshold energies.

The impact on the fusion reaction $S$-Factor is shown in Figure 1.19, investigating the measured hindrance of the $^{64}$Ni + $^{64}$Ni fusion reaction [30] and processing two CC-calculations, using the Akyuz-Winther potential (dashed blue curve) and introducing a rigid core of the nucleus with the M3Y + repulsion potential (red curve). The experimental data shows a maximum in the $S$-Factor in case of the latter potential, while the former does not. The repulsive hard core reproduces a maximum and the trend of the experimental data.

This repulsion term, however, only represents a phenomenological rendition of the

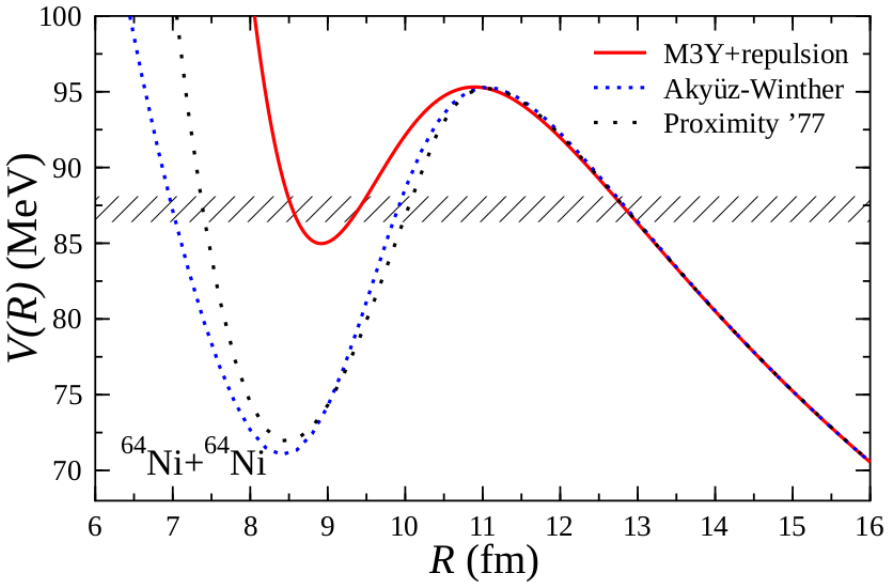


Figure 1.18: Nuclear potential as a function of the distance in the $^{64}$Ni + $^{64}$Ni, with the Akyuz-Winther and Proximity '77 potentials, that doesn't take the incompressibility into account in dashed blue and black, respectively, and M3Y potential including a repulsive term in red [32].

potential with little predictive power, so that approaches based on first principle calculations have been developped. The effect of Pauli repulsion has been investigated by Simenel *et al.* in 2017 [33] in more detail using Harthree-Fock (HF) calculations. This method gets by without introducing new parameters, deriving the bare potential from the energy density functional [34]. The Skyrme EDF force is used for the HF calculations and conventional potential. It already includes incompressibility but neglects the Pauli exclusion principle between nucleons with identical quantum numbers. The model that does not consider the Pauli exlusion principle is the Frozen Hartree-Fock (FHF) potential. The approach including the Pauli repulsion is called Density Constrained Frozen Hartree-Fock (DCFHF) [33].

The effects of Pauli repulsion on the nucleus-nucleus potential are shown in Figure 1.20 for $^{40}$Ca + $^{40}$Ca (a), $^{48}$Ca + $^{48}$Ca (b) and $^{16}$O + $^{208}$Pb (c) taking into account DCFHF Pauli repulsion (red dashed curve) and can be compared to FHF calculations (blue curve), with the respective cross-section measurements (d), (e) and (f), respectively, of the reactions. In all systems, Pauli repulsion generates a strong flattening of the depth of the potential well and a stronger repulsion at short distances as the barrier becomes wider. The effect will result in a decrease of the quantum tunneling probability and thus a reduction of the cross-section at sub-barrier energies, hence

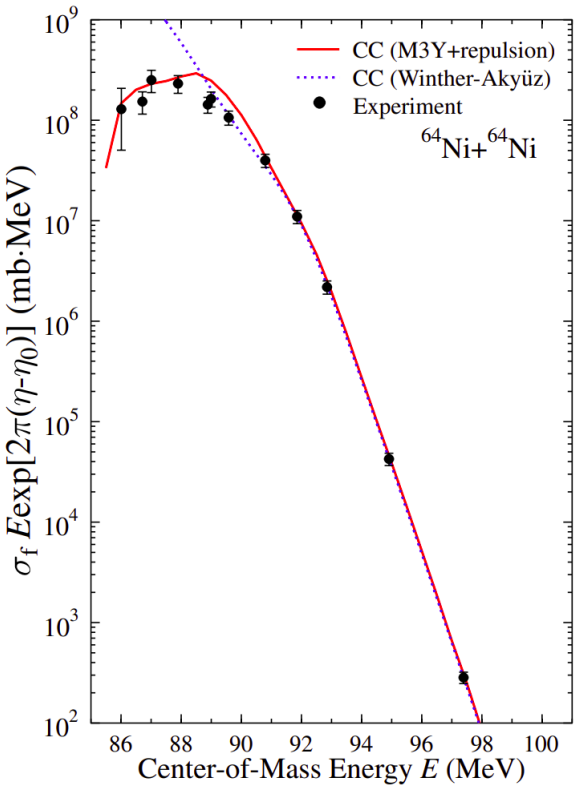


Figure 1.19: $S$-Factor *versus* the center of mass energy of the $^{64}$Ni + $^{64}$Ni fusion reaction, experimental data from Jiang *et al.* [30] and the theoretical interpretations using Akyuz-Winther and M3Y + repulsion in dashed blue and full red respectively [32].

hindrance.

The FHF calculations always overestimate the cross-sections for the three reactions, while the DCFHF calculations reproducing data more accurately for the $^{48}$Ca + $^{48}$Ca fusion reaction. For the two other reactions, the DCFHF model improves the estimation of the cross-section in the very low energy region, but it still overestimates it. Surprisingly, the $^{48}$Ca + $^{48}$Ca has the lowest barrier but the DCFHF calculations reproduce well the experimental data, while the $^{40}$Ca + $^{40}$Ca have the largest one and still overestimate the cross-section. It means that the Pauli repulsion does affect the fusion, but some additional nuclear interactions need to be considered.

A dynamical approach, the Density Constrained Time Dependent Hartree Fock (DCTDHF), is using the evolution of the internuclear distances within time steps, and performs a static energy minimization step by step [35]. Thus, the calculated ion-ion fusion barrier takes into account changes in the nuclear density. The effects of dynamical processes will not affect high energy fusion and provides similar results as the frozen calculations but affects the sub barrier energies [35].

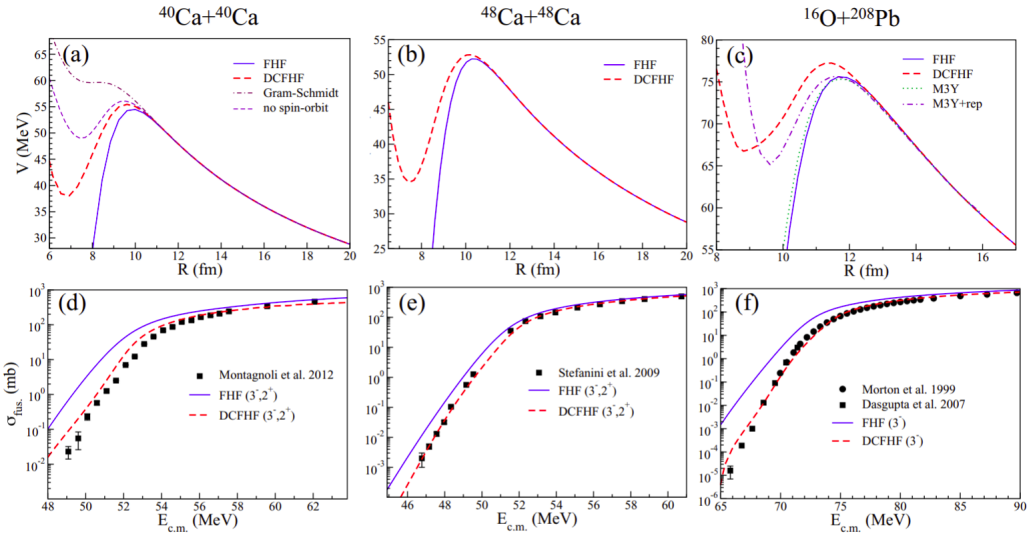


Figure 1.20: Nucleus-Nucleus potential in three reactions, $^{40}$Ca + $^{40}$Ca (a), $^{48}$Ca + $^{48}$Ca (b) and $^{16}$O + $^{208}$Pb (c) considering Pauli repulsion (DCFHF red dashed curve) comparing to the usual calculations (FHF blue curve), with their associated cross-sections (d), (e) and (f), respectively [33].

### 1.3.3 Hindrance in $^{12}$C + $^{12}$C

The hindrance phenomenon with a maximum in the $S$-Factor is intuitive to understand in the fusion reaction with negative $Q$-values, because the reaction is forbidden below this energy threshold so the cross-section vanishes. This is not the case for fusion reactions with positive $Q$-value, so the question about a maximum in the $S$-Factor is still open. Figure 1.21 displays the $^{12}$C + $^{12}$C, $^{12}$C + $^{13}$C and $^{13}$C + $^{13}$C reactions, CC-calculations for $^{12}$C + $^{13}$C and $^{13}$C + $^{13}$C fusion using a repulsive M3Y potential to reproduce data, indicating the presence of the hindrance phenomenon according to the autor [27].

The effect of hindrance is still debated for the $^{12}$C + $^{12}$C fusion reaction. Using CC-calculations, both the M3Y and the repulsive M3Y only reproduce the maximum of the resonances, but without a maximum in the $S$-Factor. The DCTDHF and DCFHF using Pauli repulsion do not predict to induce a maximum either. Figure 1.22 shows the $S$-Factor for the $^{12}$C + $^{12}$C fusion reaction, with different theoretical models, DC-TDHF using two different forces in dashed black and points and dashed purple, DCFHF in full black and FHF in dotted black. The dynamical effects in the DC-TDHF model reduce the effect of the Pauli repulsion compared to the DCFHF model, With the DCTDHF model. The top of the resonances are well described similarly to the CC-calculations. A phenomenological hindrance model is also shown in full red,

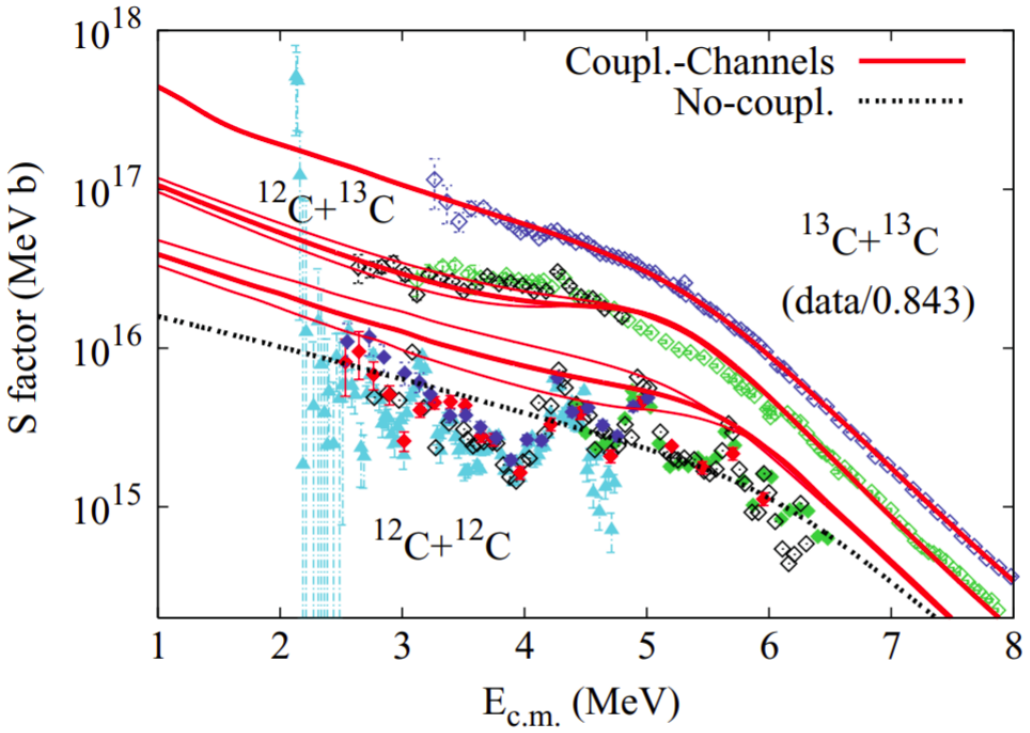


Figure 1.21: *S*-Factor *versus* the center of mass energy for three carbon related reactions: $^{12}C + ^{12}C$, $^{12}C + ^{13}C$, $^{13}C + ^{13}C$ with their associated CC-calculations. Figure taken from [27].

developed by Jiang *et al.* (2007) [36].

The hindrance model [36] was developed to describe sub-barrier fusion hindrance. It shows a maximum in the *S*-Factor. This model is based on a logarithmic derivate parametrised to fit data (see Section 1.3.1), with boundary condition that when the energy approaches zero, the cross-section must be finite and the logarithmic derivative diverges to infinity. Then the logarithmic derivative can be written as:

$$L\left(E\right) = A_0 + B_0/E^n, \tag{1.24}$$

with $A_0$ and $B_0$ fit parameters, $E$ the center of mass energy and $n = 3/2$. Thus, the cross-section can be written as:

$$\sigma\left(E\right) = \sigma_s \frac{E_s}{E} e^{A_0(E-E_s) - B_0 \frac{1}{E_s^{n-1}} \left[\left(\frac{E_s}{E}\right)^{n-1} - 1\right]}, \tag{1.25}$$

with $E_s$ the energy of the maximum in the *S*-Factor (see eq.1.23), and $\sigma_s$ is the value of the cross-section at $E_s$.

Recent results from the STELLA collaboration (Fruet *et al.* 2020 [37]) with measurements at deep sub-barrier energies are in good agreement with the hindrance model

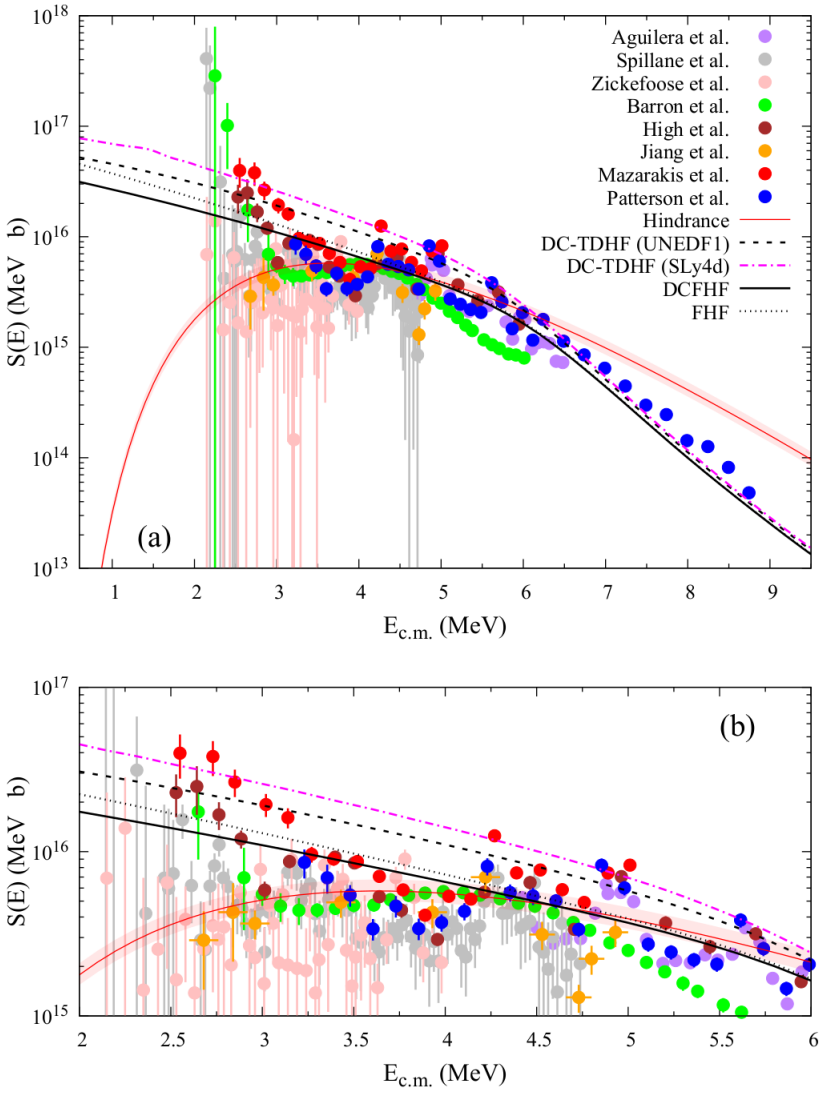


Figure 1.22: $S$-Factor *versus* the center of mass energy for the $^{12}$C + $^{12}$C fusion reaction with different theoretical models, DC-TDHF using two different forces in dashed black and points and dashed purple, DCFHF in full black and FHF in dot Black [35]. The hindrance model by Jiang *et al.* (2007) [36](a). The bottom pannel shows a zoom on the sub-barrier measurement (b).

in the energy range of $E_{\rm cm}$ = 2.1 to 5.5 MeV, however further experiments are still needed to characterize the excitation function at deep sub-barrier energies in more detail.

## 1.4 Résumé chapitre 1

Une étoile se forme par contraction gravitationnelle d'un nuage de gaz. En son sein, la pression et la température augmente jusqu'à permettre la fusion de l'hydrogène en son coeur, compensant l'attraction gravitationnelle pour atteindre un équilibre hydrostatique. Cette combustion se fait au travers de plusieurs réactions successives, appelées chaines-pp décrites dans le Tableau 1.1, mais également par réactions catalytiques avec des éléments plus lourds présents dans le coeur, décrites par les cycles CNO (Tableau 1.2). Dans tous les cas, l'hydrogène est transformé en hélium avec une chaleur de réaction $Q_{4^1\mathrm{H}\rightarrow{}^4\mathrm{He}} = 26.731$ MeV. Pour avoir lieu, ces réactions dans les étoiles doivent passer la barrière de Coulomb par effet tunnel quantique car l'énergie thermique des particules, décrite par une distribution de Maxwell-Boltzmann, est insuffisante pour la surmonter. Les réactions se font donc principalement dans une région en énergie appelé fenêtre de Gamow, définie par le pic de Gamow issu de la convolution entre la distribution en énergie des particules autour de la température $T$ et la probabilité d'effectuer un effet tunnel au travers de la barrière de Coulomb (Figure 1.3).

La fin d'une phase de combustion est marquée par une contraction du coeur de l'étoile jusqu'à atteindre les conditions d'allumage de la phase de combustion suivante et retrouver un équilibre hydrostatique. Après la combustion de l'hydrogène, vient la combustion de l'hélium par la réaction triple-$\alpha$ puis la phase de combustion du carbone avec la réaction de fusion $^{12}\mathrm{C} + {}^{12}\mathrm{C}$ et ses trois voies de sortie proton, alpha et neutron (équations 1.9, 1.10 et 1.11, respectivement), cette dernière étant défavorisée à basse énergie car sa chaleur de réaction est négative. C'est la première phase de combustion qui libère des particules légères dans le coeur, pouvant déclencher des réactions secondaires. La Figure 1.6 montre l'évolution des éléments pendant la phase de combustion du carbone utilisant des flèches pour indiquer le type de réaction et leur épaisseur pour indiquer leur intensité. Ceci indique l'importance d'une mesure précise de la section efficace de fusion de la réaction $^{12}\mathrm{C} + {}^{12}\mathrm{C}$, afin de bien déterminer l'enrichissement en éléments variés pendant cette phase de combustion.

On observe pour cette réaction une fonction d'excitation très spécifique présentant des oscillations plus prononcées sous la barrière de Coulomb, pouvant être comprises comme des résonances. Ces effets de structure nucléaire sont complexes à appréhender d'un point de vue théorique. La majorité des modèles décrivent uniquement le sommet des résonances. Certaines d'entre elles ont été associées à des états moléculaire dans le $^{24}\mathrm{Mg}$. L'idée des états moléculaires a joué un rôle crutial dans les années 1950 lorsque F.Hoyle [3] a prédit un état dans le $^{12}\mathrm{C}$ composé de trois noyaux d'hélium. Cet état a été identifié expérimentalement et cette vision a été dévelopée pour d'autres noyaux plus lourds, comme montré dans le diagramme de Ikeda Figure 1.11 [21]. Plus

récemment, des calculs théoriques se basant sur la théorie de la fonctionnelle densité d'énergie a mis en évidence des états clusters-$\alpha$ dans plusieurs noyaux $N = Z$, liant ceux-ci à des puits de potentiel locaux dans le potentiel total (Figure 1.13).

Une autre piste d'explication lie les oscillations dans la fonction d'excitation aux densités d'état dans le $^{24}$Mg, mettant en évidence une grande différence de densité d'état par rapport au $^{25}$Mg (Figure 1.15 [28]) en fonction de l'énergie d'excitation, le $^{25}$Mg ayant une densité d'état bien plus importante. Or, la fonction d'excitation pour la réaction de fusion $^{12}$C + $^{13}$C ne montre pas le comportement oscillant observé pour la réaction de fusion $^{12}$C + $^{12}$C (Figure 1.14). Dans ce cas, les oscillations seraient causées par une diminution de la section efficace de fusion dans les régions en énergie où il y a un faible chevauchement des états. Cet effet serait aacru par un nombre d'états disponibles réduit par les états initiaux $J^{\pi}(^{12}\mathrm{C}) = 0^{+}$ forçant la population d'états de spin pair avec une parité naturelle.

Enfin, en 2002 le phénomène de suppression de la fusion a été mis en évidence par Jiang *et al.* [1]. Il correspond à une diminution de la section efficace de fusion aux énergies profondément sous coulombiennes, par rapport aux prédiction des calculs en canaux couplés, référence jusqu'ici pour décrire la section efficace de fusion. Les mesures en question sont représentées sur la Figure 1.16 avec une représentation normalisée aux calculs théoriques au bas de la figure. Ce phénomène a ensuite été mesuré dans de nombreux systèmes impliquant des noyaux mi-lourds, mais est très débattu pour les systèmes plus légers. Dans le cas d'un phénomène de suppression de la fusion, un maximum dans le Facteur-$S$ doit apparaître et peut être décrit par l'équation 1.23. Différents modèles ont été proposés par les théoriciens, comme l'ajout d'un effet répulsif simulant un effet de coeur dur et d'incompressibilité dans le potentiel utilisé dans les calculs en canaux couplés [32]. Les résultats sont cohérents avec les mesures expérimentales dans de nombreux systèmes, cependant Simenel *et al.* [33] expliquent que le coeur dur et l'incompressibilité sont déjà compris dans le potentiel utilisé dans les calculs Time Dependent Harthree-Fock (TDHF) et Frozen Harthree-Fock (FHF) et que le terme répulsif ajouté englobent des effets comme le principe de répulsion de Pauli.

Ce dernier a été étudié dans des calculs Hartree-Fock qui ont la particularité de ne pas dépendre de paramètres (pas d'ajustement) et reposer sur la force utilisée. Les modèles en question sont Density Constrained Time Dependent Harthree-Fock (DCTDHF) et Density Constrained Frozen Harthree-Fock (DCFHF) prenant en compte les effets dynamiques dans le premier et non dans le second. Ils montrent que l'effet du principe de répulsion de Pauli épaississent la barrière de Coulomb et réduisent la profondeur du puit de potentiel (Figure 1.20), produisant une réduction de la section efficace de fusion. On voit sur la figure que pour deux systèmes symétriques, le

$^{40}$Ca + $^{40}$Ca et le $^{48}$Ca + $^{48}$Ca, la répulsion de Pauli reproduit correctement les données expérimentales pour ce dernier mais une légère différence subsiste dans le premier. Cela indiquerait que d'autres effets pourraient être impliqués dans le phénomène de suppression de la fusion.

Dans le cas de la réaction de fusion $^{12}$C + $^{12}$C, la suppression de fusion fait l'objet de discussions. Les calculs classiques ne décrivent que le sommet des résonances. Les calculs en canaux couplés utilisant un potentiel avec un ajout d'une répulsion pour simuler l'incompressibilité et les modèles Hartree-Fock prenant en compte la répulsion de Pauli en font de même. Aucun de ces modèles ne décrit de maximum dans le Facteur-$S$. Ainsi, on n'observerait pas de suppression de fusion dans ce système. Cependant, Jiang *et al.* [28] ont proposé un modèle phénoménologique décrivant le phénomène de supression de la fusion dans ce système qui inclut un maximum. Experimentalement, les résultats récents de Fruet *et al.* avec la collaboration STELLA montre un meilleur accord avec ce modèle phénoménologique, sur lequel on ajouterait des résonances. Il n'en reste que l'interprétation dans ce système est très discutée et nécessite davantage de mesures et de précision à basse énergie, où la mesure est extrèmement délicate. En effet, les sections efficaces sont extrèmement faibles, rendant toute mesure très sensible au bruit de fond.

# Chapter 2

# The STELLA experiment

As discussed in the previous chapter, the $^{12}$C + $^{12}$C fusion cross-section, through its resonant behaviour, can provide crucial information on the nuclear structure of $^{24}$Mg and fusion mechanisms below the Coulomb barrier, where the potential is not very well known. Its measurement is helpful to have a better understanding of the stellar evolution and the nucleosynthesis. However, measuring excitation function at deep sub-barrier energies is very challenging. This chapter will discuss the experimental technique used by the STELLA (STELlar LAboratory) collaboration to study the reaction starting with the advantages of the coincidence measurement of the evaporated charged particles and the gamma from de-exitation of the daughter nuclei. Then the developed experimental setup will be described.

## 2.1 Experimental technique

Several techniques exist to measure fusion cross-sections in a direct approach. Detecting separately charged particles or gamma decays, or measuring them in coincidence. The technique used usually depends on the system measured and the facility. As seen in the previous chapter, the $^{12}$C + $^{12}$C fusion reaction has three major exit channels:

$$^{12}\mathrm{C}(^{12}\mathrm{C}, p)^{23}\mathrm{Na} \quad (Q_p = 2.24\mathrm{MeV}), \tag{2.1}$$

$$^{12}\mathrm{C}(^{12}\mathrm{C}, \alpha)^{20}\mathrm{Ne} \quad (Q_\alpha = 4.62\mathrm{MeV}), \tag{2.2}$$

$$^{12}\mathrm{C}(^{12}\mathrm{C}, n)^{23}\mathrm{Mg} \quad (Q_n = -2.6\mathrm{MeV}), \tag{2.3}$$

where the neutron channel is closed at astrophysical energies. Thus, most of the experiments focus on the proton and the alpha channels at those energies.

### 2.1.1 Singles measurement

#### Charged particles measurement

Experiments focusing on charged particle detection only ([17], [18], [22] and [38]) use thin target foils from 10 to 50 $\mu$g/cm$^2$ to minimize the energy loss inside the target material and thus have a precise knowledge of the effective center of mass energy. They use silicon semi-conductor detectors that can be positioned at different angles, as the angular distribution of the differential cross-section can provide nuclear structure information. In forward angles (from 0° tot 90°), elastic scattering is very intense compared to the fusion signal at sub-barrier energies, so the detectors need to be protected with aluminum or nickel foils, the thickness depending on the angle and the beam energy. The thickness is kept minimal as the material degrades the effective energy resolution due to straggling. The advantages of measuring charged particles is that it is straight forward to access highly excited states providing the branching ratio of the excited states, as the measurement of the charged particle energy does not depend on the following de-excitation gamma cascade decay. In their work, Becker *et al.* measured excited states up to $p_{16}$ and $\alpha_{12}$, were $p_i$ or $\alpha_i$ describe the proton or alpha channel for the excited state $i$ of the daughter nuclei [17].

At deep sub-barrier energies, the measurement statistics drops exponentially with the energy and the measurement is subject to strong background coming from contaminant reactions. The latter come mostly from the water trapped inside the carbon target, $^{12}$C ($\geq$ 99.9%) enriched. The hydrogen isotopes, $^{1}$H and d, contained in water molecules can interact with the carbon beam nuclei, *via* elastic scattering, generating comparably low energy events in the particle detectors, but only in the forward direction due to kinematics. However, the rates can be very high, as the cross-section increases while the fusion cross-section vanishes, so that this contribution might hide low energy fusion events.

The most impacting contamination at deep sub-barrier energies ($E_{\mathrm{cm}} \leq 3.5$ MeV) comes the reaction $d(^{12}\mathrm{C}, p)^{13}C$, that produces protons in the energy range of the ground state and first excited state of the alpha and proton channel in the $^{12}$C + $^{12}$C fusion reaction. As at these energies, the $^{12}$C + $^{12}$C fusion cross-section is lower than the $\mu$b, the measurement relying on charged particle detection only is thus subject to uncertainties.

Finally, the target thickness may increase with time when exposed to the beam by deposition of the residual gas inside the chamber. If dedicated silicon detectors are used to measure elastic scattering, the normalization can be corrected, but it can impact the interaction energy and increase uncertainties.

### Gamma measurement

The gamma measurement technique ([9], [24]) consists of measuring the fusion cross-section *via* the de-excitation of the daughter nucleus. The approach is mostly focussed on the detection of the first excited state at $E_\gamma = 440$ keV for $^{23}$Na and $E_\gamma = 1634$ keV for $^{20}$Ne, because the de-excitation through these states amounts around 63% and 100% for the $^{23}$Na and $^{20}$Ne, respectively. Such gamma experiments use both thin or thick targets. In the case of thick target the beam is stopped inside the target allowing the use of very intense beams without degrading the target. The reaction energy varies from the beam energy to zero. To retrieve the fusion cross-section at a definite energy $E$, a sequence of measurements with changes of the beam energy step by step is generally performed. The counting rate is evaluated step by step and the cross-section can be computed using the following formula:

$$\sigma\left(E\right) = \frac{M_{\mathrm{T}}\mathrm{d}Y}{fN_A\mathrm{d}E}\frac{\mathrm{d}E}{\mathrm{d}(\rho x)}, \tag{2.4}$$

where $M_{\mathrm{T}}$ the molecular mass of the target, $Y$ the measured counting rate, $f$ the molecular fraction of the nucleus of interest in the target, $N_A$ the Avogadro number and $\frac{\mathrm{d}E}{\mathrm{d}(\rho x)}$ the stopping power of the beam inside the target.

Those methods measuring gamma only have to compromise between efficiency and energy resolution. In case of deep sub-barrier energies, when the cross-sections cease below the $\mu$b level,it may be difficult to separate signal from background. In the publication of Spillane *et al.* [9], it can be observed that the alpha channel can provide reasonable uncertainties, because the first excited state of the $^{20}$Ne is at quite high energy (1634 keV), hence less subject to Compton background than the first excited state of the $^{23}$Na. However, the presented error bars on the proton $S$-factor show the difficulties to measure precisely at energies as low as 440 keV. A gamma contamination from $p(^{12}\mathrm{C},\gamma)^{13}N$ and $d(^{12}\mathrm{C},p\gamma)^{13}C$ with $E_\gamma = 2360$ keV and $E_\gamma = 3090$ keV can also increase the Compton background, making the measurement of the first excited state of the $^{23}$Na very difficult. This also impacts the measurement of the first excited state of $^{20}$Ne at very low energies ($E_{\mathrm{cm}} > 2.5$ MeV).

## 2.1.2 Coincidences technique

The measurement of the $^{12}$C + $^{12}$C fusion cross-section at deep sub-barrier energies is very challenging and both gamma or charged particles technique are hampered by characteristic background contamination. To overcome it, a coincidence technique can be used measuring gamma and charged particles at the same time. The coincidence technique commonly used in nuclear physics has been introduced recently in nuclear astrophysics experiments at the Argonne National Laboratory by Jiang *et al.* [39] in

2018. It was shown that it allows for a better identification of the events at higher accuracy.

This technique benefits from selection of events using charged particles and gamma energy, optionally coupled to a time selection, as false coincidences may be recorded at a random timing while correlated signals happen in a well defined time interval. Looking at the shortcomings of single measurements, on the gamma side, the pollution of the energy spectrum from Compton events will be strongly reduced with the particle energy selection and the timing restrictions. On the charged particles side, the main contamination from $d(^{12}\mathrm{C}, p)^{13}C$ produces protons at the same energies as the signal from $^{12}\mathrm{C}$ + $^{12}\mathrm{C}$ fusion events, but the $^{13}\mathrm{C}$ is in its fundamental state, so there is no gamma emission. In other words, the contamination is usually completely suppressed by the gamma energy selection, or can be subtracted by directly measuring the random coincidence background.

## 2.2 The STELLA experiment

The STELLA (STELlar LAboratory) collaboration chose to build a coincidence experiment dedicated to astrophysically relevant reactions. It has been financed by the University of Strasbourg Institute of Advanced Studies (USIAS), the Initiative d'Excellence programme (IdEx) and CNRS-IN2P3. It is composed by a fusion reaction chamber, a vacuum system, specific target holders and a acquisition system to synchronize particles and gamma detectors from the collaboration UK-FATIMA (FAst TIMing Array). The STELLA experiment is developed to study light-medium heavy ion fusion reaction. Most of the developments have been made at Institut Pluridisciplinaire Hubert Curien (IPHC) in Strasbourg and the experiment is performed at the Andromède facility at IJCLab Orsay. The development of the STELLA apparatus and the commissioning experiment was performed during Guillaume Fruet's PhD [40, 8].

### 2.2.1 Reaction chamber

The reaction chamber of the STELLA experiment is a compact ensemble constituted of a stainless steel cylinder, closed on the top by a 2.5 mm thick aluminum dome to minimize the absorption of the gamma rays passing through it. As depicted in Figure 2.1, it encloses three silicon detectors that will be described later in this Chapter. In the middle of the chamber, the target holder can hold different types of targets and that can be changed from outside (Target Switch on top left of Figure 2.1). An intense beam represented by the yellow arrow crosses the detector holes and hits the target that rotates thanks to a motor magnetically coupled to the outside of the chamber.

The beam is monitored using a Faraday cup integrator and two surface barrier silicon detectors placed at 45° with respect to the beamline, measuring the elastic scattering. On the bottom of the chamber, a valve isolates the chamber from the cryogenic vacuum pump. Details on the different parts of the setup will be given below, starting with the silicon detectors.

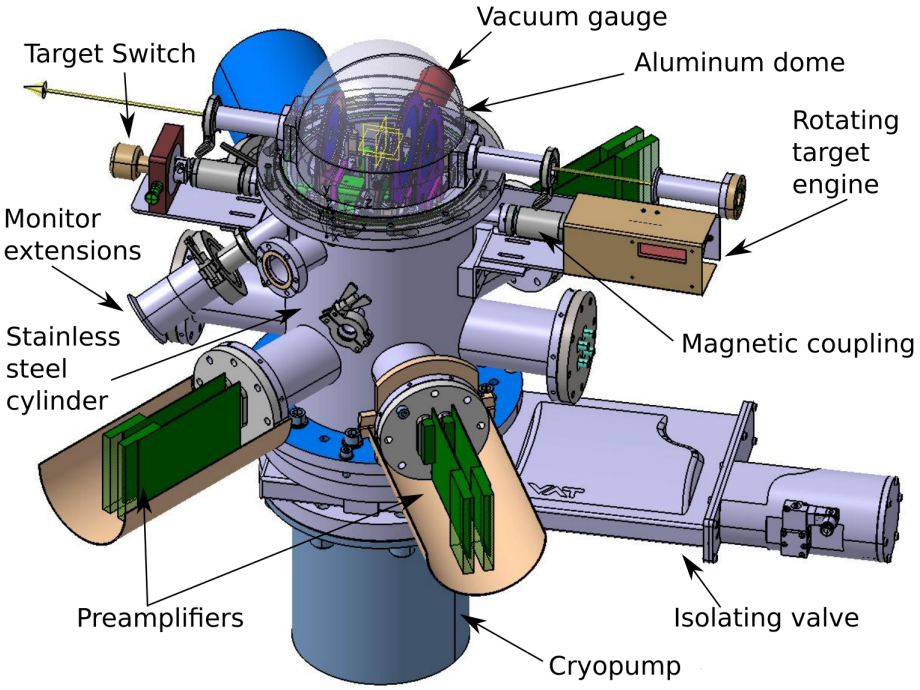


Figure 2.1: 3D CAD representation of the reaction chamber [40].

The particle detectors used to measure the fusion events are four silicon detectors with chips provided by Micron Semiconductor Ltd and mounted on PCB at IPHC Strasbourg. Two of them are Double Sided Striped Silicon Detectors (DSSSD) S3 types, one DSSSD S1, and the last one, PIXEL, can switch between Position Sensitive Detectors (PSD) BB10 or a SUPER-X3 type, depending on the experimental needs. The S3 detectors are positioned at forward (S3F) and backward (S3B) directions with respect to the beam, their position is indicated by the red arrows in Figure 2.2. The S1 detector is positioned between the target and the S3B detector and PIXEL has been added between the target and the S3F detector and can be seen on the photography in Figure 2.3. The detectors covers the angles from 10.4°to 30.3°, 122.4°to 141.8°, 148°to 159°and 45°to 90°, for S3F, S1, S3B and PIXEL, respectively.

### DSSSD S1

The S1 and S3 detectors have a cylindrical symmetry, S1 has 64 incomplete rings on the junction side with a 1505 $\mu$m strip pitch considering a 96 $\mu$m resistive separation,

and 16 sectors on the ohmic side. To save exit channels and the load on the readout electronics, the rings have been merged into 16 full circles. As the detector is situated on the backward side, for the $^{12}C + ^{12}C$ fusion reaction at the beam energy considered here, a detector thickness of 500 $\mu$m is enough to stop all particles.

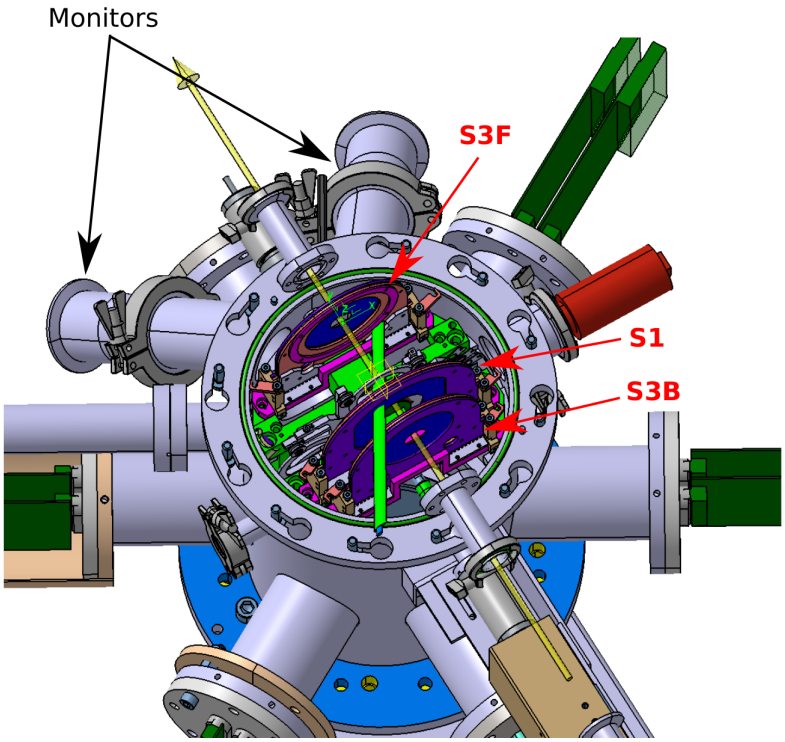


Figure 2.2: 3D CAD representation of the reaction chamber seen from the top [40].

The electronic mapping of the S1 detector is displayed on Figure 2.4. The ground connectors are represented with green circles and purple tracking lines. All sectors are connected to the ground as described on the left side of the scheme. The right side of the map shows that the rings are connected in 16 full circles that are distributed to 16 pins, eight on each side of the beam line. The rings are polarized under -60 V through two 12-channels differential preamplifiers from Mesytec®, with a typical leakage current below 200nA for the tested DSSSD. [40]

The output signal has a rising time between 80 and 120 ns and a falling time between 15 and 20 $\mu$s, taken with a triple-alpha source of $^{239}$Pu, $^{241}$Am and $^{244}$Cm, radioactive elements decaying by alpha emission with a main decay of $E_\alpha = 5.15$, 5.48 and 5.80 MeV, respectively. The measured resolution of the detector tested at these energies gives a Full Width at Half Maximum (FWHM) FWHM = 0.7%.

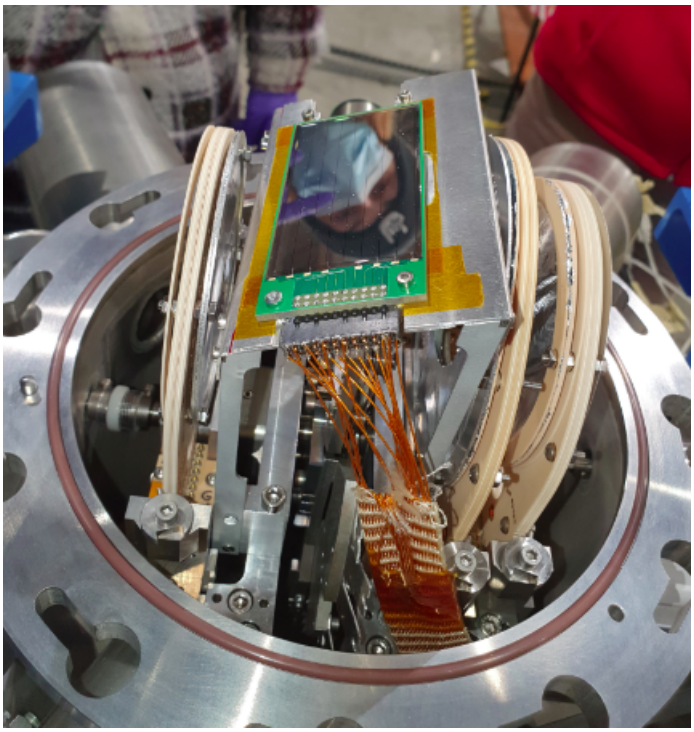

Figure 2.3: Photography with inside view of the STELLA reaction chamber taken during the 2022 experimental campaign.

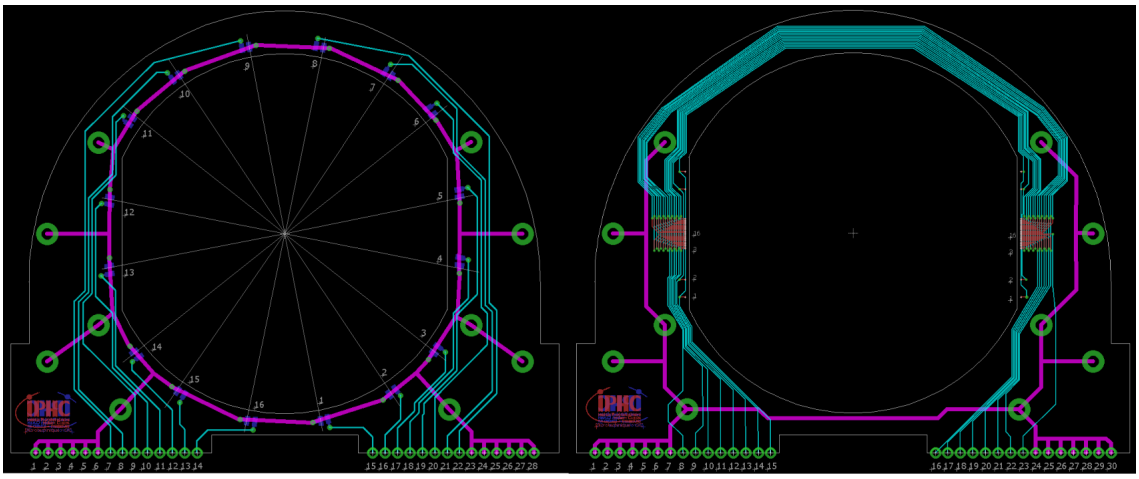

Figure 2.4: Scheme of the S1 Printed-Circuit Board (PCB) designed and mounted at IPHC Strasbourg, sector side on the left and ring side on the right [40].

### DSSSD S3

The S3 DSSSD has 24 complete rings on the junction side (see photo Figure 2.6) and 32 sectors on the ohmic side. The width of the rings is 986 $\mu$m with a 100 $\mu$m resistive separation. The active area spans from a diameter of 22 mm to 70 mm. Figure 2.5

shows the electronic mapping of the S3 detector. Similar to the S1, the sectors are fully connected to the ground. Each of the 24 ring has a separate signal distributed on each side of the detector with respect to the beam line. Two detector thicknesses were used, 500 $\mu$m and 1000 $\mu$m, the latter for high energy protons at beam energies around $E_{\rm cm} \approx 5$ MeV. Only the 500 $\mu$m thick S3 type detectors have been used in the 2019 campaign discussed in this manuscript as the beam energy investigated was low enough so that all particles from fusion are fully stopped inside the detector substrate.

The S3 detectors have been tested with a triple-alpha source under a polarization voltage of -60 V. Typical pulses have a rise time between 80 and 120 ns and a fall time between 15 and 20 $\mu$s. The resolution measured with the triple-alpha source at corresponding alpha energy is FWHM = 0.5%.

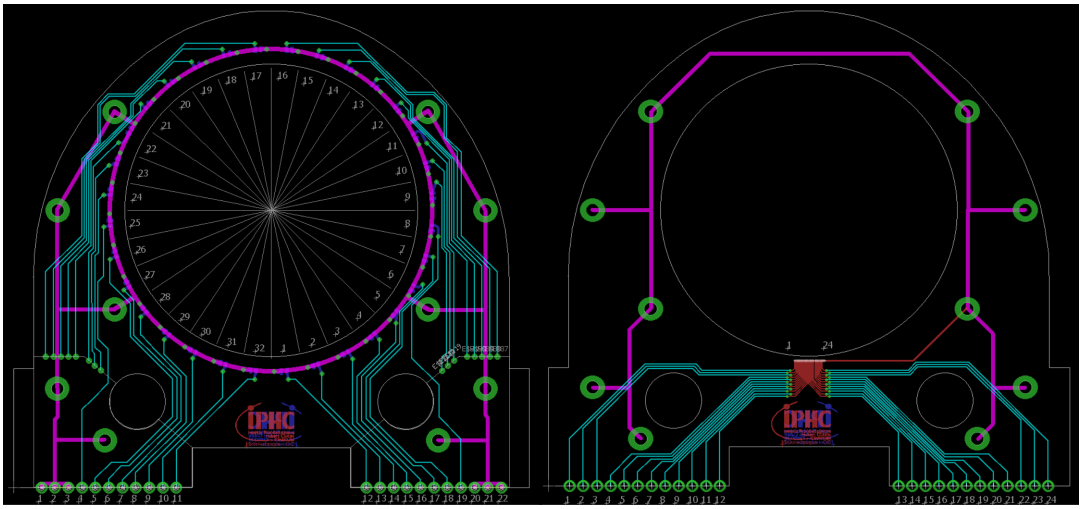

Figure 2.5: Scheme of the S3 Printed-Circuit Board (PCB) designed and mounted at IPHC Strasbourg, sector side on the left and ring side on the right [40].

The PCB is made of RO4003C$^{\rm TM}$, a material of ROGERS Corporation, a specific ceramic substrat reinforced with glass braids, known to be a very low outgasing material and essential for the vacuum level required in sub-$\mu$b cross-section measurement ($P \approx 10^{-8}$ mbar). The design of both S1 and S3 PCB have been developed at IPHC, as the standard model from Micron (Semiconductor Ltd) does not fit inside the reaction chamber and to minimize absorption. To this end, the connection to the preamplifiers are guided toward the bottom of the detector to a connector in contact on spring pins toward Kapton® cables used also for their good vacuum properties. The preamplifiers are differential MPR-16D from Mesytec® and are directly connected to the feed through of the chamber to reduce the electronic noise. The cards are hosted in an aluminum cylinder used as Faraday cage to avoid parasite electromag-

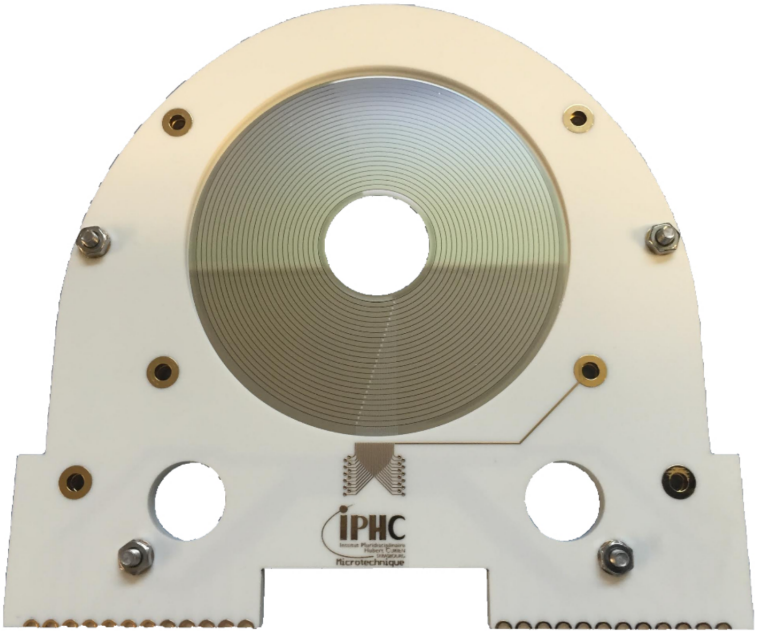


Figure 2.6: Photography of the S3 detector on the junction side, the ring are visible with the mass connectors (small circles on the PCB-board) and the connections to the pins on the bottom. Credits : G. Fruet.

netic signals disturbing the measurement. Then shielded cables carry the signal from the preamplifiers to differential to single headed converters.

The S3F detector is positioned at 60 mm from the target, covering the laboratory angles between $\theta_{\text{lab}}$ =10.4° and 30.3°, the S3B is at 56 mm from the target covering the angles $\theta_{\text{lab}}$ =148° to 169°. The S1 detector is closer to the target, namely at 31 mm covering the angles $\theta_{\text{lab}}$ =122.4° to 141.8. The associated solid angles are 0.75, 0.84 and 1.57 sr for S3F, S3B and S1, respectively. Both the S3B and the S1 detector are protected with 0.8 $\mu$m thick aluminum foil to stop electrons emitted when beam hits the target. The thickness is optimised to minimize degradation of the effective energy resolution from straggling inside the foil. For the S3F detector, the foil has to stop electrons but also the $^{12}$C from elastic scattering. As in the forward direction the particles are more energetic, a 10 $\mu$m thick aluminum is used.

The foils are fixed on RO4003C$^{\text{TM}}$ hoops and screwed through the circles connected to the ground (see Figure 2.6) to evacuate the charge accumulated on the foil and avoid discharge on the detector, as the aluminum foils are fixed on the ohmic side that faces the target. The systematic uncertainty of the solid angle of the detectors is $\Delta\Omega = 3\%$.

### PIXEL

PIXEL is an additional set of detectors added in 2022 that aims to complete the angular coverage at steep angles (from 45°to 90°) to measure angular distribution and increase the solid angle of the experiment. Two types of detectors can be used, a BB10 for the angular distributions and a SUPER-X3 for the low energy measurement, both detectors being manufactured by Micron Semiconductor LTD.

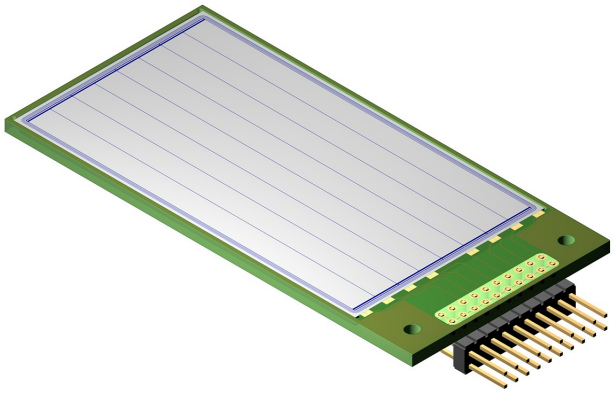

Figure 2.7: 3D view of the BB10 Detector [41].

The BB10 detector is a DC strip silicon detector without bias resistors composed of eight junctions strip with junction pitch of 4944 $\mu$m and a total active area of 39.45 $\times$ 74.15 mm$^2$ and a thickness of $\approx$ 1 mm. Figure 2.7 shows a 3D view of the BB10 detector. The eight junctions can be identified as well the connections of the strip to the pins (small rectangles at top side of each strip). This detector is used for its segmentation, as the signal is only collected at the beginning of the strip and the position of the event on the strip can be determined with a pulse shape analysis. However, the timing of the event is not adapted for efficient gamma-particle coincidences at low energy measurements, meaning that the speed of the response is not fast enough to perform a precise timing selection. But its angular precision provide helpfull informations to measure angular distributions.

Another type of detector is thus used, the SUPER-X3 (seen in Figure 2.8) which is a PSD detector of four junction strips and four ohmic sectors. The total active area is 40.30 $\times$ 75.00 mm$^2$ with a thickness of 1 mm. The signal on the junction side is collected from both side of the strips so that the position of an event can be determined. The timing is thus much better than with the BB10 detector.

Both detectors have been used during the experimental campaign in 2022 protected with a 6 $\mu$m thick aluminum foil and covering the angles between 60° and 90°, at steep

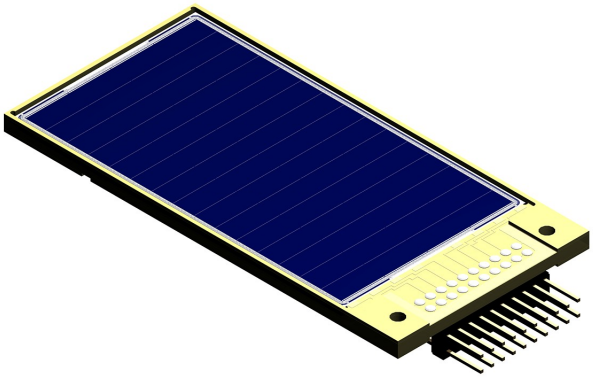

Figure 2.8: 3D view of the Super-X3 Detector [42].

angles with respect to the target.

### Monitors

The so called monitors are placed at 23 cm from the target at an angle of 45°angle with an aluminum collimator of 1 mm diameter. Surface barrier silicon detectors are usually used and they aim to measure the $^{12}$C + $^{12}$C elastic scattering used for the normalization. The elastic scattering cross-section beeing quite large compared to the fusion cross-section at sub-barrier energies, the detector can be damaged quite fast developing blind spot after exposure. Its position can be adjusted (rotation) independently from the collimator to change the irradiated area without changing the angle, effectively increasing the liftime of the detector.

The precision of the angle is important because the $^{12}$C + $^{12}$C elastic scattering cross-section has a strong angular dependency. The scattering of two identical bosons is described by the Mott cross-section. The differential cross-section in the center of mass system can be exactly described considering only the electromagnetic interaction [43]:

$$\left(\frac{\mathrm{d}\sigma}{\mathrm{d}\Omega}\right)_{\mathrm{cm}} = \frac{Z^4 e^4}{44\pi\epsilon_0 E_{\mathrm{cm}}} \times \left[\frac{1}{\sin^4\left(\frac{\theta_{\mathrm{cm}}}{2}\right)} + \frac{1}{\cos^4\left(\frac{\theta_{\mathrm{cm}}}{2}\right)} + \frac{2}{\sin^2\left(\frac{\theta_{\mathrm{cm}}}{2}\right)\cos^2\left(\frac{\theta_{\mathrm{cm}}}{2}\right)} \cos\left(\frac{Z^2 e^2}{4\pi\epsilon_0\hbar\nu} \ln\left(\tan^2\left(\frac{\theta_{\mathrm{cm}}}{2}\right)\right)\right)\right], \tag{2.5}$$

where $Z$ is the atomic number of the nucleus, $e$ the elementary charge, $\epsilon_0$ the dielectric constant, $\hbar$ the reduced Planck constant, $E_{\mathrm{cm}}$ and $\theta_{\mathrm{cm}}$ the energy and the

angle in the center of mass system.

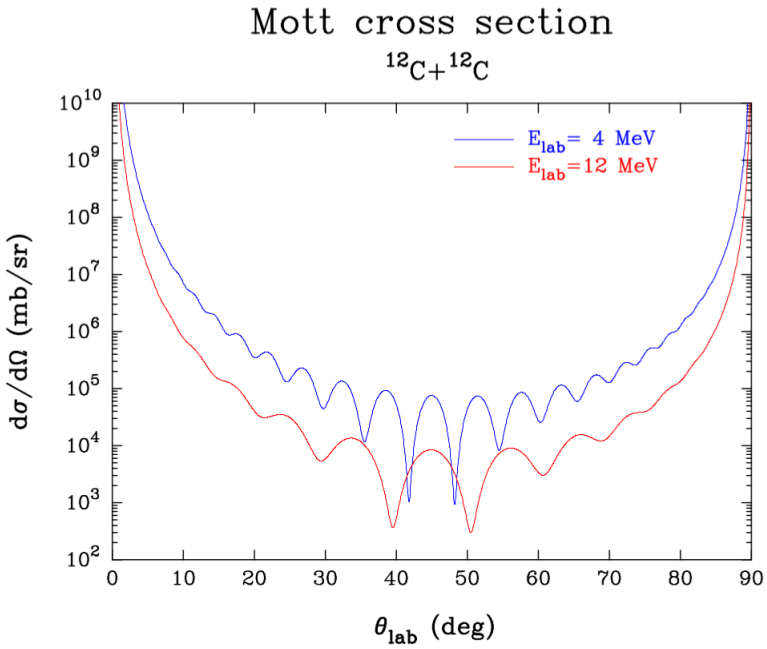


Figure 2.9: Differential cross-section in the laboratory frame for the $^{12}$C + $^{12}$C Mott scattering at two energies: $E_{\text{lab}} = 4$ MeV and $E_{\text{lab}} = 12$ MeV [40].

Figure 2.9 shows the differential cross-section of $^{12}$C + $^{12}$C Mott scattering at two energies: $E_{\text{lab}} = 4$ MeV and $E_{\text{lab}} = 12$ MeV in the laboratory frame. The $^{12}$C + $^{12}$C Mott scattering is not defined at angles $> 90°$ (backward direction), because of the identical masses of the particles. The interferences pattern appears due to the quantum properties of identical bosons (oscillations in the differential cross-section). Comparing the two energies investigated shows that only the angle $\theta_{\text{lab}} = 45°$ stays on a local maximum, while the others local maxima change with energy. It demonstrates the importance of the fixed and precise 45° angle for the measurement in the monitors for a consistent measurement for normalization of the data.

Nevertheless, high counting rates make the monitor spectra difficult to analyze for accurate data normalization. Nevertheless, the monitor is still used to verify the integrity of the target and the position of the beam combined with information from the Faraday cup used for the normalization instead.

### 2.2.2 Vacuum system

To perform the experiment in the best conditions an minimize the interactions between the beam and residual gas in the chamber, a pressure of $P \leq 10^{-7}$ mbar in the reaction

chamber is required. The STELLA project uses a combination of two pumps, a primary dry pump and a cryogenic pump. The primary dry pump is directly connected to the chamber *via* a stainless-steel tube close to the vacuum gauge (see Figure 2.1) and the pumping can be adjusted by a very precise valve, so that the air flux does not damage the foils (target and aluminum protections) inside the chamber.

The primary pumping reaches a vacuum of around $6.0 \times 10^{-2}$ mbar within few minutes and the cryogenic pumping can be started. The cryogenic vacuum pump has a diameter of 20 cm and is fixed at the bottom of the chamber separated by a valve (see Figure 2.1). The opening of the valve can be made at $6.0 \times 10^{-2}$mbar, but in order to get a very good pumping during a long time, a turbomolecular pump on the beamline close to the chamber can be used to reach $P = 10^{-3}$ to $10^{-4}$ mbar.

The cryogenic pump is a very cold trap ($\approx$ 15 K), composed of plates cooled using He gas. The residual gas inside the chamber hits the plate and transfers its kinetic energy. The molecule is then frozen on the plate, completely trapped and the plate transfers the energy to the Helium gas that is cycled with a compressor to maintain the temperature level. Cryogenic pumping is very effective for most gases. The vacuum reached for the STELLA experiment is $P = 10^{-8}$ mbar.

To ensure reaching this vacuum, low outgasing materials are used (PCB cables *etc*...), with cautions manipulations when the chamber is open and the surface inside chamber can be passified upon opening using nitrogen flushing with a precise valve to avoid damaging the foils.

### 2.2.3 Targets and thickness measurement

Thin carbon targets, between 20 and 80 $\mu$g/cm$^2$ are used in the STELLA experiment to minimize the energy loss in the target and favour accurate determination of the interacting energy. Such thin targets are very sensitive to heat generated by the energy loss of the beam inside the target. As intense beam are required for the present experiment and taking for example a 50 $\mu$g/cm$^2$ thick $^{12}$C target with a 5 MeV beam, the energy loss inside the target is around 350 keV. With a beam of 5 p$\mu$A, a power of 1.75 W is generated inside the target. In collaboration with the Grand Accelerateur National d'Ions Lourds (GANIL), a system of rotating targets has been developed at IPHC. It aims to disperse the generated heat avoiding degradation of the target. Thermal studies have been made by M. Krauth (IPHC) during the development of STELLA [8].

Figure 2.10 shows the target support that can hold three rotating targets and six fixed targets on the yellow plate on the Figure. The position in the middle of the plate is reserved for a target frame electrically isolated from the chamber to control

the beam focussing from a current measurement.

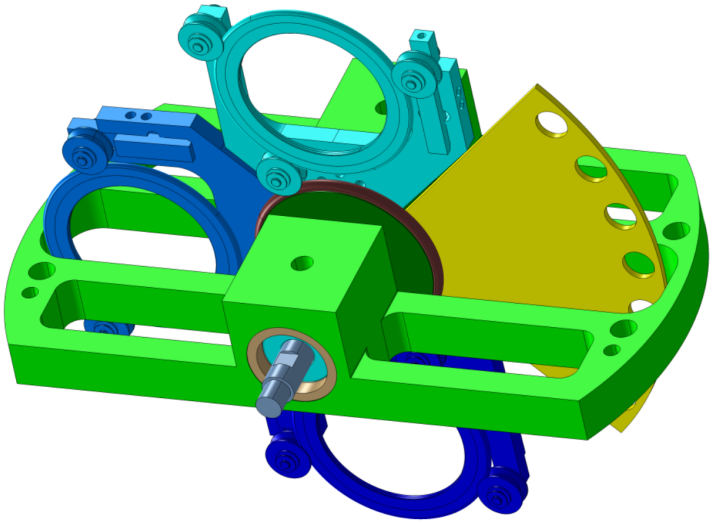

Figure 2.10: CAD representation of the target holder designed for the STELLA experiment [40].

The rings in blue are the rotating target frames spinned with carbon foils and inner and outer diameters of 46 and 63 mm, respectively. The foils are made at the laboratory GANIL with natural carbon (98.9% of $^{12}$C). The beam hits the target around 8 mm of the inner border of the frame. The frames are held by three small wheels, that can move freely to allow the rotation of the target. The motion of the target is transmitted by contact with the central wheel in brown in the middle of Figure 2.10, that rotates *via* a motor magnetically coupled to the reaction chamber up to 1000 rpm. This magnetic coupling has been developed by UHV Design LTD [44] and is designed to high vacuum requirements.

### Target Thickness Measurement

As the aim of this work is to perform accurate measurements possible, knowing the thickness of the target is crucial, as the normalization of the cross-section and the interacting energy of the measurement depend on it. Thin targets, when irradiated by beam and in the environment in the chamber, can suffer a change of thicknesses. Studies of carbon target growth and contamination have been performed in the past [45, 46]. In particular, they show that the main contribution of the phenomenon is dependent on the vacuum quality and the temperature of the target. Indeed, while the target is irradiated by a beam, carbon molecules are ionized and recombined with molecule from the residual gas inside the chamber. The broken link between carbon molecules allows the bounding with residual gas molecules. Figure 2.11 from Healy

*et al.* [46], shows the deposition on a carbon target with respect to the temperature of the target. It shows a decreasing curve when temperature increases with a saturation around 175°C, explained by the decreasing secondary electrons emitted with the increase of the temperature, that also limits the condensation of the residual gas.

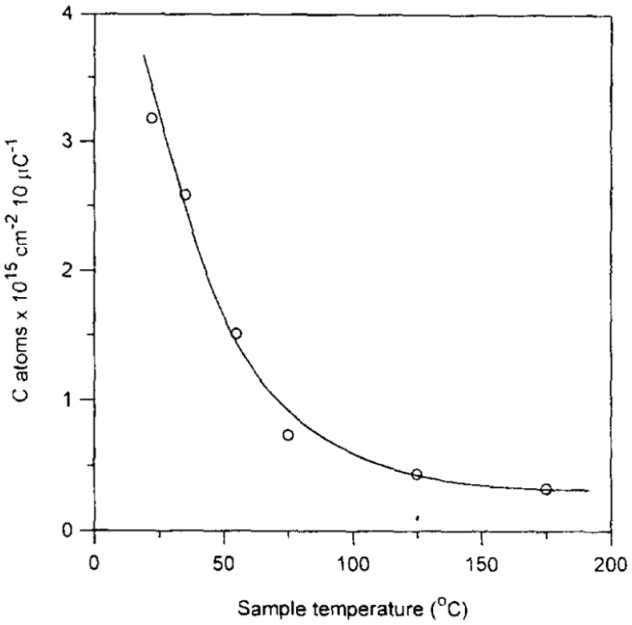


Figure 2.11: Gas deposition on a carbon target with respect to the temperature [46].

A study from Blondiaux *et al.* [45] demonstrates that the thickness increases essentially at the beam spot and not all over the surface of the entire target. Thus, its increase can be easily measured using a target thickness measurement experiment.

A dedicated reaction chamber has been developed in collaboration with the University of York and was strongly improved durnig this PhD. It can be seen in Figure 2.12 with the reaction chamber and its dedicated acquisition system. The experimental setup in the chamber (Figure 2.13) contains an alpha source (a triple-alpha and a $^{241}$Am intense source), with a collimator allowing an angular opening of 2.4°, a moving target holder with two engines moving in 2D with a micrometer precision, and a silicon detector. The goal is to measure the energy loss of the alphas inside the target and deduce the thickness of the target. The Faraday cage of the experiment has been upgraded to reduce the background noise, and a customized preamplifier from CREMAT Inc. is used to amplify the signal and deliver a single ended signal to a FMC112 card. The resolution reached is FWHM $=$ 19 keV.

Figure 2.14 shows the impact of the fluctuation of the room temperature during day and night on the energy measurement, expressed as a variation of the measured energy of the main decay of $^{241}$Am with respect to time (black curve). Here the run

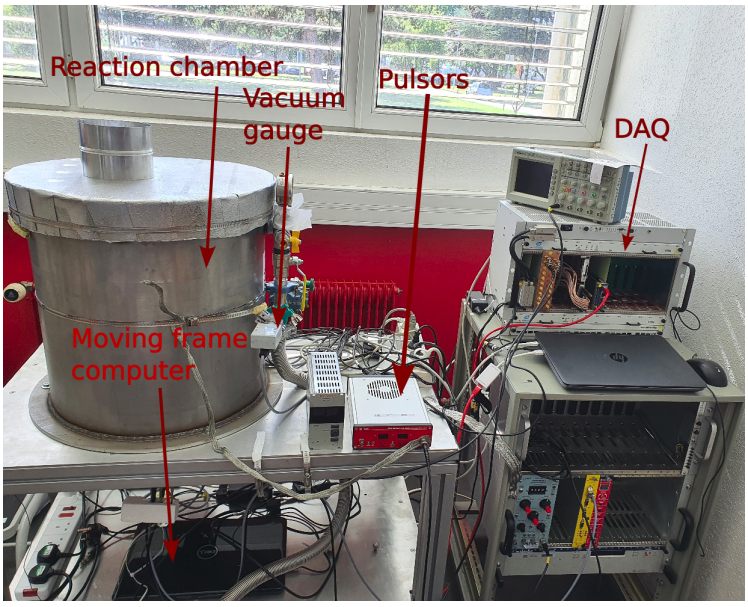


Figure 2.12: Photo of the target measurement station with the chamber and the acquisition system.

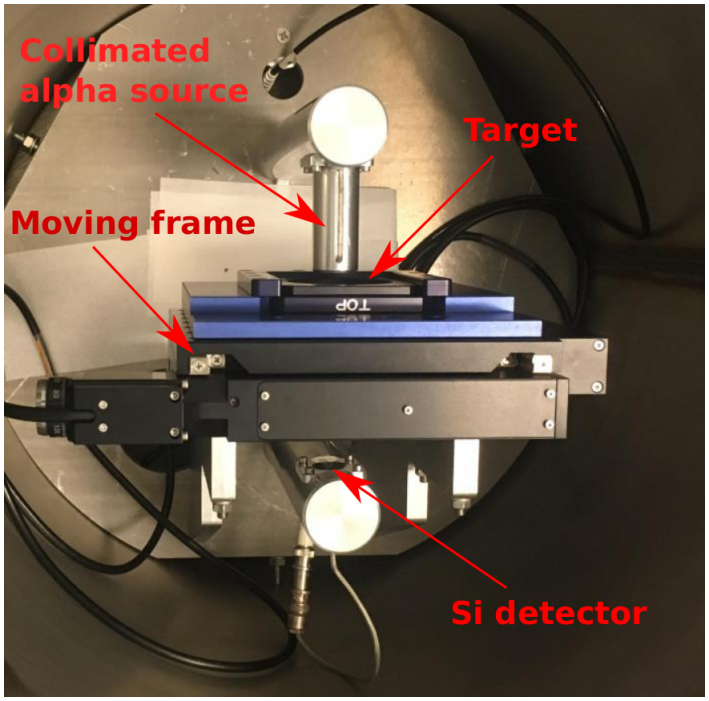


Figure 2.13: View of the inside of the reaction chamber with the collimator, the moving target holder and the silicon detector [40].

is divided into 30 periodes of approximatly 2 h. A difference of 40 keV is observed between a local minimum and a local maximum. For comparison, the energy loss of a 5.5 MeV alpha particle inside a 50 $\mu$g/cm$^2$ carbon target is $\Delta E = 36.6$ keV.

A method has been developed to follow the variations of the gain of the preamplifier. Four pulsers are inserting signals of a constant amplitude into the preamplifier, two below and above the triple-alpha source energies and two below and above the $^{241}$Am contribution. They can be used to correct the calibration with time and get rid of the impact of the temperature evolution. The application of this method is shown in red in Figure 2.14, where the amplitude diminishes from 40 keV to 4 keV, constituating a very strong improvement. Furthermore, an air conditioning system has been installed in the experimental room to stabilize the temperature of the room reducing the variation to 1-2 keV and allowing precise measurement of energy losses.

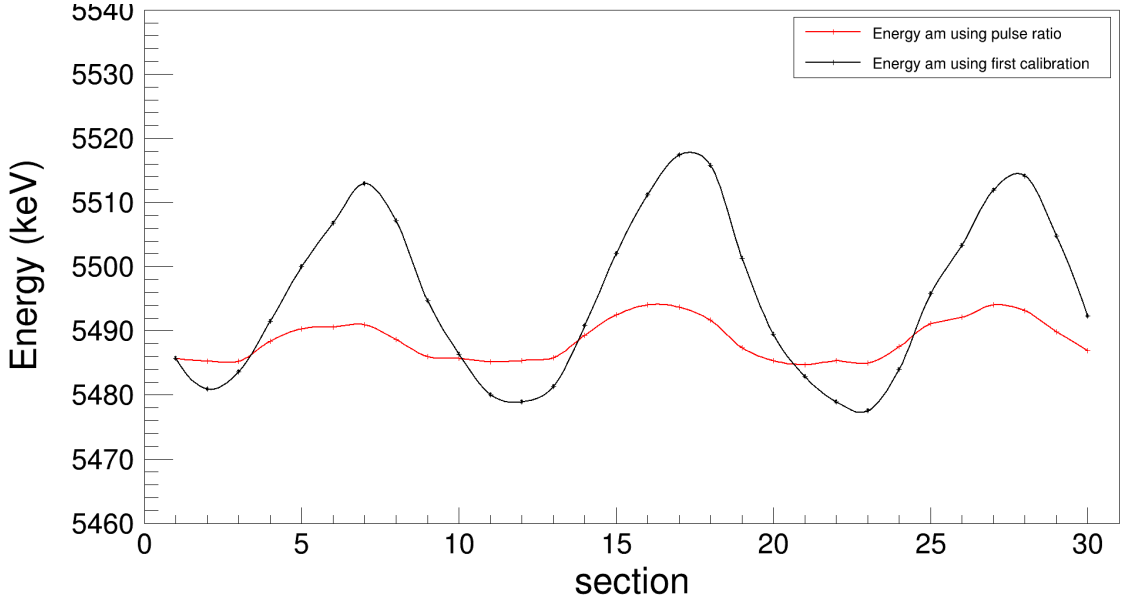


Figure 2.14: Energy of the main alpha decay of the $^{241}$Am with respect to time. The measurements have been splitted into 30 sections of approximately 2 hours. The black curve is the measurement of the alpha energy without any correction and the red one is with the pulser method correction.

The thickness determination is performed by automatically alternating between repeated measurement at the center of the target and eight points on the circle irradiated by the beam (Figure 2.15). As for the growth of the target thickness during beam irradiation, the measured difference between the non irradiated (center of the target) and the irradiated area is lower than 2 $\mu$g/cm$^2$ for all the targets. The measurement allows to measure of the target thickness with uncertainties lower than 10% and a sinusoidal variation of the thickness is observed indicating a linear variation of the thickness with respect to the diameter, as the peripheral points were chosen with equal spacing.

An example of data can be seen in Figure 2.16, the blue points are the measurements

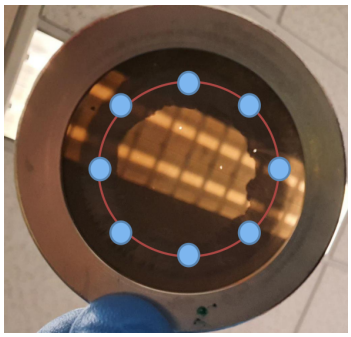

Figure 2.15: Photography of a carbon target after being irradiated by the beam during the 2019 experiment. The points represent the measurements for the thickness of the target.

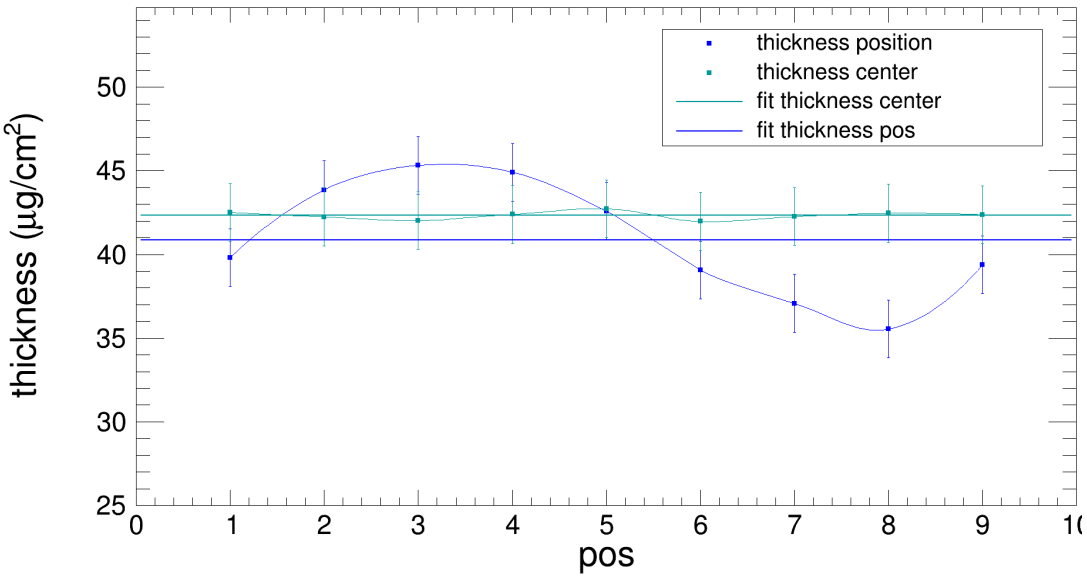


Figure 2.16: Measurement of the thickness of a target in eight positions in a circle on the irradiated area. The ninth one is the measurement, again, of the first position. The blue and green lines are a fin of the measurements using a constant function on the positions and center, respectively.

on the beam spot (circle) and the green points are the measurements in the center of the target. Note that sinusoidal variation have been observed in all the targets measured. To confirm the observation, a measurement with the target in the exact same position but measuring in a circle with a smaller radius have been made, and the results confirm the sinusoidal behaviour but with a smaller amplitude, what was expected in case of a linear variation along the diameter. This observation does not impact the fusion measurement as the target is used rotating, so the effective thickness

of importance by an order zero polynomial, the color of the line corresponds to the measurement fitted (position and center) in Figure 2.16. Note that a first measurement was performed on the production site at GANIL upon fabrication by weighting each target separately.

However, a precise measurement of the thickness of thin targets can be made with this experimental setup, with uncertainties below 10% on the thinnest targets measured, improving the constructor's uncertainties. The measurement in the center of the target shows a difference of the thickness between the center and the beam spot lower that 2 $\mu$g/cm$^2$ demonstrating that the growth of the target thickness is negligible.

### 2.2.4 Accelerator and beam intensity measurement

#### Andromede

The STELLA experiment is based at the Andromede facility [47] at IJCLab in Orsay. It is a 4 MeV electrostatic Pelletron© accelerator from the NEC (National Electrostatic Corporation) company (see photo Figure 2.17). For nuclear physics experiments, it uses an Electron Cyclotron Resonance (ECR) source to ionize the gas and inject it into the accelerator tube. For the carbon beam, the gas used is $CH_4$, to minimize possible contamination in the beam. The ECR source can deliver multiple charge states of the beam ($2^+$ and $3^+$ have been used for the STELLA experiment).

The acceleration process is performed with an electrostatic field generated by friction of chains carrying and depositing electrons along the acceleration tube, creating potential differences and an electrostatic field. To avoid discharging on metal elements of the accelerator, the device is locked in a tank containing isolating gas ($SF_6$) at a pressure arround 6 bar. This accelerator can provide intense beams ($>$ p$\mu$A) with good focusing ($\approx$ 2 mm beam spot on the target). The purity of the beam is ensured by a Wien filter and then a magnetic dipole. The STELLA experiment is installed on a 90° beam line, so that the magnetic dipole will discriminate all the contributions that have a different $(A/C)$ where $A$ is the mass number and $C$ the charge state.

All the experimental setup from the accelerator to the reaction chamber share the same grounding using connected steel plates. This avoids electronic noise in the detectors or in the preamplifiers coming from the accelerator or other devices on the beam lines.

#### Intensity measurement

The knowledge of the number of nuclei involved during the measurement is necessary for the normalization of the cross-sections. This information comes from two contributions, the thickness of the target and beam intensity. The first one is measured as

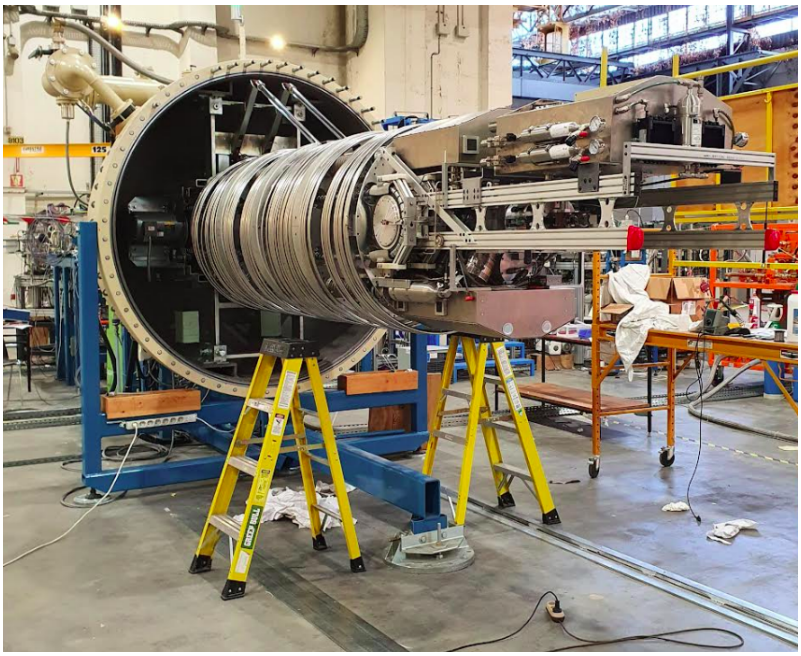

Figure 2.17: Photography of the open Andromede accelerator.

described above in Section 2.2.3, the second one can be measured by monitoring the elastic scattering as explained in Section 2.2.1, or complementary with a current integrator downstream the reaction target at the Faraday cup level. Two of them are used upstream and downstream the reaction chamber (with respect to the beam direction), indicated FC1 and FC2, respectively (see Figure 2.18).

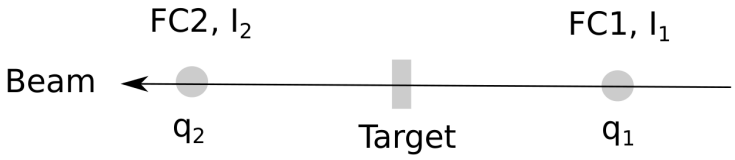


Figure 2.18: Scheme of the Faraday cups system used in the STELLA experiment before and after the target, measuring intensities $I_1$, $I_2$ at charged states $q_1$, $q_2$ [40].

The Faraday cup measures an electric current that depends on the charge state of the beam. An empty frame can be used to check the transmission of the totality of the beam through the chamber, where the two Faraday cup FC1 and FC2 should give equal results for 100% transmission, meaning the beam is fully measured after the target and is not touching anything in between. To convert the current in a number of nuclei, first the charge state has to be considered. It corresponds to the ionization of the beam and is linked to the beam energy. As 1 A = 1 C/s and one charge

$e = 1.602 \times 10^{-19}$ C, the intensity can be converted into a rate by $N/s = \frac{I}{qe}$ with $I$ the intensity, $q$ the charge state and $e$ the electric charge.

In FC2, the measured current is affected by charge stripping of the beam in the target foil, and also a negligible loss of nuclei involved in scattering reactions. The average charge state measured is thus different from the charge state before the target. However, the effect can be corrected using the ratio:

$$\frac{I_1}{q_1} = \frac{I_2}{q_2} \quad \leftrightarrow \quad q_2 = \frac{q_1 \times I_2}{I_1}. \tag{2.6}$$

Thus, the rate can be measured in FC2 after the target using:

$$N/s = \frac{I_2}{q_2 \times e}. \tag{2.7}$$

As the current can fluctuate during the measurement, a digital current integrator (ORTEC®) is used. The mode used during the 2019 experiment generates a signal (one signal gives one count) every $Q_{\mathrm{CI}} = 10^{-8}$ C. So the number of nuclei delivered by the beam on the target is given by:

$$N_{\mathrm{Beam}} = \frac{N_{\mathrm{CI}}}{Q_{\mathrm{CI}} \times e \times q_2}, \tag{2.8}$$

with $Q_{\mathrm{CI}}$ the current conversion ratio and $N_{\mathrm{CI}}$ the number of counts given by the integrator at the end of the measurement. The uncertainties considered for the number of nuclei involved in the measurement, meaning beam and target, is estimated to be 12%, taking into account the uncertainties of the target thickness measurement and the error given by the beam intensity integration devices.

## 2.3 UK-FATIMA

Surrounding the upper part of the STELLA reaction chamber, UK-FATIMA (FAst TIMing Array) [48] detectors measure gammas from the decay of the evaporation residues. The array is composed of 36 $LaBr_3$(Ce) scintillators with an energy resolution that is sufficient and given later in the section. The intrinsic efficiency and the timing resolution are better than for germanium detectors, with a timing depending on the charge collection, and $LaBr_3$ are scintillators, with a sub-nanosecond timing response.

### 2.3.1 $LaBr_3$ (Ce) detectors

The STELLA experiment uses a total of 36 $LaBr_3$(Ce) cylindrical scintillator crystals of a 3.8 cm diameter and a length of 5.1 cm. The light emitted while a particle deposits its energy inside the crystal is detected by a photomultiplier with a diameter of 7.6 cm.

The crystals are encapsulated in aluminum, 2 mm and 0.5 mm thick at the side and the top, respectively (Figure 2.19), to reduce $\gamma$-rays absorption.

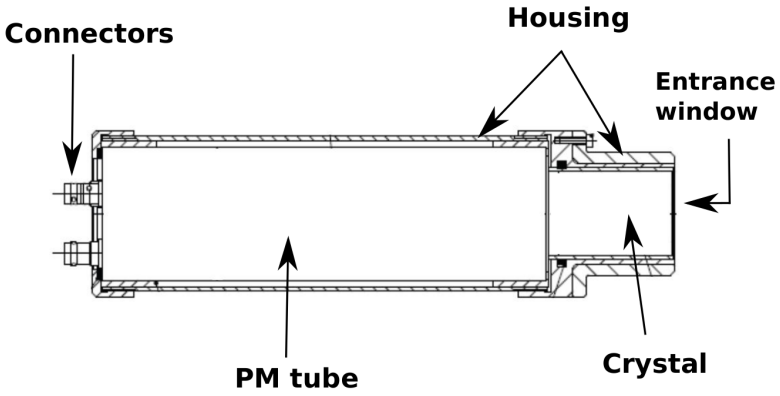


Figure 2.19: Scheme of a $LaBr_3(Ce)$ scintillator [40].

The energy response is generally described by an order two polynomial, but it has been observed in the context of the current work, that the quadratic term is $10^{-6}$ times lower than the linear term in the calibration. The resolution measured is around FWHM = 3% at 1333 keV determined with a $^{60}$Co source [8].

The crystals intrinsically contain radioactive elements, like $^{138}$La and $^{224}$Ac. The first one, with a natural abundance of 0.0902% [49], decays at 66.4% by electron capture into $^{138}$Ba populating a $2^+$ state that decays through $\gamma$-emission at $E_\gamma$ = 1436 keV, and 33.6% through $\beta$ emission populating also a $2^+$ state in $^{138}$Ce, decaying with $\gamma$-emission at $E_\gamma = 789$ keV. The $^{138}$La has a half-life of $T_{1/2} = 1.05 \times 10^{11}$ years, generating around 90 Bq of background per crystal. The $^{224}$Ac and its daughter nuclei decay through alpha emission also at energies between $E_\alpha$ = 1600 keV and $E_\alpha$ = 3000 keV [50]. The decays will be described in more details with the gamma spectrum in Section 3.2.

### 2.3.2 Geometric configuration of the array

Geant4 [51] simulations were utilized to estimate the efficiency of various geometric configurations. Three of them was considered, spherical, cylindrical and a pile configuration with 10 or 12 detectors in the first ring. In the spherical configuration, the detectors face the target, while in the cylindrical and the pile configuration they face the beam line. The acceptance is slightly better for the spherical configuration in both 10 and 12 detectors cases, with 23.3 and 24.4% of $4\pi$, respectively, against 23.1 and 23.2%, respectively for the cylindrical one. The results were obtained using an isotropic $\gamma$ emission at $E_\gamma$ = 10 keV for symmetry reasons and for practical reasons guided by constraints of constructing and assembling the gamma detector array, the

cylindrical configuration was selected to host the $Labr_3(Ce)$ detectors. It is the best compromise between detection efficiency and compactness.

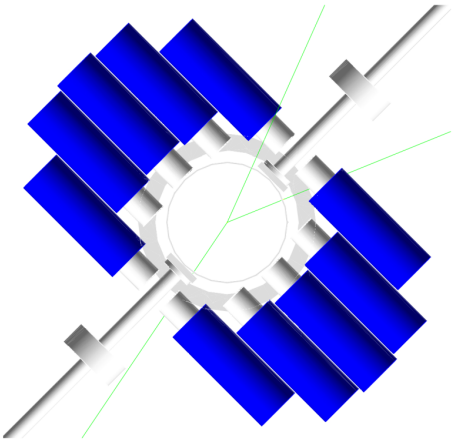

Figure 2.20: Geant4 visualization of the first ring of the cylindrical configuration, with three photons represented by green lignes [40].

The first ring is presented in the Geant4 visualization in Figure 2.20 and a CAD representation can be observed in Figure 2.21. It shows that the configuration was optimised for acceptance as close as possible to the chamber. The results of the Geant4 simulation give the efficiency of the configuration for various gamma energies in two scenarios. The first case considers only multiplicity-one events called $\epsilon_{\text{sing}}$, meaning only one detector measures a signal in a 400 ns interval, and secondly considering higher multiplicity including Compton events where the second emission is measured in another detector summing the energy. The results are summarized in Table 2.1. As the $^{12}C + ^{12}C$ fusion reaction in coincidence focus essentially into the first excited state of the $^{20}Ne$ and $^{23}Na$, $E_\gamma = 1634$ keV and $E_\gamma = 440$ keV, respectively. The relevant efficiencies is are 2.6% and 8.6% [8]. A study of the efficiency at $E_{\text{lab}} = 10.75$ MeV using 28 scintillators made by G. Fruet [40], comparing the $p_1$ and the $\alpha_1$ peak in the particle detectors with and without coincidence selection with their associated $\gamma$-decay yields $2.0 \pm 0.4\%$ for the alpha channel and $6.0 \pm 0.1\%$ for the proton channel, consistent with a simulation using 28 detectors.

The complete STELLA with FATIMA frame is shown in Figure 2.22 as a scheme to understand its full size and the lifting mechanism of FATIMA to access the reaction chamber.

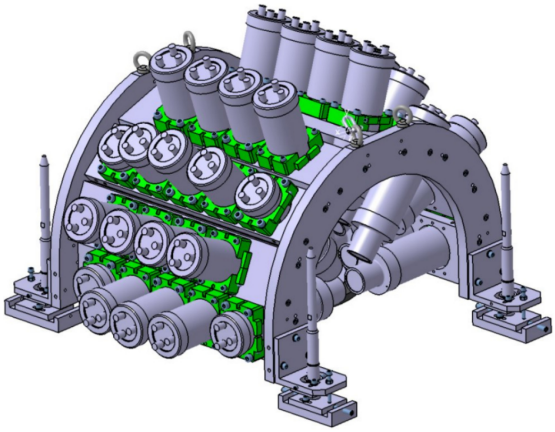

Figure 2.21: CAD representation of the UK-FATIMA detectors on the cylindrical configuration support [40].

Table 2.1: Efficiency of the photoelectric peak with respect to the energy for the complete configuration (36 scintillators) comparing single energy and the sum energy for higher multiplicity events (Compton) [8].

| $E_\gamma$ [keV] | 10 | 440 | 1000 | 1630 | 2000 | 3000 | 4000 | 5000 | 6000 | 7000 |
|---|---|---|---|---|---|---|---|---|---|---|
| $\epsilon_{\text{sing}}$ [%] | 23.1 | 8.0 | 3.5 | 2.2 | 1.8 | 1.1 | 0.7 | 0.5 | 0.4 | 0.4 |
| $\epsilon_{\text{sum}}$ [%] | 23.1 | 8.6 | 4.1 | 2.6 | 2.1 | 1.4 | 1.0 | 0.7 | 0.6 | 0.5 |

## 2.4 Acquisition system and synchronization

The STELLA silicon detectors and the UK-FATIMA scintillators generate signals which have to be evaluated in terms of energy and time by the acquisition chain separately for each type of detector. This section will introduce how the signals are treated to record reliable energy information and also how the time stamp synchronization is made associating to each signal a global time information.

### 2.4.1 UK-FATIMA data acquisition system

A scintillator crystal emits low energy light when ionized by a particle. The light is detected by the Photo Multiplier Tube (PMT) and transformed into an electrical signal. The light enters through a photocathode and is converted into primary electrons cascading through a series of dynodes between which a potential is applied generating an avalanche of electrons to amplify the signal to be read by the acquisition system.

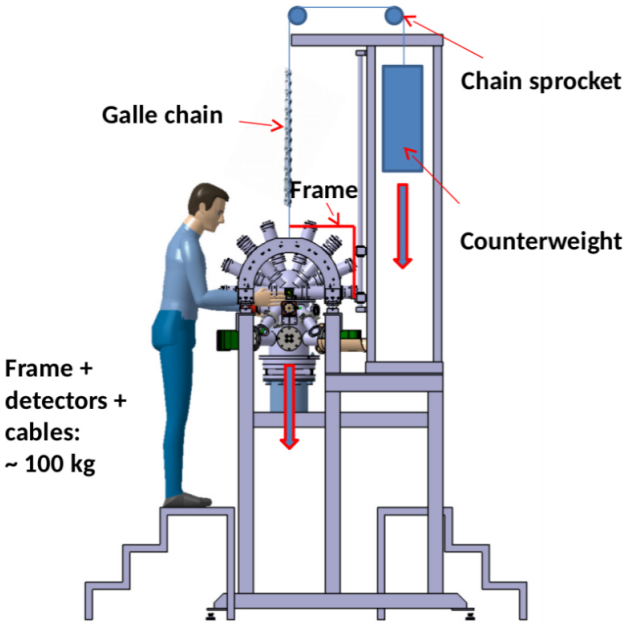


Figure 2.22: Scheme of the full structure of the STELLA experiment with the cylindrical configuration. FATIMA can be lifted with counterweights to access and open the reaction chamber. [40].

A scheme of a scintillator coupled to a PMT is shown in Figure 2.23.

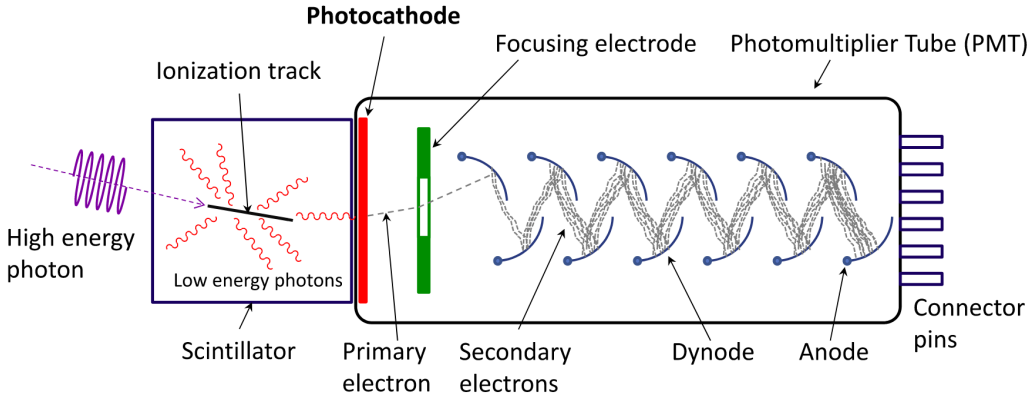


Figure 2.23: Scheme of a scintillator with a photomultiplier, a high energy photon is detected in the crystal, ionizing the material which scintillates emitting low energy photons. The photomultiplier transforms the light into an electrical signal [52].

In the case of the $LaBr_3(Ce)$ detectors, the voltage applied to the PMT is around 1000 V, delivered by a multichannel module from Caen®. Their signals are read by 1 GHz VME-based Caen® V1751 cards. Five cards are used hosting eight acquisition

channels each, that can also receive external triggers and a clock to synchronize it with the STELLA acquisition system. Before the 2022 experiment, they were controlled and read out by the Multi Instance Data Acquisition System (MIDAS) developed by the STFC laboratory (Daresbury, United-Kingdom) [53] and synchronized to the STELLA electronics. During the 2022 experiment, an acquisition software for UK-FATIMA has been implemented into the STELLA acquisition framework [8].

### 2.4.2 STELLA data acquisition system

The detectors inside the STELLA reaction chamber are silicon semiconductors. The substrate of the detector is polarized with a -60 V potential difference applied in the junction side (strips) depleting the substrate. A simplified scheme of the process is shown in Figure 2.24, where the trajectory of the particle is indicated by the black line, creating electron-hole pairs along the path. The charges migrate in the electrical field of the detector and are collected at the electrodes. The signal is generated by the potential difference created by the avalanche of charges.

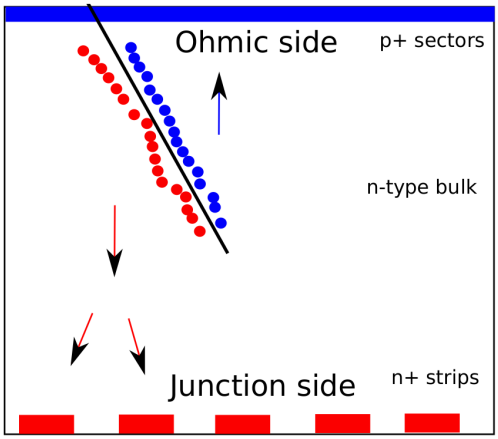


Figure 2.24: Simplified scheme of a polarized silicon particle detector [40].

The signal generated is amplified in the differential preamplifier and transformed from differential to single ended signal in converter electronics. A typical signal is shown in Figure 2.25. The rise time corresponds to the charge collection in the strips and is generally between 80 and 120 ns. The amplitude depends on the energy of detected the particle. The fall time is the discharge of detector following an exponential tendency and is in general between 15 and 20 $\mu$s.

The pre-amplified signal is then sent to the STELLA data acquisition system that was developed by the technical group "Système de Mesure et d'Acquisition" at IPHC. It is composed of a commercial ABACO® 125 MHz $\mu$TCA crate hosting 8 FMC112

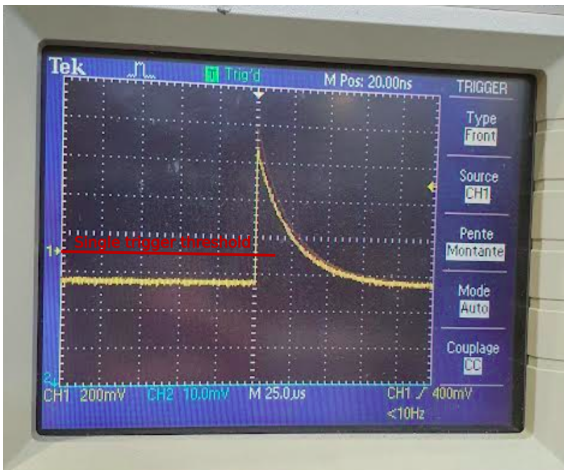


Figure 2.25: Photography of an oscillogram showing a typical signal in the S3F detector obtained with a triple-alpha source.

cards, containing 12 ADC channels each for a total of 96 channels. The cards are grouped two by two using FC7 Advances Mezzanine Card (AMC) mother boards [54], capable of single ended signals up to ±2 V. One of the FC7 AMC card is used for each S3 and S1 detectors and the last one is employed for the two monitors and the beam integrator.

A comparably fast way of triggering the acquisition process is with a threshold on the amplitude. Then the amplitude of the signal crosses the threshold, the timestamp and trigger number is stored and accepted for the acquisition process. However, this method is sensitive to the slow decay of the signal in the detector, and thus sensitive to baseline fluctuations.

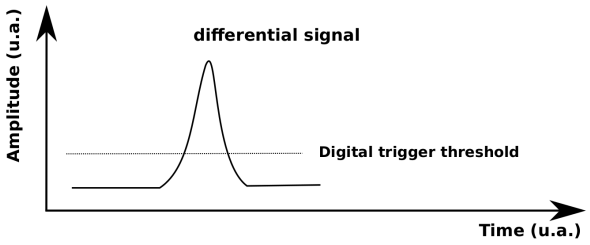


Figure 2.26: Differential signal compared to the Digital trigger threshold [40].

The STELLA acquisition system uses instead a digital trigger that consists of the differentiation of the signal by applying a timing delay and the signal is subtracted from the non-delayed signal. It then is integrated on definite number of samples, with a size adjusted in the acquisition software. The integration can drastically reduce the dependency of the baseline fluctuations. Then the triggering depends on a threshold

set by the user as shown in Figure 2.26. The deadtime of the acquisition is reduced with this method by optimizing the integration window of the signal [40].

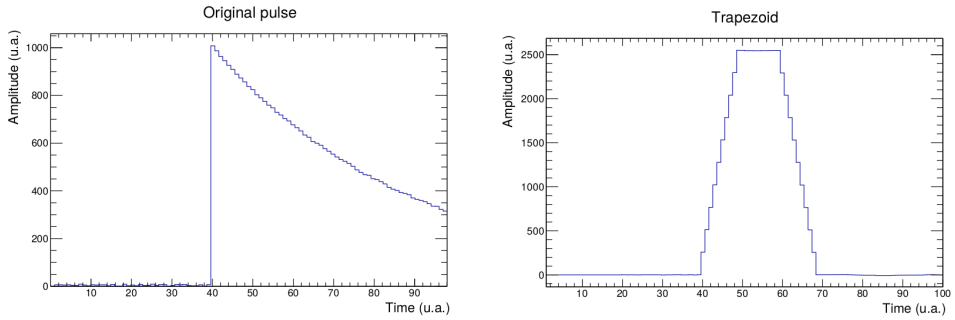


Figure 2.27: Typical pulse on the left transformed into a trapezoid signal using the Jordanov algorithm [55] on the right side. The amplitude of the signal is computed comparing the plateau of the trapezoid and the baseline [40].

This process is continuously done by the software with an 8 ns sample rate. If the threshold is reached, the signal is treated with the Jordnov algorithm [55] transforming the single ended signal into a trapezoid signal. The trapezoid shape depends on the rise time and amplitude of the single ended signal and the energy is determined from mean value on the trapezoid plateau and the mean value of the base line within a fixed time interval. A digital gain can be added depending on the reaction and the energy studied (see Figure 2.27).

### 2.4.3 STELLA and UK-FATIMA synchronization

The time synchronization is made by a Gigabit Link Interface Board (GLIB) card hosted by the same $\mu$TCA module as the FC7 cards from the STELLA acquisition system. It generates a 10 MHz clock delivered to the FC7 cards that convert it into a 125 MHz sinusoidal signal, and transmit it to the 8 FMC112 cards. One of the FMC112 cards transmits the clock to the UK-FATIMA acquisition on the first V1751 QDC, that passes the signal to the 4 other cards in a chain (see Figure 2.28) [8].

The 125 MHz clock for the STELLA acquisition is adapted to the response time of the silicon detector, with ping every 8 ns providing a time precision approximately 4 ns. The scintillators have a much faster timing resolution than semiconductor detectors ($\leq$ 1 ns), so the 1 GHz clock is mandatory to reach a precision adapted to thin timing resolution.

The scheme in Figure 2.28 shows the clock from the GLIB card synchronizes all QDC cards, that have internal clock (125 MHz for STELLA and 1 GHz for FATIMA).

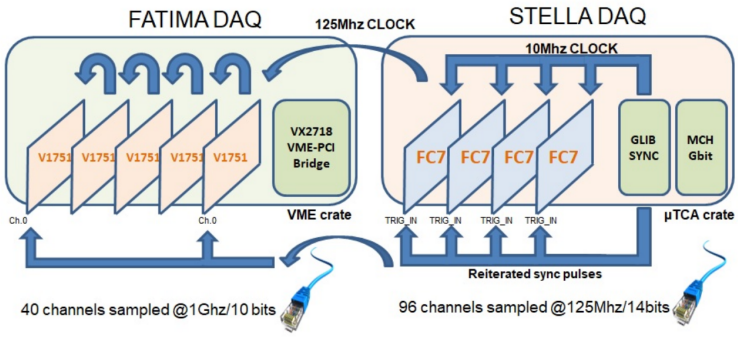


Figure 2.28: Scheme of the synchronization system between the STELLA and the FATIMA electronics. It shows how the clock from the GLIB card synchronizes all acquisition cards using a 10 MHz signal [8].

Those internal clocks can have a starting delay upon launch, that can rise up to 1 s. It will be a constant and controlled offset, that is determined by a synchronization signal on a dedicated readout channel transmitted to all cards every 15 min.

With this global time stamp synchronization, event data bears information of the channel it has been measured, its energy and its timestamp. Some bits are dedicated to tag saturated signals ($> 2$ V) and pile up (too high counting rate).

Figure 2.29 shows a scheme of the time synchronization system between the STELLA and the FATIMA clocks where $t_{0(lab)}$ represents the starting time of all the acquisition, and $t_{0(g)}$ and $t_{0(p)}$ represents the start of the internal clock of the FATIMA and STELLA cards, respectively. The time when the synchronization signal from the GLIB card is sent to all the clocks is represented by the red arrow and illustrated by the dashed line on the timelines of the clocks giving $t_{sync(lab)}$, $t_{sync(g)}$ and $t_{sync(p)}$. The timestamp of the three clocks and the offset is simply $t_{sync(g)} - t_{sync(p)}$. The time calibration can be made with the offset and coincidences between the events can be made between gamma and charged particles, but also gamma-gamma and particle-particle, for the reconstruction of Compton events or charge sharing events. Considering the acquisition deadtime, a window of 400 ns is used for the event reconstruction. The timing window of truly coincident (fusion) events is indeed much shorter as explained in the next Chapter.

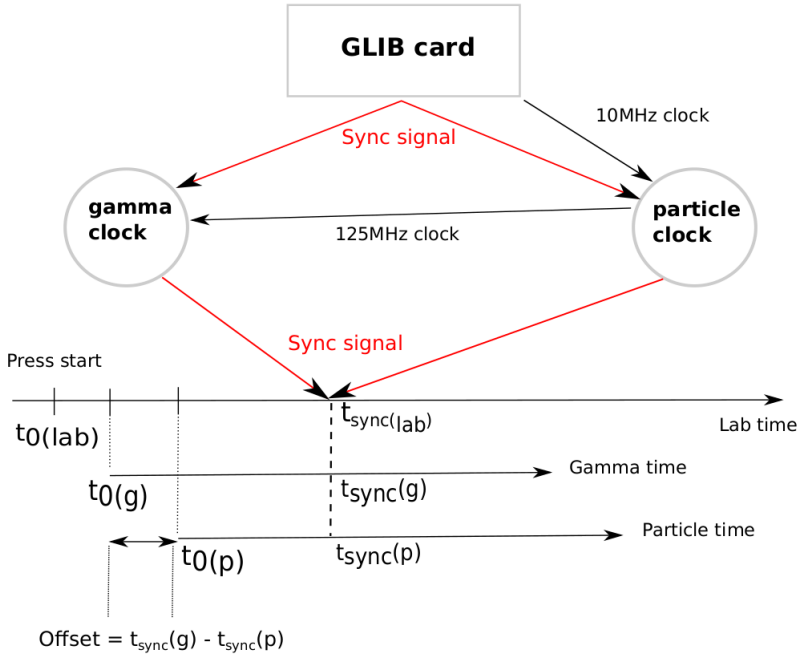


Figure 2.29: Scheme of the time synchronization system between the STELLA and the FATIMA electronics. It shows how the clock synchronization is made with the consideration on the starting delay of the internal clocks [40].

## 2.5 Résumé chapitre 2

Différentes techniques ont été utilisées pour mesurer de façon directe les réactions de fusion $^{12}C + {}^{12}C$, des mesures distinctes mesurant soit les particules chargées, soit les gammas de désexcitation, ou des mesures en coïncidences, mesurant les particules chargées et les gammas de désexcitation en simultané. Dans le cas des mesures distinctes de particules chargées, des cibles fines de carbone sont utilisées et les particules chargées sont mesurées dans des détecteurs en silicium protégés par de fines feuilles d'aluminium ou de nickel. Ces techniques ont l'avantage de pouvoir mesurer de très nombreuses voies de désexcitation et leurs rapports d'embranchement (jusqu'à $p_{16}$ et $\alpha_{12}$ pour Becker *et al.*[17]). Cependant, aux énergies profondément sous coulombiennes et d'intérêt astrophysique, la statistique chute exponenciellement et la mesure est sujette à un bruit de fond dominant, provenant notamment de réactions parasites avec des contaminants présents dans la cible ($d$ et $^1H$ majoritairement). Pour la mesure distincte des gammas de désexcitation, des cibles fines et épaisses peuvent être utilisées. Dans les cibles épaisses, le faisceau peut perdre toute son énergie et la mesure va intégrer des réactions de l'énergie du faisceau jusqu'à zéro. Les mesures sont donc effectuées variant l'énergie pas à pas. Aux basses énergies, les spectres sont très sensibles au fond Compton de contributions venant de la radioactivité ambiante ou de réactions parasites.

La technique de mesure en coïncidences a été introduite en 2018 dans le cadre de mesures d'intérêt astrophysique. Cette technique consiste en la mesure de particules chargés et des gammas de désexcitation des noyaux fils en simultané. Bien que réduisant la statistique par rapport à une mesure distincte, la technique permet une forte réduction du bruit de fond et une identification des évènements plus précise à l'aide de conditions de sélection. Ainsi, les réactions issues des contaminants sont supprimées et des sections efficaces plus précises peuvent être extraites.

L'expérience STELLA (STELlar LAboratory) utilise une technique de coincidence. Elle utilise une chambre à réaction contenant quatres detecteurs en silicium pour les particules chargées issues de la fusion, deux moniteur pour mesurer la diffusion élastique, un support de cible portant trois cibles rotatives, six cibles fixes et un cadre isolé électriquement pour vérifier la focalisation du faisceau et un système de pompage composé d'une pompe sèche primaire et d'une pompe cryogénique permettant d'atteindre un vide de $P \approx 10^{-8}$. Les détecteurs pour les particules chargées sont des semiconducteurs en silicium, Un de type DSSSD (Double Sided Striped Silicon Detector) S1 et deux de type DSSSD S3, le substrat Si provenant de Micron Semiconductor Ltd et monté sur des supports PCB ROGER à l'IPHC. Un détecteur vient les compléter depuis 2022 appelé PIXEL, pouvant utiliser soit un BB10, soit un SUPER-

X3 de Micron Semiconductor Ltd, qui sont des détecteurs en silicium donnant une indication sur la position où la particule a touché le détecteur, le premier avec huit pistes contre quatre pour le second, qui aura pour lui une résolution temporelle bien meilleure, dépendemment des besoins (précision angulaire ou timing plus précis). Ces détecteurs couvrent les angles de 122.4° à 141.8°, 10.4° à 30.3°, 148° à 159° et 45° à 90°, respectivement.

Les moniteurs utilisés habituellement sont des détecteurs en silicium à barrière de surface. Ils mesurent des données provenant de la section efficace de Mott de la diffusion élastique. Dû aux deux bosons identiques dans l'état initial et l'état final, la section efficace présente des interférences (Figure 2.9), ainsi la position du détecteur est à 45° à 23 cm de la cible, collimaté par une ouverture de 1 mm de diamètre. En plus de servir à la normalisation, ils permettent de monitorer d'éventuels changements de focalisation ou de transmission du faisceau dans la chambre à réaction, ou encore de vérifier l'état de la cible.

Les cibles rotatives utilisées sont épaisses de 20 à 80 $\mu g/cm^2$, fixées sur un cadre circulaire de diamètres intérieur et extérieur de 46 et 63 mm . La rotation est assurée par un moteur couplé magnétiquement à la chambre à réaction pouvant faire tourner les cibles juqu'à 1000 rpm, afin de dissiper la chaleur générée par la perte d'énergie du faisceau dans la cible. L'épaisseur des cibles est remesurée après expérience dans une station de mesure développée à York en collaboration avec l'équipe de STELLA et a été améliorée à l'IPHC afin d'atteindre une précision de mesure inférieur à 10%. Pour cela, des améliorations ont été apportées sur la chambre et une technique de suivi de l'évolution du gain du préamplificateur a été développée. Ces mesures ont révélé que l'épaisseur de la cible n'était pas augmentée au niveau du passage du faisceau sur la cible, et une variation sinusoidale de l'épaisseur suivant un cercle sur la cible, indique une variation linéaire de l'épaisseur sur le diamètre, ce qui n'a pas d'impacte sur notre mesure.

Le faisceau est généré par l'accélérateur Andromède, un accélérateur électrostatique Pelletron© de 4 MV muni d'une source ECR qui ionise du $CH_4$ avant de l'envoyer dans le tube accélérateur. La pureté du faisceau est assurée par un filtre de Wien et un aimant à 90°, angle auquel est placée la ligne occupée par STELLA. L'intensité du faiseau est mesurée dans une cage de Faraday située derrière la chambre et le courant généré est intégré par un intégrateur de courant Digital ORTEC®.

Enfin, les rayonnements gammas sont mesurés par les 36 scintillateurs $LaBr_3$(Ce) de la collaboration UK-FATIMA (FAst TIMing Array). Ces scintillateurs ont une résolution suffisante (FWHM = 3% à 1333 keV), une bonne efficacité de détection, et surtout un temps de réponse inférieur à la nanoseconde. Ils sont sujets à une radioactivité interne comprenant de la radioactivité gamma, bêta et alpha, permettant une

auto-calibration pour parer aux variations de température au cours du temps. La configuration utilisée est une configuration cylindrique où l'ensemble des détecteurs font face au faisceau, permettant un montage plus simple qu'une configuration sphérique et permettant tout de même une efficacité de 8.6% pour la mesure du premier état excité du $^{23}$Na (440 keV) et 2.6% pour celui du $^{20}$Ne (1634 keV).

Pour une mesure en coïncidences, la synchronisation temporelle de ces détecteurs est nécessaire. D'un côté, nous avons des détecteurs semiconducteurs : lorsqu'une particule chargée interagit avec le détecteur elle génère des électrons trous dans celui-ci et les chargent migrent pour être récoltée. Ces signaux électriques sont amplifiés avant d'être traités dans les cartes d'acquisition FMC112, elles-mêmes gérées par des cartes mères FC7 AMC. Ces cartes sont disposées dans un boitier $\mu$TCA ABACO® muni d'une horloge de 125 MHz. Les scintillateurs délivrent un signal lumineux transformé en signal électrique et amplifié par les photomultiplicateurs. Ce dernier est beaucoup plus rapide et les signaux sont traités par des cartes VME V1751 de Caen® ayant une horloge interne de 1 GHz. La synchronization est faite avec une carte Gigabit Link Interface Board (GLIB) Transmettant un signal horloge de 10 MHz délivré aux cartes mères FC7 pour les synchroniser. Enfin l'une d'elles transmet un signal horloge de 125 MHz en chaine aux cartes VME de l'acquisition de UK-FATIMA. Toutes les cartes ne démarrant pas à la même vitesse, un signal de synchronisation envoyé toutes les 15 minutes permet la synchronisation temporelle exacte de toutes les horloges comme expliqué sur la Figure 2.29. Le temps mort de l'acquisition et donc le temps considéré pour les coïncidences est de 400 ns.

# Chapter 3

# Data analysis

In this chapter the extraction of the fusion cross-section from the experimental data is discussed. As described in the previous Chapter (2), the STELLA experiment is based on coincidences of two types of detectors, scintillators to measure gammas from de-excitation of the daughter nuclei, and silicon detectors inside the reaction chamber to measure evaporated charged particles. First, the charged particles spectra will be introduced with explanations of the different reactions and the decomposition of the signals to have the best understanding of it and extract valuables information from the detector. Then, details about the scintillators signals will be given, and the optimization resulting in sharp timing precision is described. The coincidences events are selected with three conditions, the gamma energy, the particle energy and the time difference between the two measurement. The selections rules are explained for all conditions.

## 3.1 Charged particle detection

This section is dedicated to the particle detection, reminding that the $^{12}C + ^{12}C$ fusion reaction in nuclear astrophysics for the carbon burning phase happens mainly through the two exit channels :

$$^{12}\mathrm{C} + {}^{12}\mathrm{C} \rightarrow {}^{24}\mathrm{Mg}^{*} \rightarrow {}^{23}\mathrm{Na} + p + \gamma, Q = 2.24\ MeV \tag{3.1}$$

$$^{12}\mathrm{C} + {}^{12}\mathrm{C} \rightarrow {}^{24}\mathrm{Mg}^{*} \rightarrow {}^{20}\mathrm{Ne} + \alpha + \gamma, Q = 4.62\ MeV \tag{3.2}$$

The silicon detectors (DSSSD) measure protons and alpha particles in terms of energy, angle, and time stamp, for a given beam energy and via proton and $\alpha$ discrimination.

### 3.1.1 Reaction kinematic spectrum

Figure 3.1 shows a 2D spectrum of the S3F detector at $E_{\mathrm{cm}} = 5.34$ MeV (data taken in the first campaign in 2016-2017)[37], polar angle *versus* the energy. The binning for $y$-axis corresponds to a bin for each strip of the detector and respect the angular coverage of it. The lines correspond to kinematic calculations of the particle energy[16], black for the $\alpha$ channel and red for the proton channel, while the blue ones represent the background reaction : $^{12}\mathrm{C} + \mathrm{d} \rightarrow {}^{13}\mathrm{C} + \mathrm{p} + \gamma$. Starting from the right, the ground state $\alpha_0$ (see equation 3.2) and the first excited state $\alpha_1$ are visible. The two protons lines, $\mathrm{p}_0$ and $\mathrm{p}_1$ don't show in the experimental data, because the associated protons have too much energy to be fully stopped in the detector. The latter can nevertheless be measured in the backward detector (S3B) Figure 3.2. This only affects the highest beam energies ($E_{\mathrm{cm}} > 4$ MeV), and for the data set analysed during this work, this effect with thus not be present.

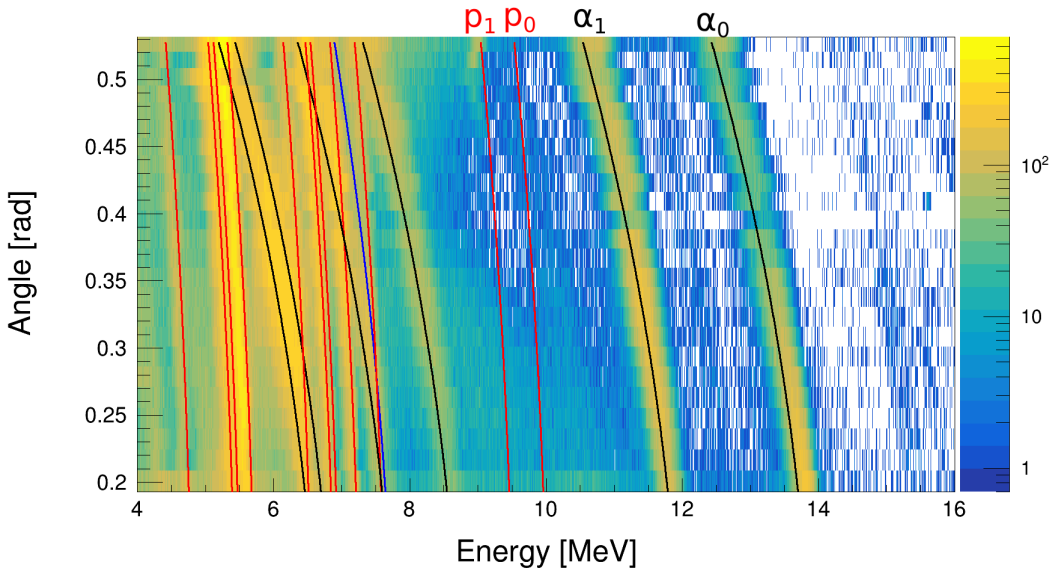


Figure 3.1: Angular differential energy spectrum in S3F at $E_{\mathrm{cm}} = 5.34$ MeV. Red and black lines represent the kinematics calculation for the proton and alpha channel, respectively, and the blue ones represent the reaction on the deuterium contamination.

These spectra are predominantly composed of multiplicity-one events, i.e the entire energy is deposit in only one strip. However, the analysis of multiplicity-two events gives insight into background contamination in the spectra. Multiplicity-two events are two signals in the detector measured at the same time (in a 400 ns range). Generally one can consider two different types of multiplicity-two signals. As a S3F or S3B detector contains 24 rings that can be considered as detectors themselves, charge

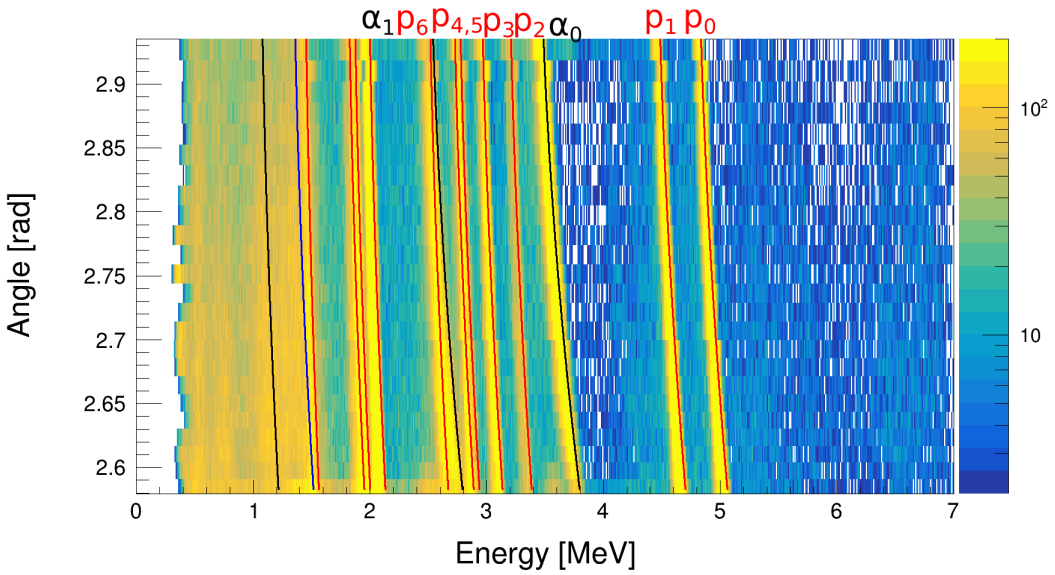


Figure 3.2: Angular differential energy spectrum in S3B at $E_{\mathrm{cm}} = 5.34$ MeV. Red and black lines represent the kinematics calculation for the proton and alpha channel respectively, and the blue ones represent the reaction on the deuterium contamination.

sharing between two strips can occur, in particular when measuring alpha particles. An electron avalanche is generated by the particle when it interacts with the detector. The figure 3.3 represents a scheme of three strips in the detector, labeled A, B and C. In the left case, the electron cloud generated by the charged particle is confined to one strip. On the opposite, in the right case, the particle hits the detector between strips B and C so that the electron cloud is collected by both strips. The charge distribution is illustrated in the diagram on the right, most of the signal is collected by the strip B. To reconstruct the total energy, it is therefore required to sum up the two signals. The second type of multiplicity-two signals occurs when two particles of different origin hit two different strips of the detector within a 400 ns interval. In that case, all signals have to be considered independently.

The first and more efficient way to disentangle both effects is to consider interactions with the detector. Charge sharing will only occur in neighbouring strips, while simultaneous detection of two independent particles can occur in any combination of couples of strips. As shown in the Figure 3.4, separating multiplicity-two events in those two categories already cleans the spectrum significantly from miss-identified events. The Figure 3.4 shows three spectra, a spectrum without any treatment containing sum energies of multiplicity-two events in black, the blue spectrum contains only multiplicity-one events and the red one only multiplicity-two events without any

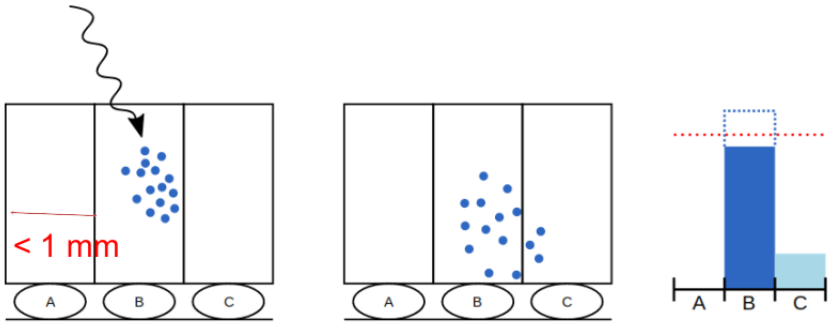


Figure 3.3: Simplified view of the charge sharing, 3 strips are drawn, and the points represents the electron cloud generated by the interaction of a charged particle in the detector. On the left, no charge sharing occurs while on the right there is charge is distributed over two strips. The diagram on the right represents the amount of charges collected by every strip in the latter scenarios

selection (sum energy). It shows first that most of the events are multiplicity-one, while multiplicity-two represents only 10% of the counts for alpha particles and less for protons. The spectra show similar features and structures above 6 MeV but between 3 and 6 MeV, the multiplicity one and multiplicity-two spectra look very different. In this energy region the multiplicity-one spectrum isn't disturbed by summing effect of random simultaneous signals. As in this plot the multiplicity-two spectrum is only the sum of energy without any treatment, it is sensitive to miss-identified events. The peak around 3 MeV is present only in the total spectrum and the multiplicity-two spectrum. This means that this structure contains exclusively non charge-sharing events. It results from the addition of proton events from $p + {}^{12}C$ elastic scattering, ${}^{12}C$ from the beam and proton events from the water contamination inside the target, and a low energy noise. The subsequent analysis will help understanding in detail how multiplicity-two events impact the spectrum.

In the Figure 3.5 are only represented multiplicity-two events. In black can be observed the sum energy spectrum without any treatment, the neighbour strips sum energy in red and the non-neighbour strips single energy in blue. A similar comparison in Figure 3.4, above 6 MeV, explains that most of the multiplicity-two events are from neighbouring strips. But for the region below 6 MeV, strong differences between the black and the red curve appears. In particular between 4 and 6 MeV, where the typical energy of two protons from elastic scattering previously mentioned in this energy range, are hiding the peaks from higher excited state events from the fusion reactions. This method is efficient to help dissociate signals from fusion reaction making a charge sharing signal in the detector and signals of two random particles

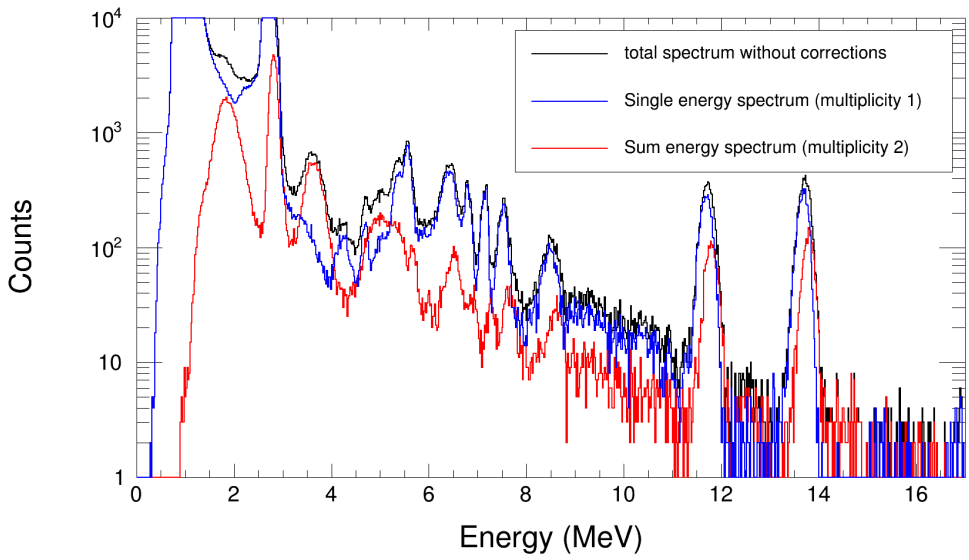


Figure 3.4: Typical energy spectra of one strip in S3F. Blue is multiplicity-one events only, sum energy multiplicity-two events in red and the black is the addition of blue and red.

hitting the detector in a given time interval. However, random simultaneous particles can also be distinguished when appearing in neighbouring strips.

For a charge-sharing event, the energy measured in both strips is summed to reconstruct the real energy of the particle, that can be described by the calculation of the reaction kinematics, while random multiplicity-two events will reconstruct peaks in the spectrum that are not associated with real events. Figure 3.6 shows the correlation of energies in multiplicity-two events in neighbouring strips. The diagonal bands $Q_0 = x + y$ correspond to all charge sharing combinations for a given energy deposit $Q_0$. Those lines contain mostly charge sharing events as they are clearly correlated. In the vicinity of energies of the proton elastic scattering around 2.7 MeV in each strip, a blob in the middle of the diagonal band is visible. This blob is from two protons events with the same energy. The band is detailed in Figure 3.7 in order to estimate the amount of protons from elastic scattering in it, with respect to the signal.

Figure 3.7 shows the energy differences $\frac{1}{\sqrt{2}}\sqrt{E_1 - E_2}$ in the energy band of 5.4 MeV. The data are fitted by a gaussian on a linear background. The background represents the charge-sharing events while the gaussian is generated by the two protons within a 400 ns time interval in neighbour strips. To understand the impact of this contribution, an energy selection within three sigmas of the gaussian is made and the spectrum is corrected with a ratio between the linear and the gaussian contributions in this energy range. For the events with protons from elastic scattering and a signal from $^{12}C + ^{12}C$

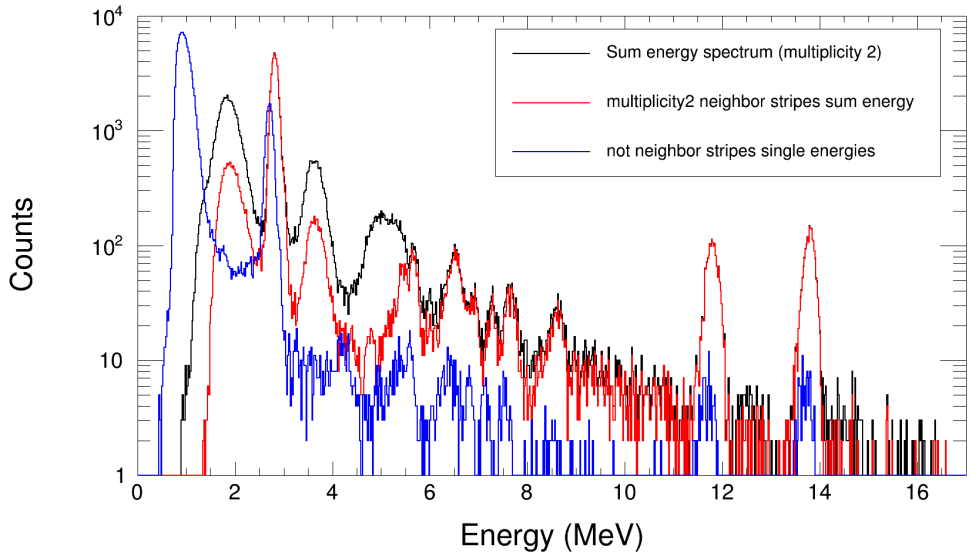


Figure 3.5: Energy spectra of multiplicity-two events only of one strip in the S3F detector. Three spectra are shown : total multiplicity-two spectrum with the sum energy in black, multiplicity-two events in non-neighbour strips single energy in blue and sum energy events in neighbour strips in red.

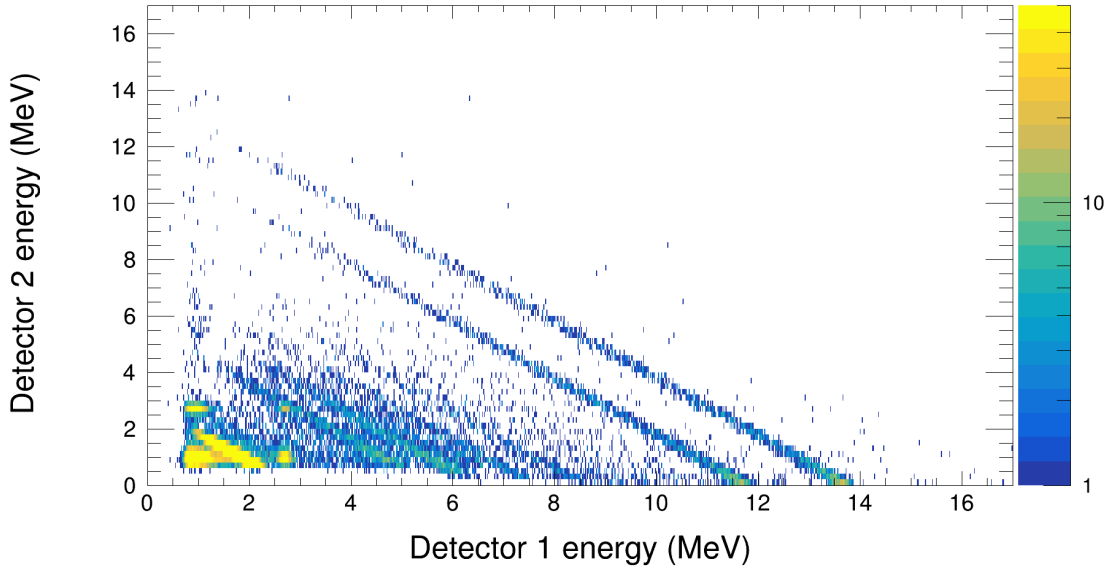


Figure 3.6: Correlation of particles energies for multiplicity-two events. The diagonal bands correspond to charge sharing of characteristic $\alpha$- or p-energies for $^{12}C + ^{12}C$ fusion reactions.

fusion reaction, there is no specific discrimination in neighbour strips. But as shown in the Figures 3.4 and 3.5, their contribution amounts to less than 10% of multiplicity-two events. These are non charge-sharing events in neighbour strips. Considering the 24 strips in the detector, it can be estimated that the amount of those events is 22 times less significant in neighbour strips. So comparing that to the entire spectrum, where multiplicity-two events represents less than 10% of the total data, one can consider also that less that 1% divided by 22 can be neglected. This approximation is made in the inner part of the detector, the cross-section of $^{12}$C + p elastic scattering depends on the angle and the beam energy. Even with an order of magnitude difference, the phenomenon is still negligible. It should be noted that the discussed corrections in the sum energy spectrum are far from the $\alpha_0$, $\alpha_1$, $p_0$ and $p_1$ energies, that are the main focus of this work. At lower beam energies, the elastically scattered particles are stopped in the aluminum protection foil of the detector and do not affect the measurement anymore.

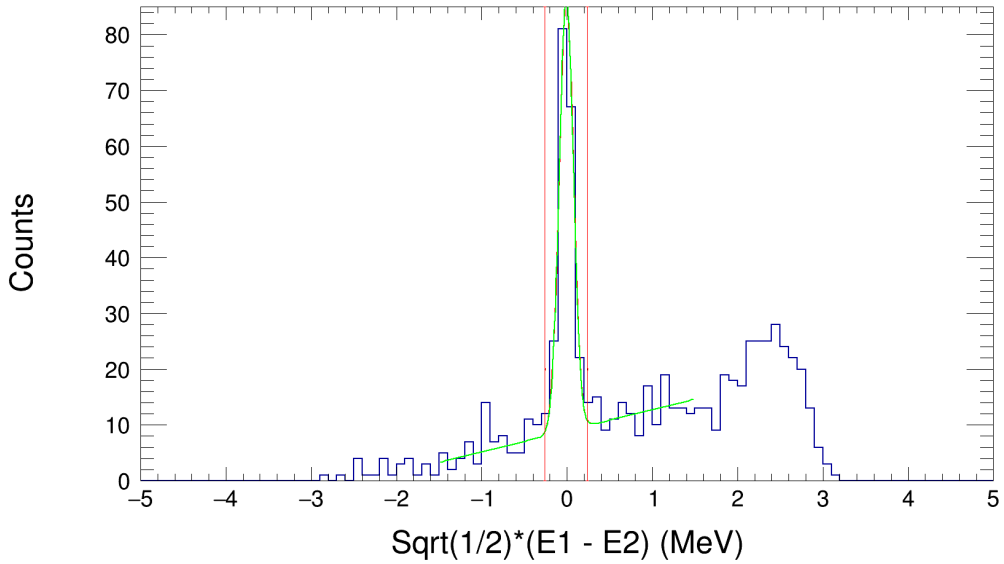


Figure 3.7: Energy difference in 5.4 MeV band containing elastic scattering and charge sharing. The fit yields an estimation of the background contribution

Charge sharing and simultaneous detection of multiple particles can be identified by dissociating non neighbour strips, and correlation of energy in neighbour strips. These effects are summarized in Figure 3.8, where the spectrum without any corrections is shown in black, the spectrum cleaned with the neighbour - non-neighbour method in red, and in green with the ratio correction in neighbour strips for the two protons from the elastic scattering. The differences between the red and the green curve are

negligible, with only minor deviations around 5 MeV. On the other hand, the difference between those two spectra and the spectrum without corrections is significant, in particular between 4 and 6 MeV where peaks belonging to $p_{i,j}$ transitions are very well-defined in the cleaned spectrum.

Another aspect of the random coincidences is shown in this Figure at energies higher than 14 MeV. This can be interpreted in termes of peak at 13.5 MeV plus a background event or an elastic scattering proton. It is most likely the latter, but those events represents less than $\frac{1}{1000}$ of the events from the peak ($\alpha_0$) and then can be neglected.

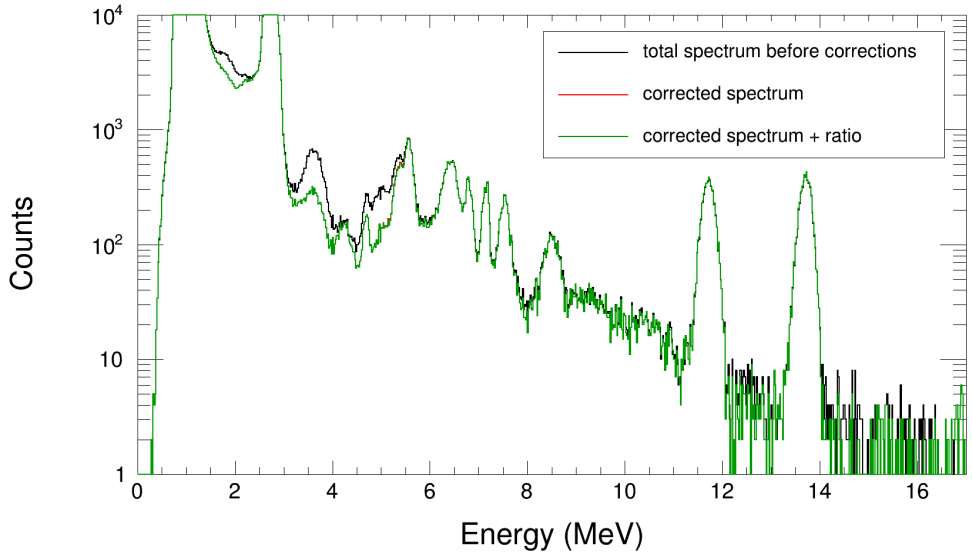


Figure 3.8: Comparison between the energy spectrum without and with neighbour corrections in black and red respectively, neighbour corrections with the addition of the ratio correction in neighbour strips presented in Figure 3.7 in green.

### 3.1.2 Angular differential cross sections

For high statistics runs, cross-sections can be extracted separately for every strip of the particle detectors. Each strip corresponds to an angle, with a definite coverage. This allows for the extraction of differential cross-sections and the interpretation of angular distributions of the light charged particles using equations 3.1 and 3.2. They can be fitted with a Legendre polynomial to extract information on the angular momentum taken away by the evaporated particle and to eventually deduce information on the state populated in the compound nucleus before evaporation.

Most of the investigated angular distributions only show linear behavior meaning they only can be fitted with the order zero of the Legendre polynomials. Nevertheless the ground state transition of the $\alpha$-channel ($\alpha_0$) shows large variations in the cross-section with respect to the angle in the center of mass system. To fit the results with Legendre polynomials, only even orders are allowed for the $^{12}$C +$^{12}$ C fusion reaction, due to angular momentum conservation of the two $0^+$ nuclei.

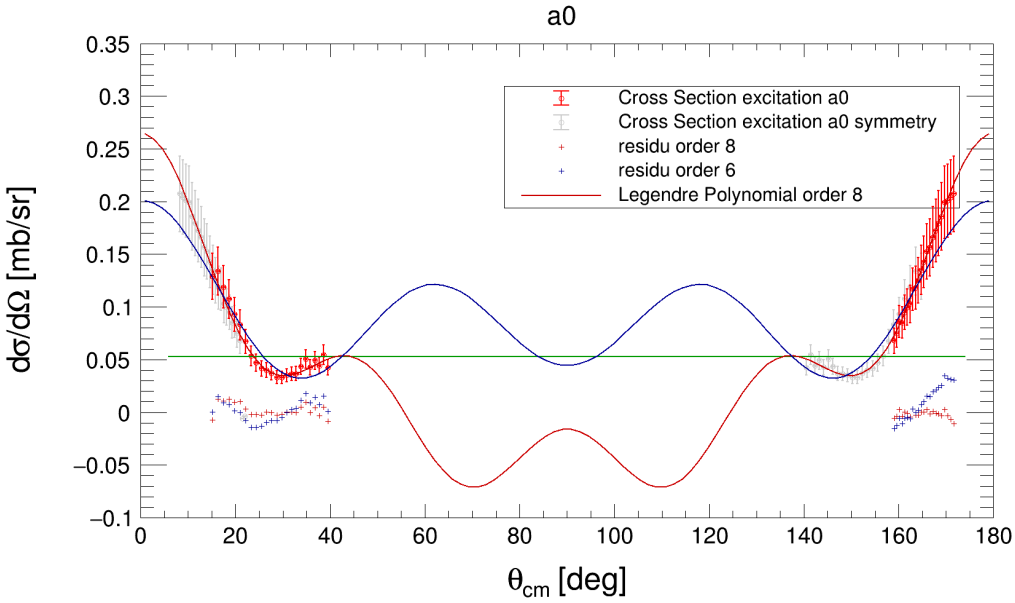


Figure 3.9: Angular distribution of the differential cross-section for $\alpha_0$ at $E_{\text{lab}} = 10.75$ MeV. The red data points represent the measured made with S3F and S3B and the grey points are the mirrored points of both detectors with respect to $\theta_{\text{cm}} = 90^{\circ}$. The green, dark blue and red curves corresponds to Legendre Polynomials of orders zero, six and height respectively. The dark blue and red crosses in the lower panel are the fit residue for the polynomials of order six and eight respectively.

The value of the highest order of the Legendre Polynomial $k_{max}$ in equation 1.19 ($\left(\frac{d\sigma}{d\Omega}\right)_{\text{cm}} = \sum_{k=0}^{k_{max}} a_k P_k(\cos\theta_{\text{cm}})$) is determined by the condition $k_{max} \leq \min(2I \equiv 2l_i, 2l_e)$ where $I(l_i)$ is the compound state's angular momentum and $l_e$ the angular momentum involved in the exit channel [17]. It means that measuring the angular momentum involved in the exit channel restricts the possibilities of the spin of the state populated in the compound nucleus. Another interest of the Legendre polynomial fit is the extraction of the total cross-section for a specific state and exit channel by $\sigma_{tot} = 4\pi a_0$, that corrects for possible angular distributions.

The figure 3.9 shows the differential cross-section for the ground state of the $\alpha$-

channel. The red data points represent the measurements in the different strips of the detectors S3F and S3B. The grey points are the complements of the red points with respect to 90°. The three curves represent Legendre polynomials at orders zero (green), six (dark blue) and eight (red) and the red and dark blue crosses are the residue ($\sigma_{exp} - \sigma_{leg}$) for the orders eight and six respectively. The order eight fits the best the data. A lack of data around 90° limits the accuracy of determining the parameters of leading orders. Therefore, an additional detector, PIXEL, was added to cover polar angles between 60° to 90°. The detector was commissioned during the experiment in 2022 and the analysis is in progress.

As presented in the Chapter 2.2,the addition of the PIXEL detector aims to complete the angular coverage of the STELLA experiment, especially between 60 and 90 degrees. For the angular distribution measurement, the detector BB10 has higher granularity. The strips of the detector cover different angles without accounting for the position on the strip. Figure 3.10 shows the kinematic energy of the alpha and proton channels with their excited states in black and red, respectively, in the two S3 detectors (S3F between 0.2 and 0.5 rad and S3B between 2.6 and 3 rad) and the PIXEL detector, the latter placed between 0.8 and 1.6 rad. It shows strong variation of the energy of the alpha particles from kinematics boost and energy loss in the protection foils (aluminum).

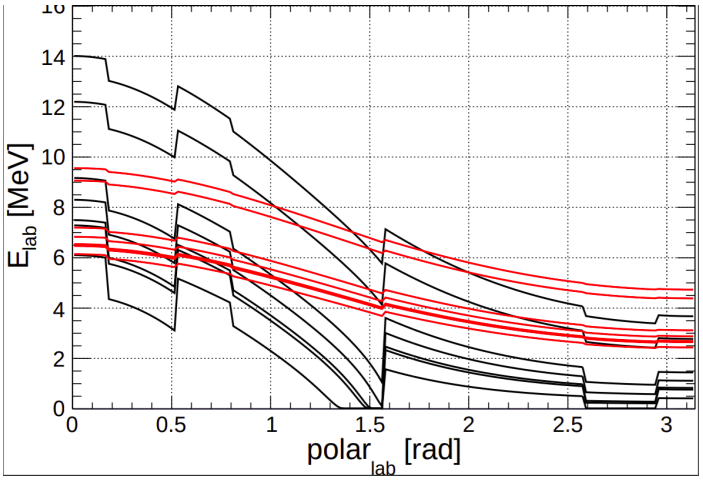


Figure 3.10: Energy kinematic calculations showing energy in the two S3 and the PIXEL detectors. The energy loss in the aluminum foils cause the dips at the angles covered by the detector.

The difference of the reaction kinematics and absorption characteristics in the detector cover reflect in the energy spectrum of PIXEL in Figure 3.11, where narrow and wide peaks appear. The former ones are protons, as their energy variation is limited even in a strip with wide angular coverage. The wider peaks can be identified as

alphas, with a strong angular dependency of the energy. However, using coincidences exit channels with gamma emission will be extracted even if the kinematic lines cross each others providing a wider picture of the angular distribution of the differential cross-section.

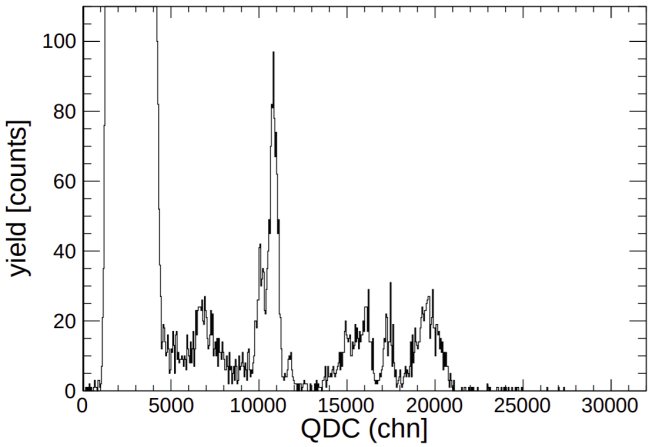


Figure 3.11: QDC spectrum from a strip of the BB10 detector from the PIXEL project.

### 3.1.3 Energy calibration

The measurement at low relative energy, because of expected very low statistic requires a very good understanding of the detector behaviour. For the particle detectors, two features are important, the calibration and the resolution. There are two ways of performing the calibration, using the exit channels associated with kinematic calculations at a known beam energy, or using a 3-alpha source. If the cross-section is large enough, the calibration using the exit channels provides data over a wide energy range, while the 3-alpha calibration is independent of the beam energy and its properties are very well known, but only cover energies from 5 to 6 MeV.

For most of the data analysis presented in this work, due to low statistic, the 3-alpha calibration has been used with excellent results. It is composed of $^{239}$Pu, $^{241}$Am and $^{244}$Cm, with the major decay energy of $E_\alpha^{\mathrm{Pu}} = 5156.59$ keV, $E_\alpha^{\mathrm{Am}} = 5485.56$ keV and $E_\alpha^{\mathrm{Cm}} = 5804.77$ keV. The raw spectra are fitted for each strip of the detectors and of the energy the major decay lines are associated. In the Figure 3.12, the energy of the alpha particles are shown in the $y$-axis and the mean value of the associated peak in QDC spectrum (QDC channels) in the $x$-axis. The graph is fitted with a linear function and the obtained parameters are used for the calibration (see box in Figure 3.12).

Once the data are calibrated, the measurement of the effective energy resolution of

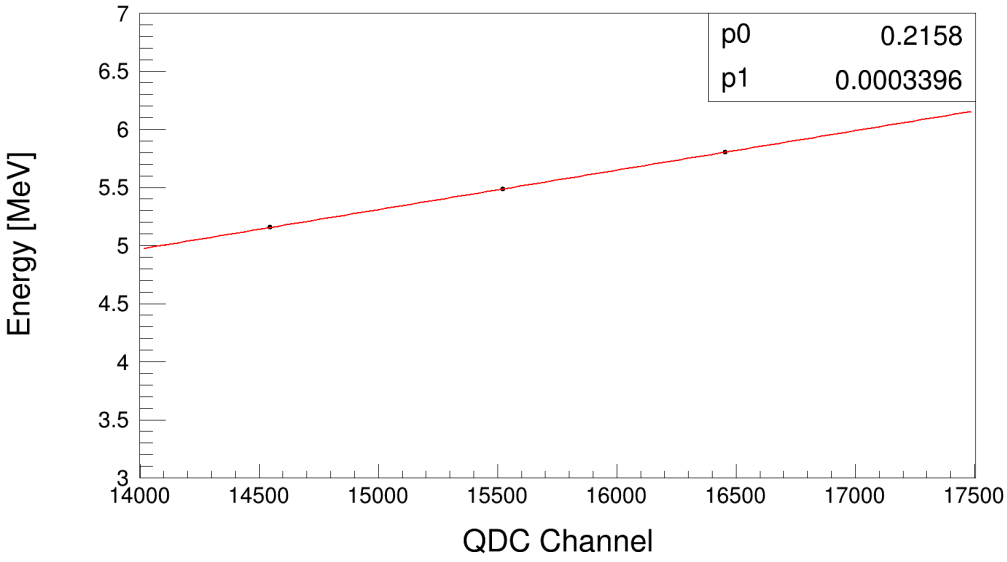


Figure 3.12: Calibration fit with nominal decay energies on the $y$-axis and mean value of the main peaks of the alpha sources for a typical strip of the S3F detector in QDC channels on the $x$-axis

the detector can be performed. In this work the resolution of the detector strongly depends on the thickness of the aluminum foils protecting them, because of the energy straggling of the particles. The resolution has been determined for each strip of the detectors. For the S3F detector, with 10 $\mu$m, the resolution has been measured using experimental data at a beam energy of $E_{\text{lab}} = 6.80$ MeV for the $\alpha_1$ exit channel. Figure 3.13 shows on the same plot the mean value of experimental data measured for the $\alpha_1$ exit channel (red bold cross) and for deuterium (blue bold cross) ground state contamination, as well as their associated kinematic calculation for all the strips of the S3F detector (red and blue circles). On both sides of the measurements, the thin cross indicates the resolution of the detector at a one sigma level of the fitted gaussian. Minor variations can be observed between measurements and theory but they never exceed the one sigma limit. At low energies, the energy of the $\alpha_1$ and $p_1$ particles are closer to the 3-alpha source energies, meaning that the calibration covers well the region of interest of this works measurements. The events on the charged particle detector at low energies are selected using the condition $E_{\text{gate}} = E_{\text{kin}} \pm 4 \times \sigma_{\text{res}}$, where $E_{\text{gate}}$ is the energy range for the selection, $E_{\text{kin}}$ is the calculated kinematic energy and $\sigma_{\text{res}}$ is the effective detector resolution. As 99.73% of the events of a gaussian are distributed in three sigmas around the mean value, with a maximum discrepancy of one sigma, energy selection within four sigma range keep the associated uncertainty far below 1%.

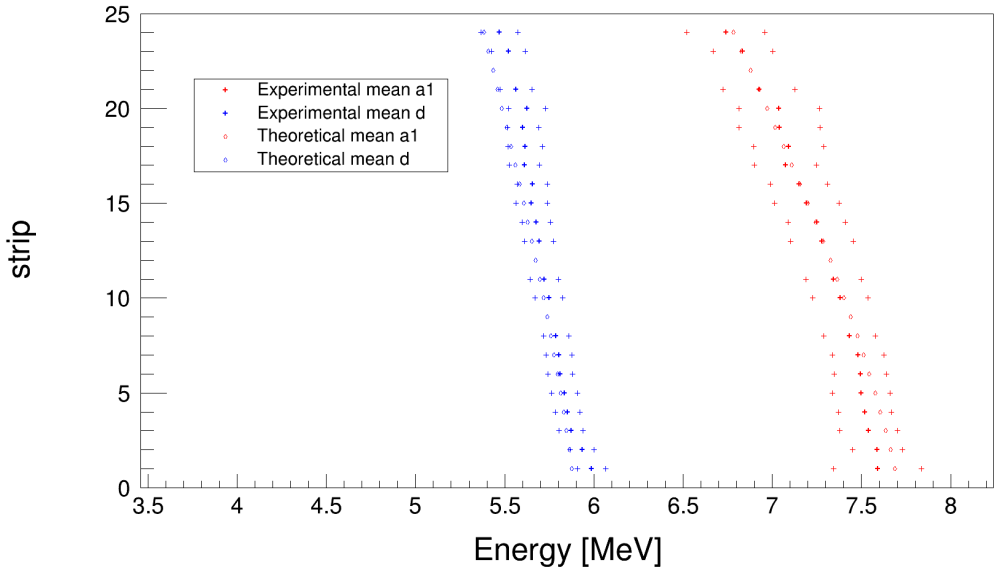


Figure 3.13: Comparison between the fitted experimental energy of the $\alpha_1$ (red bold cross), the deuterium (blue bold cross) ground state contamination, and their calculated kinematic energy (empty diamonds), as a function of the S3F detector strip. The thin crosses around the measured energy represent the one sigma resolution of the fitted gaussian.

## 3.2 Gamma detection

$LaBr_3(Ce)$ scintillator detectors from the UK-FATIMA collaboration [56] [57] are used to measure gamma de-excitation of states in the daughter nuclei. For the $\alpha$ and the proton channels of the $^{12}C + ^{12}C$ fusion reaction, these are excited states in $^{20}Ne$ and $^{23}Na$. The current analysis focuses on the first excited states of those two nuclei, that both decay to the ground-state through gamma-emission with energies of $E_\gamma^{^{20}Ne} = 1634$ keV and $E_\gamma^{^{23}Na} = 440$ keV. In this section, the analysis of the data obtained with the $LaBr_3(Ce)$ scintillator.

### 3.2.1 Self-activity of $LaBr_3(Ce)$

The $LaBr_3(Ce)$ crystal contains nuclei ($^{138}La$, $^{227}Ac$) that show radioactive decay. This contribution is well known, as can be seen in [58]. The latter ($^{227}Ac$) is in the crystals because it is chemically similar to the $^{138}La$. The $^{227}Ac$ its the daughter nuclei emit alpha particles of energies between $E = 1600$ keV and $E = 3000$ keV. $^{138}La$ decays at 66.4% by electron capture and 33.6% by beta decay to $^{138}Ba$ and $^{138}Ce$, respectively. In both cases the first excited state is populated and decays by a gamma transition,

with energies $E_\gamma = 1436$ keV and $E_\gamma = 789$ keV, respectively.

The identification of exit channels in the scintillators is, in this work, focused on the gamma decay from the two first excited states of $^{23}$Na and $^{20}$Ne, with energies $E_\gamma = 440$ keV and $E_\gamma = 1634$ keV respectively. The detection efficiencies for those contributions are 6% and 2% obtained from Geant4 simulations, respectively, as described in Section 2.3 [56] [57].

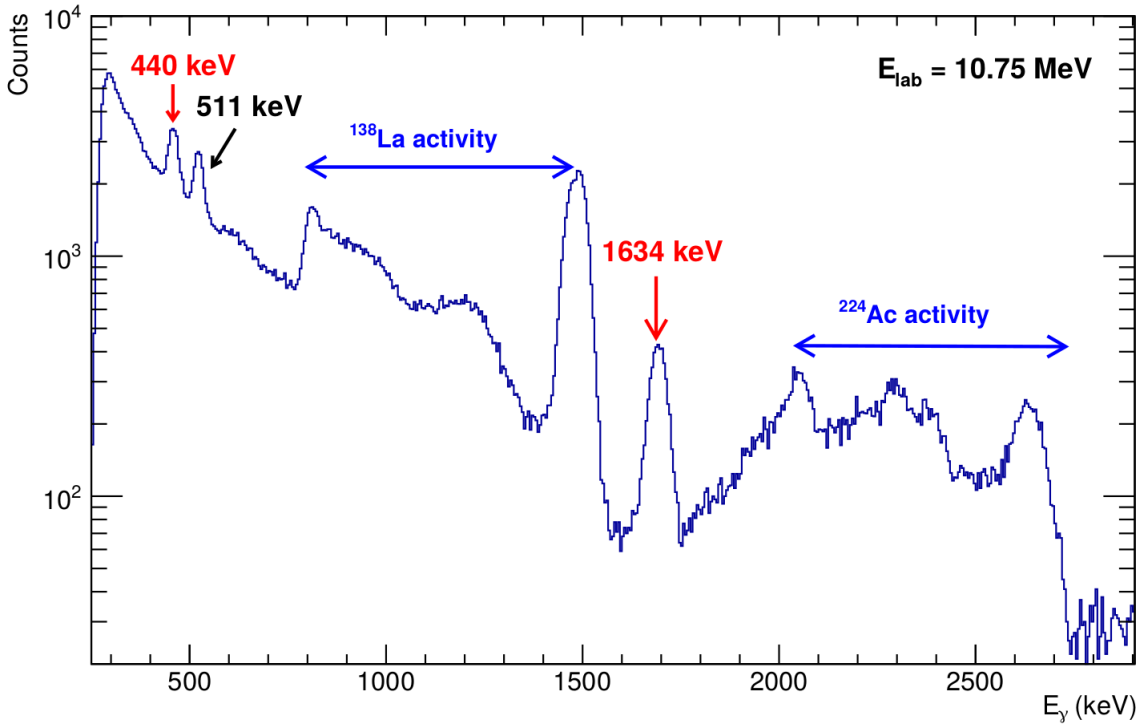


Figure 3.14: Gamma energy spectrum at a beam energy of $E_{\text{lab}} = 10.75$ MeV. The self activity from both $^{138}$La and $^{227}$Ac is shown with blue arrows, the decay of the first excited states of $^{23}$Na and $^{20}$Ne in red [40].

Figure 3.14 shows a typical gamma energy spectrum, at a beam energy of $E_{\text{lab}} = 10.75$ MeV, using data from the first campaign in 2016-2017 [37], where several contributions are observed. First, the self-activity above mentioned, is indicated with blue arrows, and dominates the spectrum between 700 keV and 1550 keV and between 2000 keV and 2800 keV from the decay of $^{138}$La and $^{227}$Ac respectively. The bulk towards higher energies of the peak at 789 keV comes from by electrons from the beta decay with an energy of $E_{beta} = 258$ keV end point. The peaks indicated by red arrows at 440 keV and 1634 keV are gamma decays from the first excited states of the $^{23}$Na and $^{20}$Ne, subject of this work. The contribution at 511 keV comes from pair creations from the ambient gammas.

### 3.2.2 Internal activity calibration

The internal activity of the $LaBr_3$ crystals allows an continueous energy calibration independent of conventionally external radioactive sources. The energy calibration of the scintillators is based on a Geant4 simulation of the $^{138}$La decay pattern [58] that is compared to experimental data to obtain the calibration parameters. The raw experimental data are fitted to the simulation leaving the QDC-bin a free parameter to perform an energy calibration. The simulation with the fit are shown in the Figure 3.16 and the results of the calibration is shown in the Figure 3.15 where the blue line represent the experimental data analysed in this work at a beam energy of $E_{\text{lab}} = 4.81$ MeV and the red spectrum corresponds to the simulation of the $^{138}$La decay.

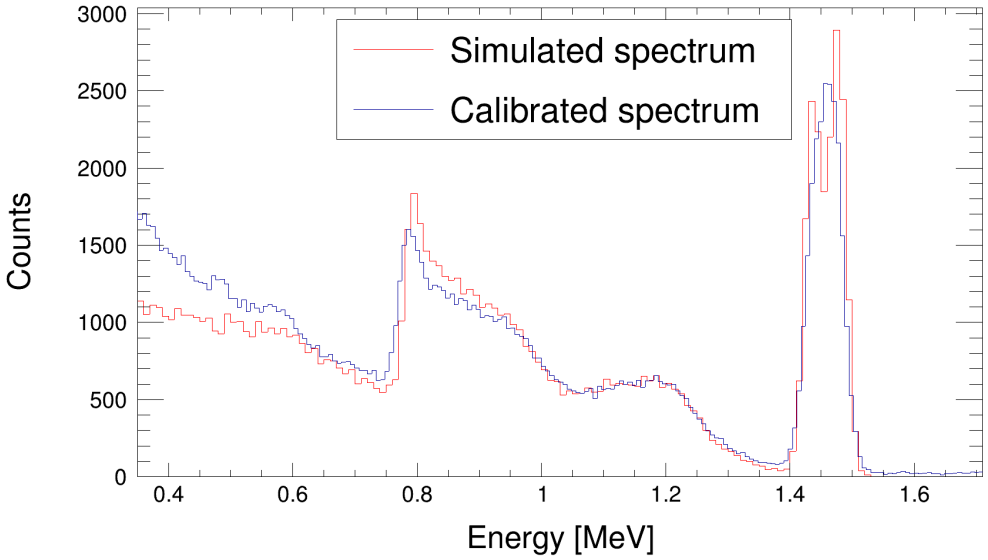


Figure 3.15: Energy calibrated gamma spectrum in blue of a $LaBr_3$ scintillator at $E_{\text{lab}} = 4.81$ MeV compared with the simulation in red.

The first step is to convolute the simulation with the average energy resolution. Then detect the 784 keV and 1436 keV peaks in QDC spectrum and approximately adjust the QDC-spectrum (Figure 3.15). The second step consists in using a fit function with the QDC-bin as a fit parameter to perform the linear calibration (Figure 3.16).

This calibration of the scintillators can be performed on an hour basis allowing stability check for very long measurement. The Figure 3.17 shows a temperature drift (blue squares) corrected with calibration samples of 45 min [8].

The blue squares are non-corrected data of the 1434 keV peak. The peak energy follows night and day cycles, in other words evolution of the temperature with respect to the time that impacts the gain of the photomultiplier. With a calibration every

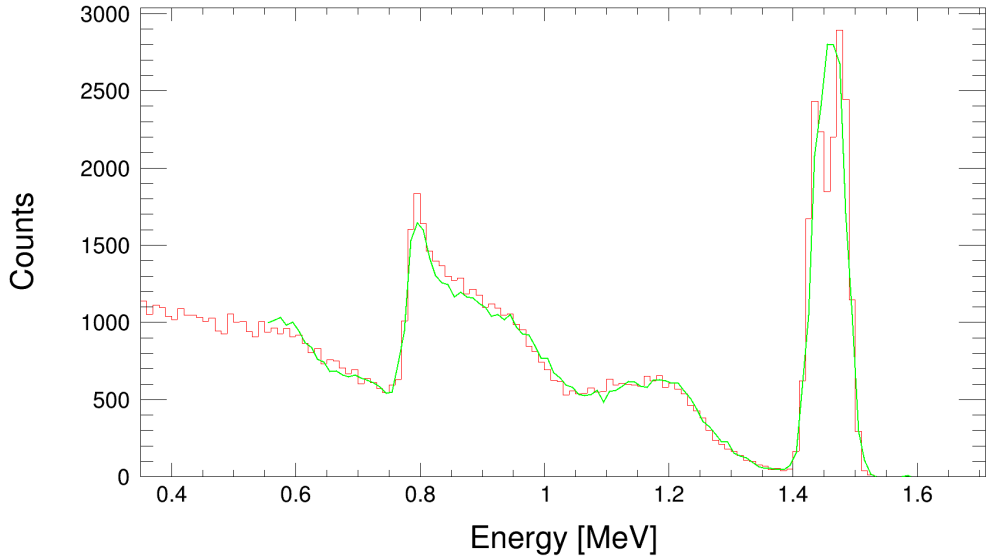


Figure 3.16: Simulation of the $^{138}$La decay in red fitted to calibrate the Data, green curve.

45 min, the reconstructed energy of the same contribution stays stable, as demonstrated by the red triangles. For the data presented in this work using self-calibration, the energy variation of the peaks of interest ($E_\gamma = 440$ keV and $E_\gamma = 1634$ keV), over two months of data taking was negligible.

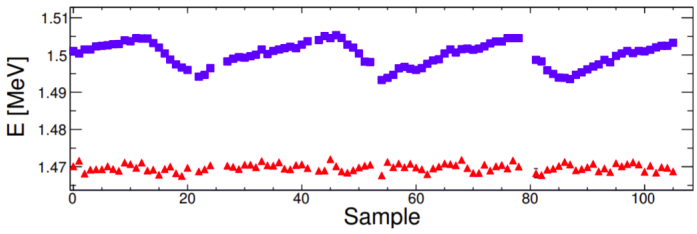


Figure 3.17: Evolution of the energy with respect to time for a data samplings of around 45 min. The red triangles data points are self-calibrated for each sample periods while the blue squares are not [8].

### 3.2.3 Gamma energy selection

In the frame of this work, gamma measurement for the $^{12}$C + $^{12}$C fusion reaction focuses on the first excited stated of the $^{23}$Na and $^{20}$Ne, with a respective energy of $E_\gamma = 440$ keV and $E_\gamma = 1634$ keV. Figure 3.18 shows a gamma energy spectrum, it is the sum of all the detectors from the UK-FATIMA array, including 35 detectors, at a

beam energy of $E_{\text{lab}} = 7.64$ MeV, with a downscaling of 10000 on the non-coincident events. Downscaling is used to limit the file size to practical numbers, and the result is the suppression of potentially uninteresting events.

This means that for gammas that are not measured coincidently with a charged particle in a S3 detector, only $\frac{1}{10000}$ are written in the analysed data file. The resulting spectrum is mostly composed of coincident events, but still shows features of the self activity, above 1.8 MeV for the alpha decay from $^{227}$Ac and between 700 keV and 1550 keV for the decay of the $^{138}$La. The peak around 1.6 MeV comes from two contributions, the decay of the first excited state of the $^{20}$Ne at $E_\gamma^{^{20}\text{Ne}} = 1634$ keV and from the second excited state of the $^{23}$Na decaying through the first one at $E_\gamma^{^{23}\text{Na}} = 440$ keV. Due to lack of statistic, the peak at $E_\gamma = 440$ keV cannot be identified in the background.

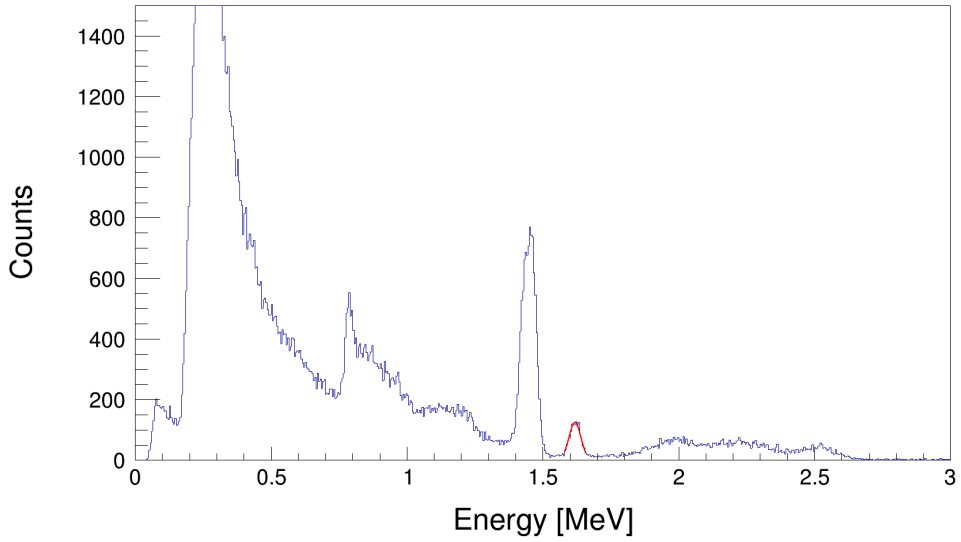


Figure 3.18: Gamma sum-energy spectrum of all 35 scintillators used during the experiment, at $E_{\text{lab}} = 7.64$ MeV, with a downscaling of the non-coincident events of 10000. No specific particle energy was selected.

The gamma energy gates for $\alpha_1$ and $p_1$ transitions were defined using gamma spectra with coincident selection of associated particle energy in S3F (see Section 3.1.3). Figure 3.19 shows the gamma spectrum for the full scintillator array with an energy gate on $\alpha_1$ particles. The full-energy peak can be clearly identified and the spectrum also shows the Compton background. The peak is fitted with a gaussian and the energy gate is determined based on it.

The same method is applied to determine the energy gate for the gamma associated to the $p_1$ exit channel. The result is shown in Figure 3.20 where the associated $\gamma$-

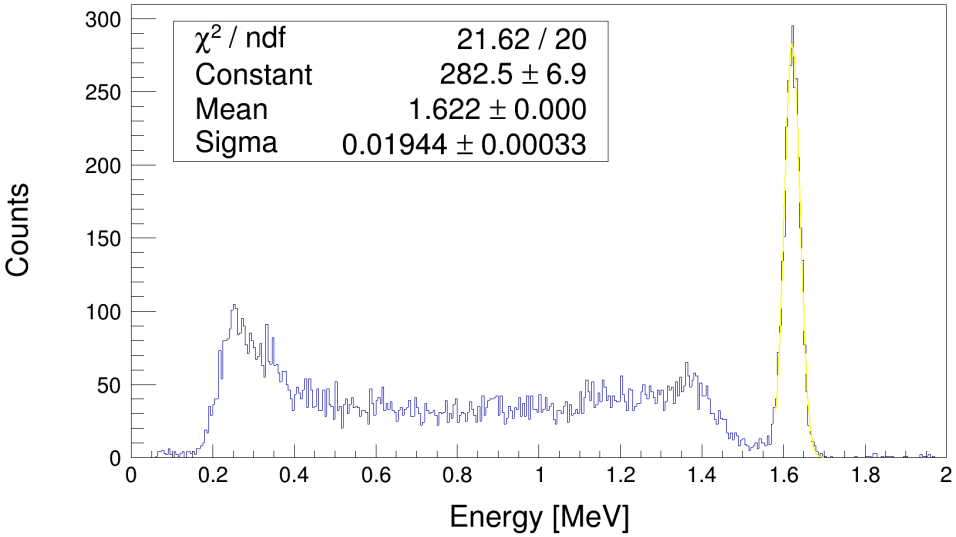


Figure 3.19: Gamma sum-energy spectrum of all 35 scintillators used during the experiment, at $E_{\mathrm{lab}} = 7.64$ MeV, with a three sigma energy selection of the $\alpha_1$ transition in S3F.

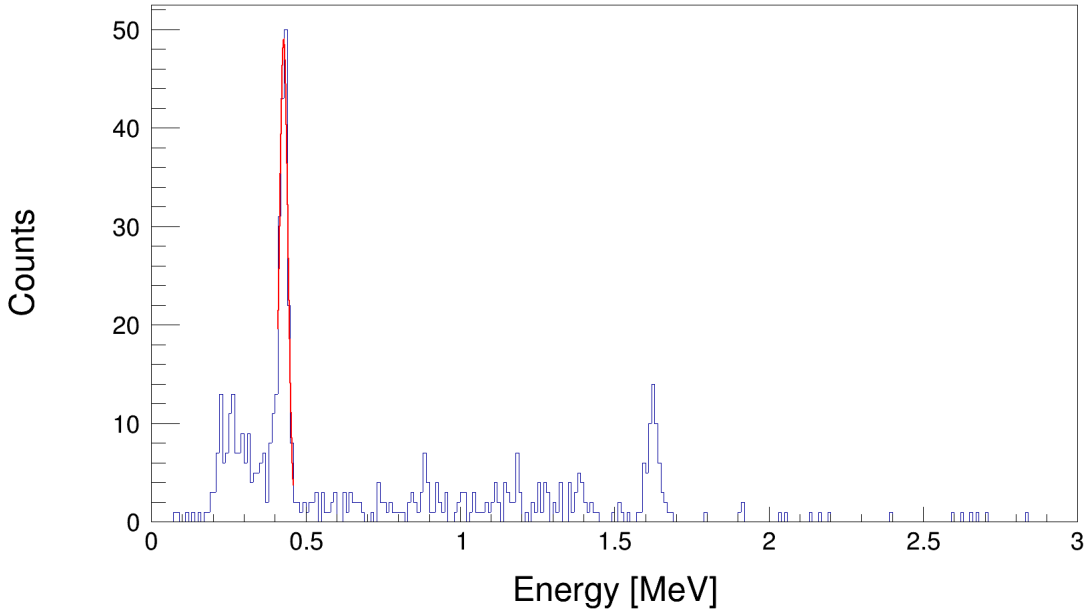


Figure 3.20: Gamma sum-energy spectrum of all 35 scintillators used during the experiment, at $E_{\mathrm{lab}} = 7.64$ MeV, with a three sigma energy selection of the $p_1$ transition in S3F.

transition is now clearly distinguishable at $E_\gamma = 440$ keV (compare Figure 3.18). It can be fitted and the energy gate parameters can be extracted. The full energy peak at

$E_\gamma = 1634$ keV still appears with its Compton plateau, because in the energy selection on the particle detector, within the three sigma from the resolution of the detectors, some protons and alphas signals overlap on several strips.

The parameters used to determine the gates for the gamma energy selection are shown in the Table 3.1.

Table 3.1: Gates for the gamma energy selection

| | $\hat{x}_{gateE_\gamma}$ [MeV] | $\sigma_{gateE_\gamma}$ [MeV] |
|---|---|---|
| Proton channel | $0.4311 \pm 0.0008$ | $0.01365 \pm 0.00082$ |
| Alpha channel | $1.622 \pm 0.001$ | $0.0194 \pm 0.00033$ |

## 3.3 Coincidences analysis

The coincidence analysis focuses on gamma and charge particles recorded withing a 400 ns interval. Figure 3.21.a shows particle energy *versus* the time difference between gamma and charged particle. In Figure 3.21.b, gates on the gamma energy for the $E_\gamma = 440$ keV and $E_\gamma = 1634$ keV for proton and alpha channels respectively, are applied. Blobs can be observed in both Figures, they correspond to correlated events. On the left side, events out of those blobs can be observed and are non-correlated events, all over the spectrum. This is demonstrated on the right side, where most of it has disappeared after a gamma energy selection. The boxes, black for $\alpha_1$ and red for $p_1$, are the region of interest of the signal and the background boxes are dashed, evaluating it out of the correlation timing. Thus, it is evident that the optimization of this timing is essential for an accurate selection of fusion events.

On the left Figure 3.21, the blobs are labeled $p_1$, $p_2$, $\alpha_1$ etc... to indicate the exit channels, and a red phenomenological line splits the protons channels from the alpha channels. It shows that even when two correlated particles types have the same energy in the particle detector, they can be separated with the timing selection ($\alpha_1$ and $p_6$ on the Figure 3.21). The timing difference between the two exit channels, comes from the interaction of the particles with the detector, as discussed in Chapter 2.

To optimise the timing precision, a correction was implemented using next neighbour alignment of the timing of the different strips of the particle detector (S3F and S3B). Two methods have been tested. The first one is based on multiplicity-two events between the neighboring strips and measures the timing difference between them. Charge sharing events are expected to generate simultaneous signals on the

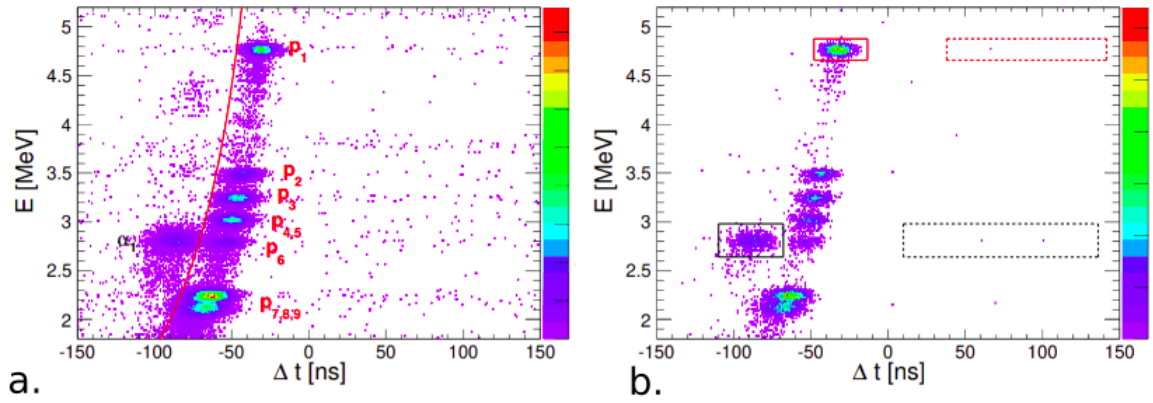


Figure 3.21: Particle energy versus time spectra in the S3B detector at a beam energy of $E_{\text{lab}} = 10.75$ MeV, data from the first experimental campaign [37], on the left side are shown coincidences with every gamma and on the right side with selected gamma for the $E_\gamma = 440$ keV and $E_\gamma = 1634$ keV for proton and alpha channels respectively. [8]

involved strips, at variance with uncorrelated events triggering two strips, whose time difference distribution will be flat. The mean value of the gaussian gives the time difference between the two strips. Doing so for all the strips allows to realign the timing of all strips of the detector. Figure 3.22 shows the time differences between the two signals of charge-sharing events in neighboring strips. For the couple of strips shown here the timing difference is 3 ns ($p1$ parameter), that have to be sum up to the time difference of the previous pair of strips (in geometrical order) to achieve a full time alignment. With this method, the time resolution precision reached is $\sigma_t =$ 10 to 15 ns.

The second method employs directly the time differences between gamma and charged particles. Following the same principle as the multiplicity-two method restricted to particles only, time correlated signals happen in the 400 ns interval for coincidences determination, whereas non-coincident ones show a random time difference distribution. A selection is made with the alpha particles from the $\alpha_1$ exit channel with four sigma energy selection around kinematic energy computed at the strip angle and a three sigma selection on the gamma energy $E_\gamma = 1634$ keV. The correlated events peak can be fitted with a gaussian. Its mean value is the timing correction associated to the strip. To realign the timing for the entire detector, each strip is corrected independently with the determined offset.

The efficiency of the method is illustrated by Figure 3.23 and 3.24. The raw time difference is shown in the Figure 3.23, with the selection on $\alpha_1$ particles discussed in

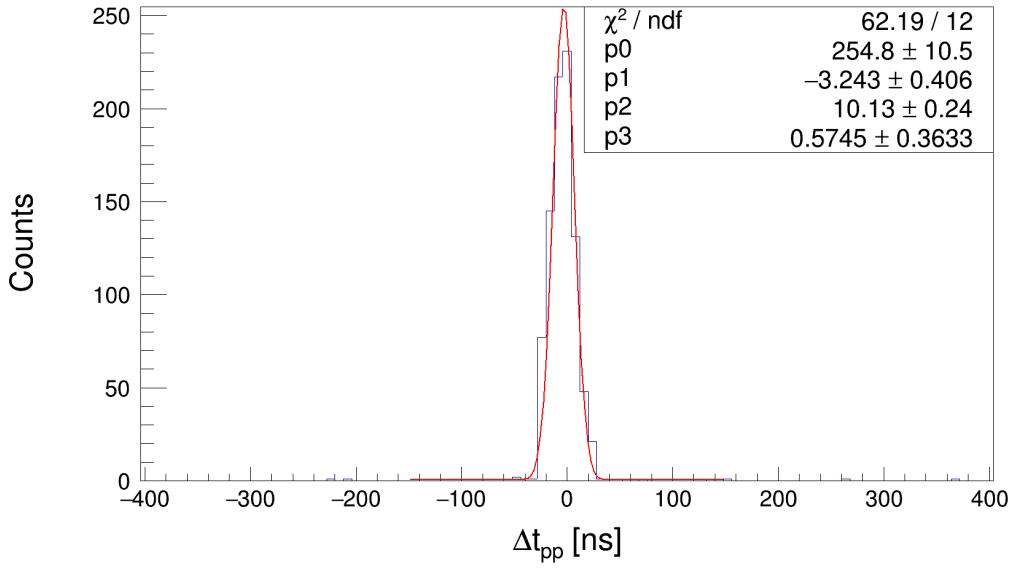


Figure 3.22: Time difference spectrum of multiplicity-two events in two neighboring strips.

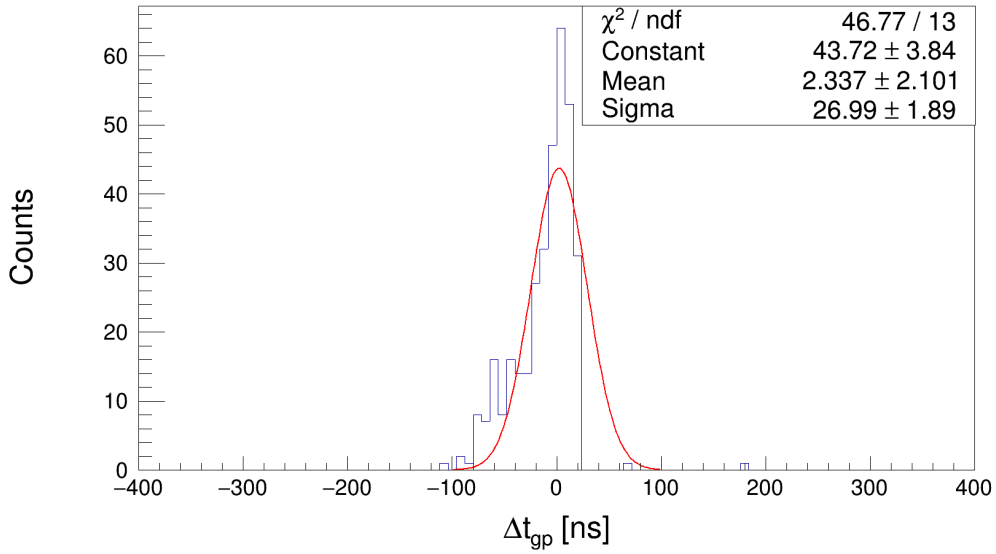


Figure 3.23: Time difference spectrum between gammas and $\alpha_1$ particles without any correction (tail) at a beam energy of $E_{\text{lab}} = 6.80$ MeV.

the previous paragraph, without time correction. A distribution centered at zero can be observed with a tail towards negative values in the spectrum. This means that some strips are a bit shifted in time than others. The same spectrum with time offset can be observed in Figure 3.24. The tail has been corrected and a regular gaussian centered on $\Delta t = 1.77 \pm 0.58$ ns with $\sigma_t = 10.27 \pm 0.49$ ns.

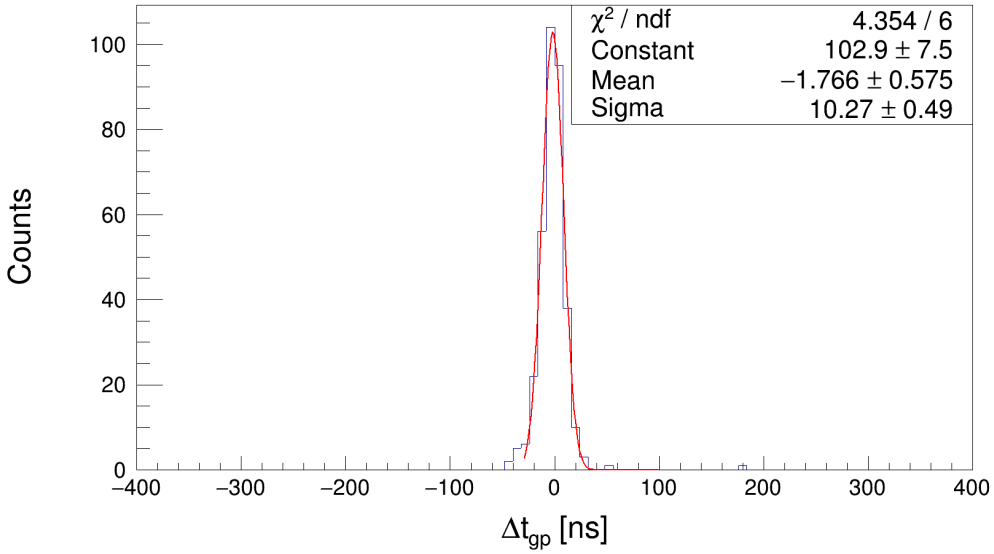


Figure 3.24: Time difference spectrum between gammas and $\alpha_1$ particles with the gamma-particle correction method at a beam energy of $E_{\text{lab}} = 6.80$ MeV.

Both method give similar results, the precision reached is slightly better with the gamma-particle method. This can be explained by several reasons. First, the timing is strongly linked to the clock of the DAQ and the type of detector used. The first one relies on the comparison between two signals sampled at 125 MHz of two semiconductors detectors (two strips of S3 detector), where response is dominated by the charge migration in the substrate. On the other hand for the gamma-particle method combine a 125 MHz and 1 GHz DAQ, between a semiconductor and a scintillator (the $LaBr_3$ (Ce) have sub-nanosecond timing). The second reason for high precision gamma-particle timing is that the first method corrects the timing difference with respect to previous couples of strips in a chain along the detector, with accumulating uncertainties of all the timing measurements. The second method is independent for all the strips.

For the protons, the applied selection with the particle energy is at four sigmas around the nominal $p_1$ kinematic energy, and a gamma energy selection at $E_\gamma = 440$ keV with a three sigma acceptance. In Figure 3.25, the raw time difference between gamma and charged particles are shown with a selection on $p_1$. Two structures can be identified, a gaussian centered on $\Delta t = 52.59 \pm 1.54$ ns with $\sigma_t = 8.36 \pm 1.16$ ns, corresponding to the $p_1$ contribution, and a wide structure to the left of the gaussian. Those events correspond to a contamination from $\alpha_1$ particles in coincidence with a Compton event in the 440 keV energy selection range. Applying the gamma-particle

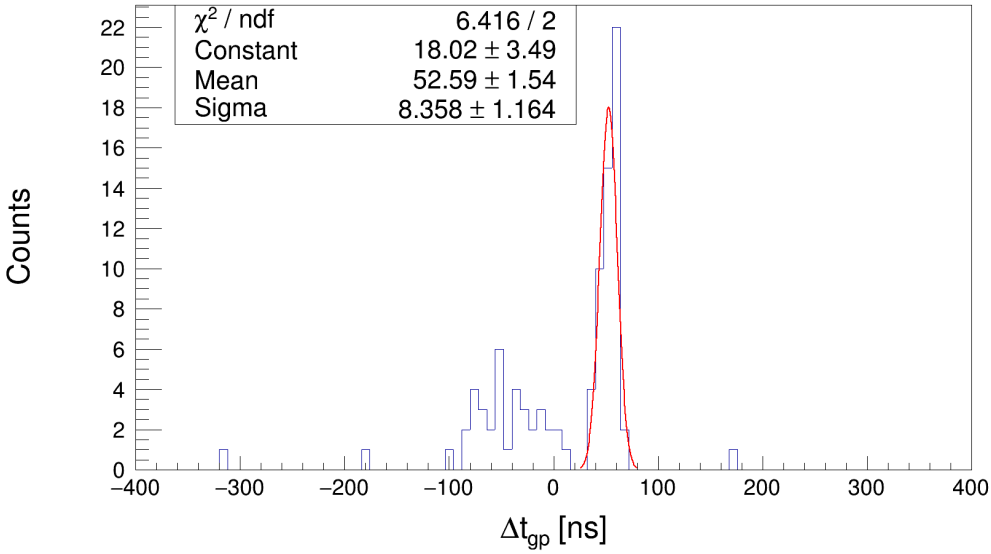


Figure 3.25: Time difference spectrum between gammas and $p_1$ particles without any correction at a beam energy of $E_{\text{lab}} = 6.80$ MeV.

method to the proton does not improve the timing resolution. The explanation can be found in the way particles interact within the silicon detector. Notably, alphas are believed to deposit their energy in a zone that is widely spread out. The timing then depends on the trigger generated by the electron avalanche from such a wide charge distribution. Protons on the other hand, create electron charges predominantly along the initial track of incident angle into the substrate. The very uniform location of the Bragg peak then creates more precise timing information as compared to alphas.

To control the validity of the timing gate parameters, the measurement of the gate parameters can be compared at different beam energies, in order to investigate any energy dependent effect on the timing. Energy deposition in the detector (Bragg peak) could impact the timing, and could explain the difference between protons and alpha particles. As the alphas go less deep inside the detector, and are more sensitive to energy loss in the materials. Decreasing the energy could impact the time difference measured.

Figure 3.26 shows the timing gate analysis as a function of the relative energy. The selection gates are represented by the mean value and one sigma uncertainty interval, for the proton and alphas in red and black, respectively.

The analysis was performed under stable conditions, meaning same detectors and same voltage to deplete the detector, and requires sufficient statistic to extract a timing gate. The first of all, in this Figure, the protons shows the same behaviour as the alphas but with a weakened effect. Second, no systematic behaviour with respect

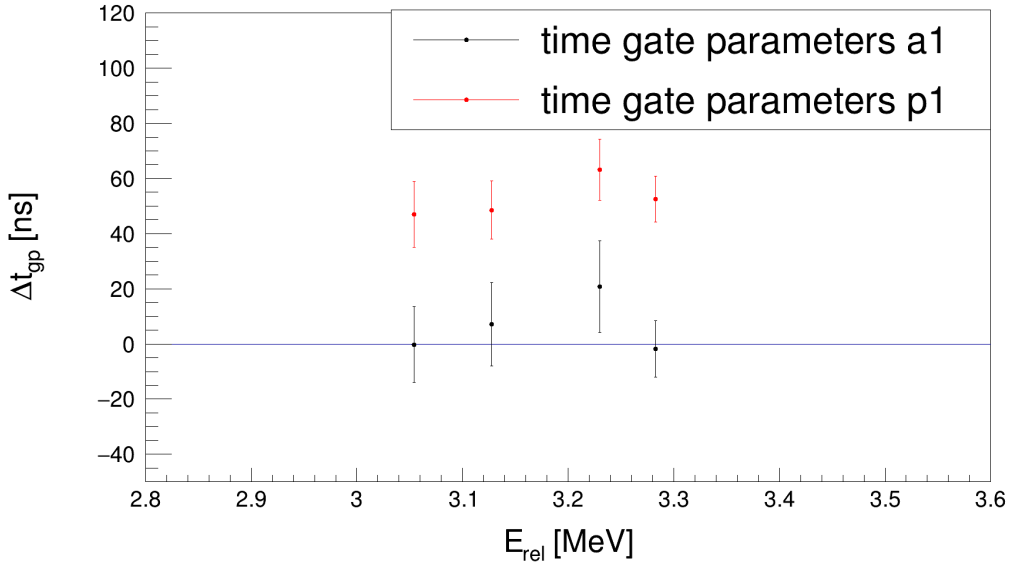


Figure 3.26: Measured timing gates parameters *versus* the interaction energy in the center of mass system. The red and black dots represents protons and alphas mean values, respectively, and the error bars represent the one sigma range of the measured gate parameter.

to the energy is observed. But with only four energies investigated, no conclusion can be made. Thus, regarding this result, the timing gate measured on the higher beam energies is taken with a five sigmas acceptance for the analysis of the lowest data measurement at $E_{\mathrm{rel}} = 2.32$ MeV.

To summarize, three analysis have been discussed. The charged particles' detection is introduced, discussing the identification of the particles and how to reconstruct the energy, allowing consistent angular distribution measurement as well as low statistic measurement with an energy selection considering the calibration and kinematic calculations. Then the analysis of the scintillators has been discussed, in particular the stability of the energy calibration, using the self activity and leading to a precise determination of the gamma energy selection rules. And to finish, the time differences between the gamma measurement and the charged particles in coincidence is described, showing the strength of this selections to separate protons from alphas particles event at the same energy in the particle detector. The time alignment of the strips of the silicon detectors shows an effect on the alpha but not on the protons. It demonstrates that the interaction of the particles with the detector affects the timing evaluation. However, the study of this effect with different beam energies do not show a systematic behaviour, but another effect might affect the timing measurement and has to be taken into account for low energy measurement, with the determination of

the timing selection rules (timing gates).

## 3.4 Résumé chapitre 3

L'analyse de données associée à cette expérience regroupe des informations sur l'énergie des particules chargées et des gammas de désexcitation des noyaux fils, couplées à une information temporelle. Les détecteurs de particules chargées, situés dans la chambre, permettent également de déterminer l'angle de détection des particules chargées. Dans un premier temps, pour remplir les spectres, nous avons dissocié les évènements générant des signaux dans une seule piste, qui reproduisent exactement l'énergie des particules mesurées, des évènements générant des signaux dans deux pistes (multiplicité deux), dont l'énergie doit être reconstruite. Parmi ces évènements de multiplicité deux, on peut en identifier deux types : ceux qui représentent un partage de charge (Figure 3.3), autrement dit deux signaux dans deux pistes différentes provenant d'une unique particule, et ceux pour deux particules en simultanés arrivant dans le détecteur générant un signal dans deux pistes dans un intervalle de 400 ns. Dans le premier cas, l'énergie des deux signaux doit être additionnée pour recontruire l'énergie de la particule mesurée. Dans l'autre cas, les deux signaux doivent être traités indépendamment.

Pour les différencier, on peut considérer que les évènements de partage de charge arrivent uniquement dans des pistes voisines, alors que dans l'autre cas les pistes touchées sont aléatoires. Une première sélection sur le voisinage corrige la majorité des évènements. Il a été observé que les évènements mesurant deux particules distinctes viennent principalement de la diffusion élastique avec des noyaux d'hydrogènes présents dans l'eau contenue dans la cible. Une correction supplémentaire peut être faite analysant la corrélation en énergie entre les deux signaux mesurés. Deux particules distinctes arrivent à une énergie fixe dans le détecteur, alors que pour un partage de charge partage, l'énergie est aléatoirement répartie entre l'énergie de la particule et zéro (Figure 3.6). Nous avons démontré que cette contribution restante est négligeable.

La géométrie des détecteurs permet de mesurer des distributions angulaires, comme montré dans la Figure 3.9, et de les ajuster avec un polynome de Legendre, où l'ordre du polynome détermine le moment angulaire emporté par la particule mesurée. Cependant, on observe un manque de couverture angulaire empêchant de déterminer de façon définitive les contributions des ordres inférieurs du polynome de Legendre. Ceci est compensé par l'ajout en 2022 du détecteur PIXEL, décrit techniquement au chapitre précédent qui couvrira les angles entre 45° et 90°.

L'étalonnage peut être réalisé utilisant les lignes cinématiques et tenant en compte la perte d'énergie des particules dans les feuilles d'aluminium protégeant les détecteurs, ou en utilisant une source triple-$\alpha$. La stabilité de l'étalonage a été étudiée et la

décision de prendre une sélection d'énergie des particules de quatre sigmas autour de la ligne cinématique a été prise, basée sur les résultats de ces observations (Figure 3.13). La valeur de sigma est déterminée pour chaque piste indépendament en faisant un ajustement gaussien sur le pic $\alpha_1$ pour le canal alpha. Le pic correspondant aux protons venant de la réaction parasite avec le deutérium de l'eau contaminant la cible a été utilisé pour la déterminer résolution des protons, les voies protons $p_0$ et $p_1$ n'ayant pas suffisament de statistique pour le déterminer et la réaction contaminante étant proche en énergie des signaux protons issus de la fusion.

Du côté des scintillateurs, l'étalonage est réalisée à l'aide des pics de la radioactivité interne des détecteurs, et les spectres expérimentaux sont comparés à des simulations, notamment au niveau des pics correspondants aux décroissances du $^{138}$Ba et $^{138}$Ce à $E_\gamma = 1436$ keV et $E_\gamma = 789$ keV, respectivement. La simulation est ajustée aux spectres expérimentaux pour obtenir les paramètres de étalonage. Cette methode utilisant la radioactivité interne permet un étalonage quasi continu des scintillateurs et ainsi de corriger d'éventuelles variations de gain des photomultiplicateurs, permettant une mesure très stable dans le temps. De ce fait, l'intervalle en énergie pour la sélection des évènements sera fixé à trois sigmas autour des valeur moyenne des pics d'intérêt, $E_\gamma = 440$ keV et $E_\gamma = 1634$ keV pour les premiers états excités des noyaux $^{23}$Na et $^{20}$Ne, respectivement. Ces derniers ont été déterminés précisément dans les spectres expérimentaux à $E_{\text{rel}} = 3.755$ MeV, en faisant une sélection en énergie sur l'énergie des particules chargées coïncidentes ($p_1$ et $\alpha_1$) pour éviter une contamination du bruit de fond et évaluer au mieux les pics d'intérêt.

La dernière sélection concerne l'information temporelle. Pour ce faire il a dans un premier temps fallu réaligner temporellement les différentes pistes des détecteurs de particules chargées. Pour ce faire, deux méthodes ont été utilisées. La première utilise les signaux de partage de charge pour mesurer les différences temporelles entre pistes voisines et ainsi une correction par chaine de voisins pour réaligner temporellement tout le détecteur. Lorsque la statistique le permet, la seconde méthode utilise directement la différence temporelle entre les gammas de la désexcitation des noyaux fils et les particules chargées évaporées en sélectionnant les particules issues de la fusion avec les fenêtres en énergie des différents détecteurs. Cette dernière a l'avantage d'aligner temporellement les pistes indépendamment. Les précisions atteintes sont meilleures que pour la première méthode.

L'alignement a été effectué uniquement pour les alphas, les protons n'étant que très peu affectés. Cela indique que les différences temporelles entre les pistes sont liées à l'interaction de la particule avec le détecteur. Plusieurs énergies ont donc été analysées, regardant l'évolution des paramètres de sélection en fonction de l'énergie (Figure 3.26), s'attendant à observer une évolution systématique de la valeur moyenne du pic en

fonction de l'énergie, et ce avec une variation plus importante pour les alphas que pour les protons. Les résultats montrent des variations de la valeur moyenne pouvant aller jusqu'à un sigma et une augmentation de la valeur de sigma pour certaines énergies, sans tendance systématique. C'est pourquoi nous avons fixé la sélection à trois sigmas pour les énergies permettant de déterminer une fenêtre, et cinq sigmas pour l'énergie la plus basse ($E_{\mathrm{rel}} = 2.320$ MeV).

# Chapter 4

# Results and discussion

In this chapter will be discussed the event selection with the gates defined in Chapter 3. The energies investigated start with a consistency check at $E_{\mathrm{rel}} = 3.755$ MeV, then measurements around a resonant structure at $E_{\mathrm{rel}} = 3.2$ MeV and a last measurement at low energy $E_{\mathrm{rel}} = 2.230$ MeV, at the tail of a resonance structure at $E_{\mathrm{rel}} = 2.14$ MeV. The resulting S-factors will be discussed with the impact on astrophysics.

## 4.1 Event selection and cross-section measurement

The measurement of cross-sections starts with the evaluation of the background sources and how they impact the selection of events. The energy selection gates will be discussed for the scintillators and the particle detectors. The timing gates are computed run by run at high beam energies with rich statistics. The observations will be adapted to set the timing selection for the measurement at the lowest relative energy ($E_{\mathrm{rel}} = 2.320$ MeV). Then the background suppression with the gates will be described, and the cross-sections will be computed considering the background subtraction.

### 4.1.1 Energy selection gates and background

The stability of the gamma detectors calibration has been discussed in Section 3.2.2 and the gate width parameters have been investigated in Section 3.2.3. Considering the stability of the calibration, the use of a three sigma range of the energy distribution around the mean value of the peak of interest (3.1) has been taken for the gamma energy selection. Within three sigmas of a gaussian, 99.72% of the measured events are considered. If the calibration is stable, the mean value of the peak does not change. Thus, increasing the interval will not increase fusion event statistics, but the background in the spectra, in particular for the proton channel, where the gamma

decay at $E_\gamma = 440$ keV is subject to contamination from the Compton background from the self activity in the $LaBr_3$(Ce) crystals.

For the charged particle detector, a variety of effects can be observed impacting the resolution of the detector. The calibration is discussed in Section 3.1.3. However, the resolution of the detector also depends on the focusing of the beam and the thickness of the target. For these reasons, a four sigma range selection for the particle energy has been done, with a mean value of the gate determined by kinematic calculations (Chapter 3),

$$E_{\text{kin}}^{\text{lab}} = \frac{A_1 A_3 E_i}{A_2 \left(A_1 + A_2\right)} \frac{\left[\gamma_3 \cos\theta_3 \pm \left(1 - \gamma_3^2 \sin^2\theta_3\right)^{1/2}\right]^2}{\gamma_3^2}, \tag{4.1}$$

with $A_i$ the number of nucleons in the nuclei involved in the reaction, $E_i$ the center of mass energy, and $\theta_3$ the laboratory angle. $\gamma_3 = \left(\frac{A_1 A_3}{A_2 A_4} \frac{E_i}{E_i + Q}\right)^{1/2}$ where $Q$ is the $Q$-value of the reaction.

The resolution is measured at $E_{\text{cm}} = 3.755$ MeV using $\alpha_1$ and the proton from the contaminant reaction $^{12}\text{C} + d$, fitted with a gaussian. The contamination is well understood (see Figure 4.1) and serves as a reliable source of extracting these detectors caracteristics. At this energy, the proton cross-section is in some strips too low to be extracted without coincidence with sufficient statistic. Thus, a resolution is extracted for each strip of the detector from background to achieve the best evaluation of the spectra for the S3F detector.

Figure 4.1 shows energy spectra of all strips of the S3F detector with their associated angular coverage. The red, black and blue lines represent the calculated kinematic energy of the protons channels $p_i$, alpha channels $\alpha_i$ and the proton from the deuterium contaminant $d_i$, respectively. The $\alpha_1$ contribution between 7.5 and 9 MeV is clearly visible in the spectrum and the peaks are easily fitted. The proton lines ($p_0$ and $p_1$ in particular) are, however, quite weak and the measurement of the resolution would be subject to important uncertainties. On the other hand, protons from the reaction with a deuterium contaminant in the target is apparent at this energy. As both signals in the detector substrate are caused by protons and their energy are close to each others ($\approx 7$ MeV for $p_1$ and $\approx 6$ MeV for $d_0$), the resolution of the proton peak from the ground state of the deuterium reaction is a very good approximation of the resolution of the $p_1$ peak.

Figure 4.2 also shows a contribution between the $\alpha_0$ and $\alpha_1$ peaks, that cannot be explained with the described fusion mecanisms. It has a resolution wider than the alpha peaks and indicates that it might be a particle heavier than an alpha particle or two particles detected in the same strip at the same time.

An approach to identify it is investigating potential beam contamination with nuclei

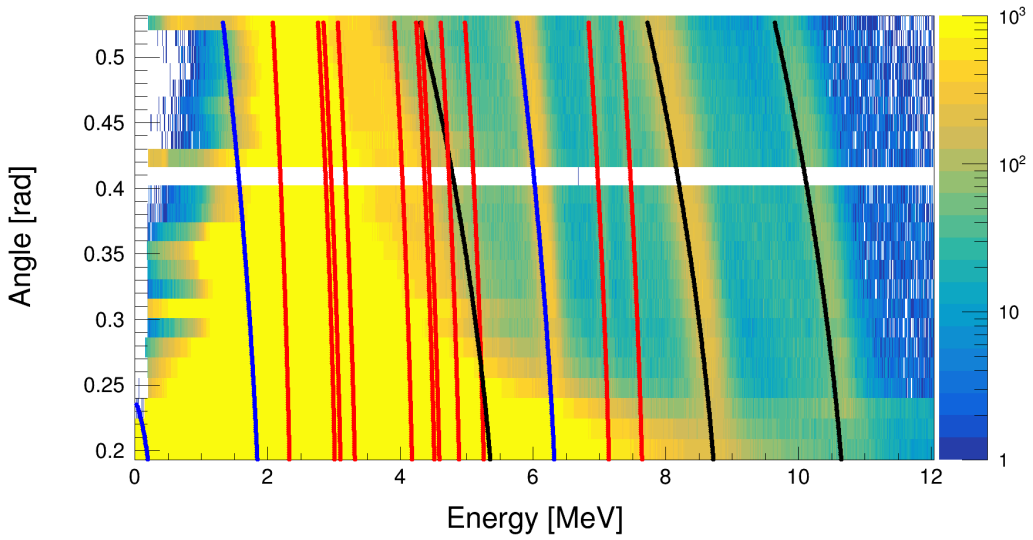


Figure 4.1: Angle in the laboratory frame *versus* the energy. The 24 strips of the S3F detector are presented with their associated angular coverage. The measurement is performed at $E_{\mathrm{rel}} = 3.755$ MeV. The red, black and blue lines represent the calculated kinematic energy of the protons channels $p_i$, alpha channels $\alpha_i$ and the protons from the deuterium contaminant $d_i$, respectively.

compatible with selection in the 90° magnet ($A/C$ similar with $C$ the charge state) in the Andromede beam line. For the data analysed in this work, a charge state of $2^+$ has been used. All promising candidates were excluded, because they require different charge states which is not compatible with the observation in Figure 4.2 at $E_{\mathrm{rel}} = 3.37$ MeV. The position of the contribution stays between the $\alpha_0$ and $\alpha_1$ peaks. It means that with a higher charge state, the energy of the contribution should scale differently than the $\alpha_0$ and $\alpha_1$ energies. This triggers the idea of the simultaneous detection of an $\alpha_1$ plus a proton from the elastic scattering $p_{\mathrm{el}}$ of a $^{12}$C on a $^1$H from water contaminating the target (associated kinematic calculation in dark green in the Figure). The energy seems to match, however decreasing the beam energy lower the $\alpha_1$ cross-section, while the contribution becomes stronger. Some events in this peaks might be $\alpha_1 + p_{\mathrm{el}}$, but as discussed in Section 3.1 this contribution should be negligible An analysis in coincidences with a gamma line has been made with a particle energy selection, but no gamma contribution has been observed different than a very small $E_\gamma = 1634$ keV peak, that comes from $\alpha_1$ events. Another argument against this hypothesis is that if is was a simultaneous measurement of two particles, other lines should be observed, $\alpha_0 + {}^1$H and $d_0 + {}^1$H.

In the S3F detector, there are two main sources of background in the relevant

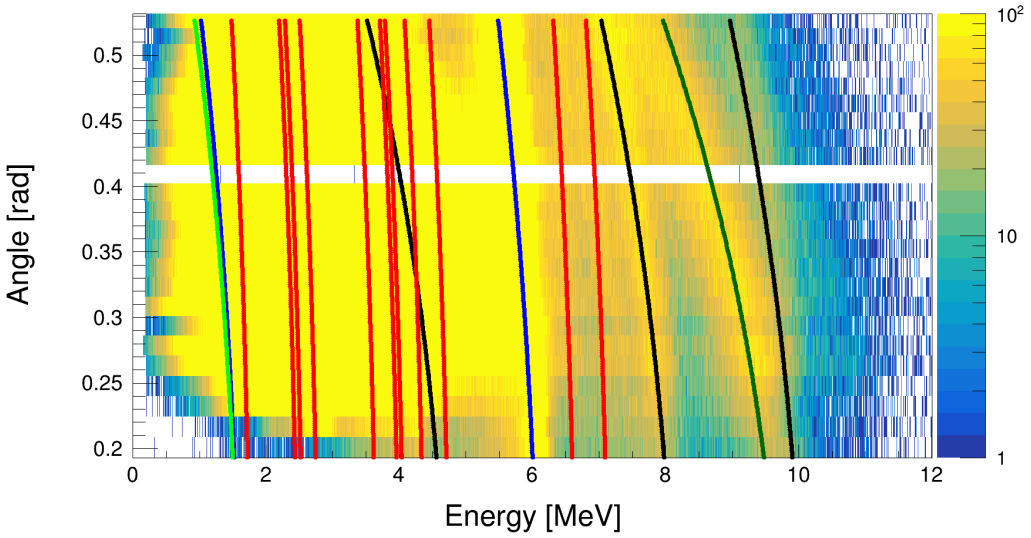


Figure 4.2: Angle in the laboratory frame *versus* the energy spectra, the 24 strips of the S3F detector are presented with their associated angular coverage. The measurement is performed at $E_{\mathrm{cm}} = 3.37$ MeV. Red, black and blue lines represent the calculated kinematic energy of the protons channels $p_i$, alpha channels $\alpha_i$ and protons from the deuterium contaminant $d_i$, respectively. The light and dark green curves represent the elastic scattering of $^{12}$C on $^{1}$H from the water contaminant on the target, and a simultaneous measurement of $\alpha_1$ and a proton from elastic scattering, respectively.

energy range, one of them is the above mentioned unidentified contamination and the other one is the protons from the reaction $^{12}\mathrm{C} + d \rightarrow {}^{13}\mathrm{C} + p$. No gamma contribution has been observed with the first one, and the second one, around $E_{\mathrm{cm}} = 2.3$ MeV the ground state kinematic energy of the proton are similar to the energy of $p_1$ events. Thus, no gamma particles coincidences from a background reaction will interfere with the $^{12}\mathrm{C} + {}^{12}\mathrm{C}$ fusion reaction measurement. It means that the background contribution in our spectra is due to false coincidences with random timing between the gamma and the charge particle. Thus, the background will be efficiently suppressed by the energy gates on gamma and particle spectra, and the remaining background can be very well evaluated with the timing analysis presented in Section 3.3.

### 4.1.2 Accuracy of analysis technique

Figure 4.3 shows the energy spectra of the 24 strips of the S3B detector at $E_{\mathrm{cm}} = 3.755$ MeV. A strong background is observed covering the energy range of the fusion events. Its

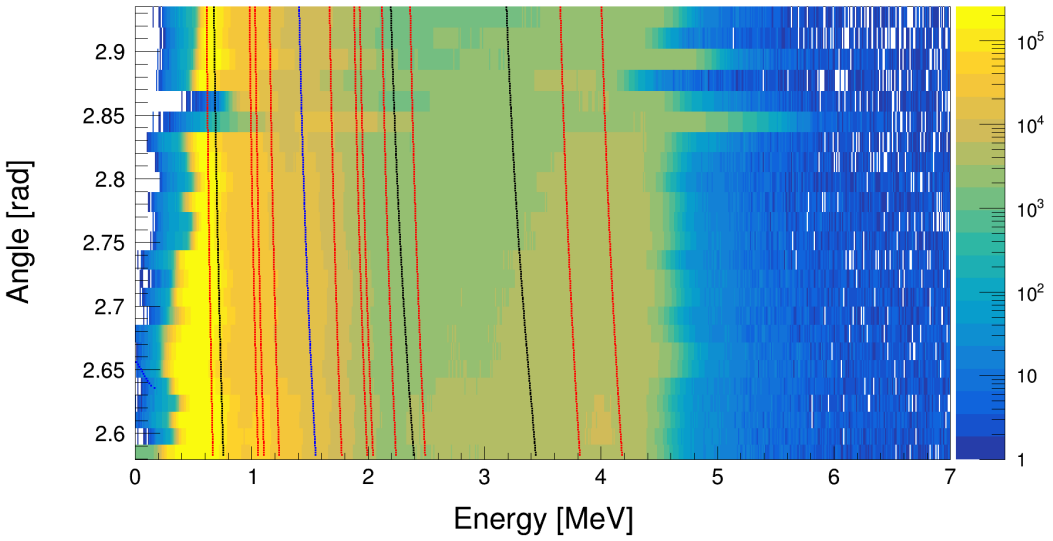


Figure 4.3: Angle in the laboratory frame *versus* the energy. The 24 strips of the S3B detector are presented with their associated angular coverage. The measurement is performed at $E_{\text{rel}} = 3.755$ MeV. The red, black and blue lines represent the calculated kinematic energy of the protons channels $p_i$, alpha channels $\alpha_i$ and protons from the deuterium contaminant $d_i$, respectively.

source is not fully understood currently, but the leading hypothesis is electrons generated by the scratching of the electrons on the target. It is impossible to see signal without coincidences, but the detector can be utilised applying them.

First, the gates over the energy are applied selecting events to extract the timing of the detector. The gate over the gamma energy stays the same and as the resolution of the charged particles' detector is affected by the beam focusing, a wide range was selected to cover well the energy region of the evaporated particles. The timing is then corrected for the alpha with the multiplicity-two method (see Section 3.3) and the resulting timing for protons and alphas is presented in Figure 4.4. It shows the timing spectrum for $\alpha_1$ in Figure 4.4.a and $p_1$ in Figure 4.4.b. A noticeable difference appears between alphas and protons. In the protons timing spectrum, there is a constant background covering the entire time coincidence range, that is not present in the alpha spectrum.

This difference comes from the gamma energy selection. The $p_1$ signal is associated to a gamma energy $E_\gamma = 440$ keV while the $\alpha_1$ signal is associated to a gamma energy $E_\gamma = 1634$ keV. Thus, at 440 keV, there are contributions in the spectrum from Compton events, mostly from the self-activity of the $LaBr_3$ (Ce) detectors, generating false coincidences with an event in the enormous background contribution in the S3B

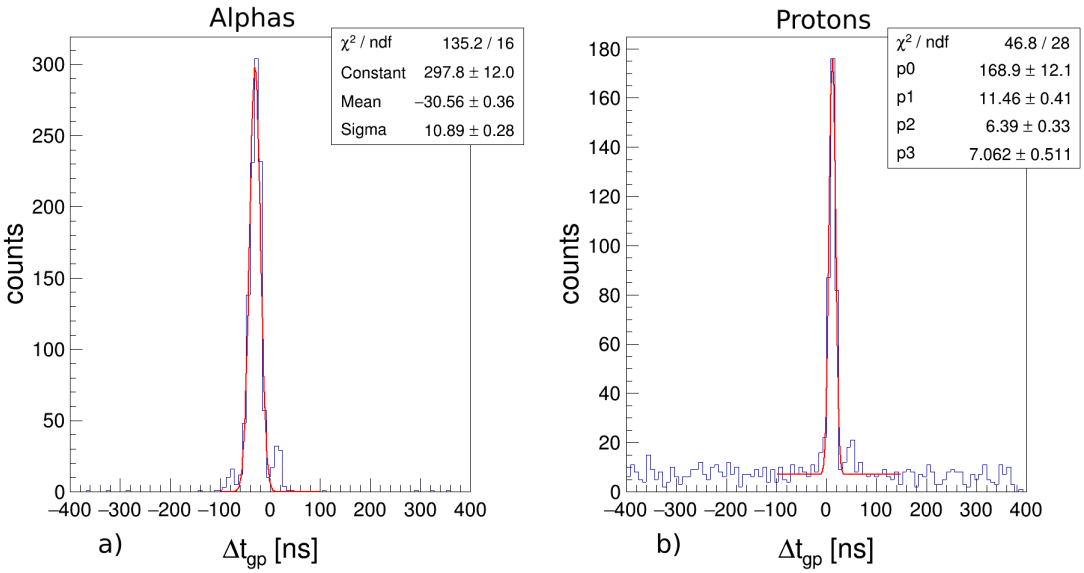


Figure 4.4: Corrected time differences spectrum between the gamma and the charged particles in the 24 strips of S3B detector at $E_{\mathrm{rel}} = 3.755$ MeV for $\alpha_1$ and $p_1$, a) and b), respectively.

detector. However, a clear peak appears and the timing selection gate can unambiguously be defined, fitted with a gaussian with the parameters given in the top-right box in the Figure 4.4.a and .b, for both alphas and protons, respectively.

Figures 4.5 and 4.6 show the charged particle energy spectra with the application of the selection gates. For the timing selection, the events inside the gate selection within three sigma range (parameters from Figure 4.4) are taken. To estimate the background, a three sigma interval centered with an offset of 300 ns, hence non-coincident, was chosen to estimate contribution inside the defined energy gates.

Comparing the Figures 4.3 and 4.5, a strong background reduction is observed. The $\alpha_1$ peak cannot be observed in Figure 4.3, while it is clearly observed in Figure 4.5, inside the energy range limited by the black crosses individually for each strip of the detector. The strong background reduction seen in Figure 4.5 is permitted thanks to extremely efficient gamma energy cuts. The energy region around $E_\gamma = 1634$ keV, is absent of almost any Compton background, the rate of false coincidence is very low. For the proton channel, with a gamma energy selection around $E_\gamma = 440$ keV, the Compton background is important and also reflects in the noise observed on Figure 4.3. The background reduction is less effective, but still allows the reliable measurement of $p_1$ events, in the energy range delimited by the red crosses in Figure 4.6.

The same method is applied for the S3F detector and the resulting counts for both detectors are reported in Table 4.1.

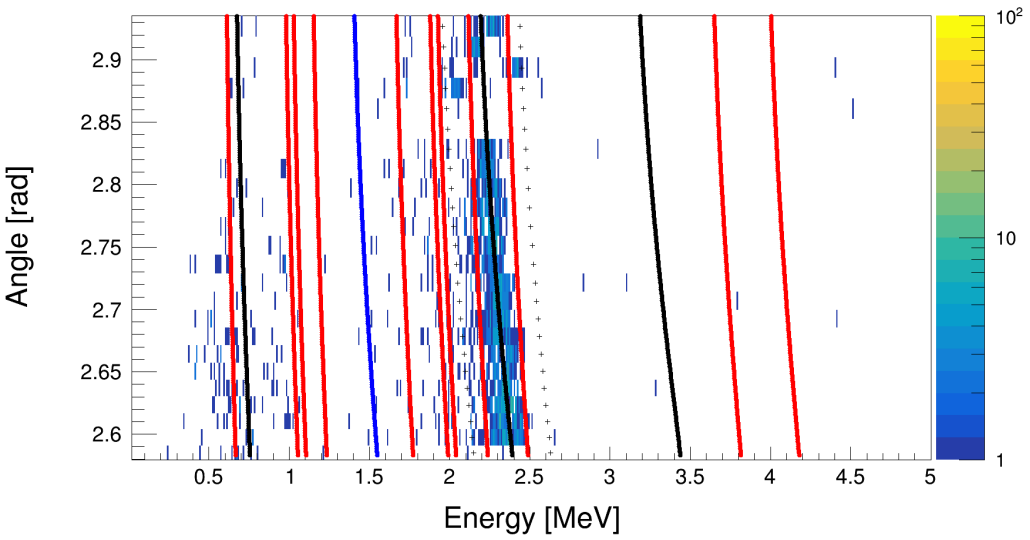


Figure 4.5: Angle in the laboratory frame *versus* the energy. The 24 strips of the S3B detector are presented with their associated angular coverage. The measurement is performed at $E_{\text{rel}} = 3.755$ MeV. The red, black and blue lines represent the calculated kinematic energy of the protons channels $p_i$, alpha channels $\alpha_i$ and protons from the deuterium contaminant $d_i$, respectively. The selection gates (gamma energy and time) are applied for the $\alpha_1$ channel and the black crosses define the charged particle energy interval selecting fusion events.

Table 4.1: Signal and background counts at $E_{\text{rel}} = 3.755$ MeV.

| | $N$ | $B$ | $S = N - B$ |
|---|---|---|---|
| $p_1$ S3B | 341 | 25 | 316 |
| $\alpha_1$ S3B | 911 | 1 | 910 |
| $p_1$ S3F | 706 | 1 | 705 |
| $\alpha_1$ S3F | 2872 | 0 | 2872 |

The measured counts $N$ and the measured background $B$ give the resulting fusion signal $S = N - B \pm \sqrt{N + B}$. To extract the cross-section from it, a normalization is made as presented in Section 1.2.2, also with the transformation to the center of mass system. To get the total cross-section, the angular differential cross-section have to be integrated over the full solid angle and need to be corrected by the contribution of the exit channel to the total cross-section. This work focuses on first excited states of the alpha and proton channels, so that the branching correction has to consider the

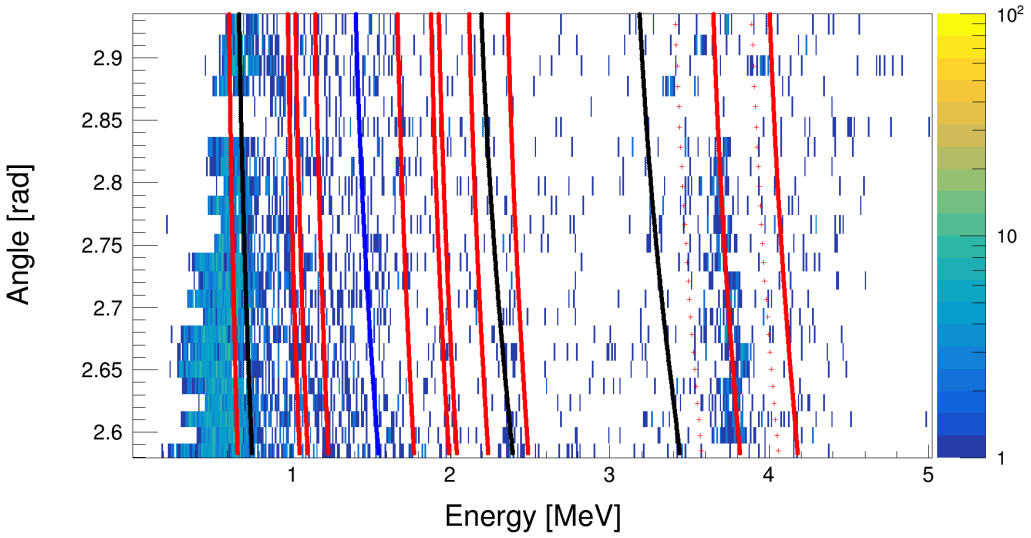


Figure 4.6: Angle in the laboratory frame *versus* the energy. The 24 strips of the S3B detector are presented with their associated angular coverage. The measurement is performed at $E_{\text{rel}} = 3.755$ MeV. The red, black and blue lines represent the calculated kinematic energy of the protons channels $p_i$, alpha channels $\alpha_i$ and protons from the deuterium contaminant $d_i$, respectively. The selection gates are applied for the $p_1$ channel (gamma and time) and the red crosses define the charged particle energy interval selecting fusion events.

fraction of the first excited state of both channels in the total cross-section.

This fraction is estimated using the experimental data of Becker *et al.* [17], in an energy range between $E_{\text{cm}} = 2.7$ MeV and $E_{\text{cm}} = 6.0$ MeV. Figure 4.7 shows, in the upper panel, the fraction of $p_1$ over the total proton cross-section in the lower panel for $\alpha_1$ over the total alpha cross-section. In this energy range, excited states up to $p_{16}$ and $\alpha_{12}$ were taken into account. The resulting fraction is summarized in Table 4.2, considering the mean value of the contribution with an associated systematic fit uncertainty of 4.5%.

The total cross-section for an exit channel is the angular differential cross-section integrated on all the solid angle with the following:

$$\sigma^{cm}_{\alpha/p} = 4\pi \left(\frac{\mathrm{d}\sigma_{\alpha/p}}{\mathrm{d}\Omega}\right)_{cm} \Gamma_{\alpha/p}, \tag{4.2}$$

with $\left(\frac{\mathrm{d}\sigma_{\alpha/p}}{\mathrm{d}\Omega}\right)_{cm}$ the differential cross-section in the center of mass system for the alpha or the proton channel with its associated branching correction $\Gamma_{\alpha/p}$. The relative uncertainties described in Chapter 2.2 associated to the measurement comes from the

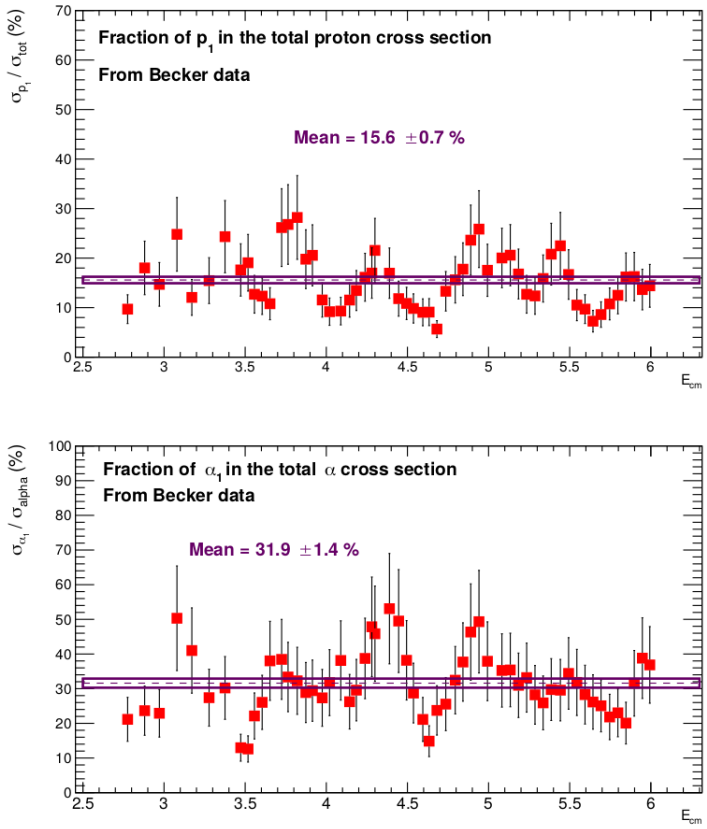


Figure 4.7: Mean of the fraction of the first excited state in the total cross-section for the proton and the alpha channels, upper panel and lower panel, respectively. The experimental data are extracted from Becker *et al.* [17], Figure taken from [40].

Table 4.2: Fraction of the measured excited states for the alpha and proton channels (fusion data from Becker *et al.* [17], values taken from [40]).

| Measured excited states | Fraction of the total proton cross-section |
|---|---|
| $p_0$ to $p_7$ | 73% |
| $p_0$, $p_1$ | 28.4% |
| $p_1$ | 15.6% |
| Measured excited states | Fraction of the total proton cross-section |
| $\alpha_0$ to $\alpha_3$ | 65% |
| $\alpha_0$, $\alpha_1$ | 48% |
| $\alpha_1$ | 31.9% |

number of nuclei involved in the measurement, so the beam intensity and the thickness of the target with a relative uncertainty of 12%, 10% regarding the gamma efficiency of the $LaBr_3$ (Ce) configuration, 4.5% associated to the cross-section correction with the branching of the contributing excited states and 3% for the solid angle uncertainty, coming mostly from the position of the detector with respect to the beamspot on the target known at a 0.5 mm precision [40]. The total relative systematic uncertainty is given by:

$$\frac{\Delta\sigma^{syst.}}{\sigma} = \frac{\sqrt{12^2 + 10^2 + 4.5^2 + 3^2}}{S} = 16.5\% \tag{4.3}$$

The statistical uncertainties are estimated using:

$$\frac{\Delta\sigma^{stat.}}{\sigma} = \sqrt{\Delta N^2 + \Delta B^2} = \frac{\sqrt{N+B}}{S} \tag{4.4}$$

with $N$ the measured counts, $B$ the measured background and $S = N - B$. The cross-section resulting of this work will be expressed with statistical uncertainties only.

To confirm the consistency of the experiment, at the energy analysed in this section, $E_{rel} = 3.755$ MeV, the cross-section is extracted from both S3F and S3B independently. The transformation from counts to cross-section is made using the following:

$$\left(\frac{d\sigma}{d\Omega}\right)_{\text{lab}} = \frac{S}{I \times N_t \times \Delta\Omega \times \epsilon} \,. \tag{4.5}$$

With $I$ and $N_t$ ne number of nuclei involved in the reactions, $\Delta\Omega$ the solid angle covered by the detectors and $\epsilon$ the gamma efficiency. The cross section in the lab frame is then transformed into the center of mass system using the equations defined in Section 1.2.2 and normalized to $4\pi$ and corrected with the right branching.

Table 4.3: Total cross-section at $E_{\text{rel}} = 3.755$ MeV.

| | $\sigma_{\text{tot}}$ S3F [mb] | $\sigma_{\text{tot}}$ S3B [mb] |
|---|---|---|
| Proton channel | $3.03 \times 10^{-3} \pm 0.114 \times 10^{-3}$ | $2.50 \times 10^{-3} \pm 0.152 \times 10^{-3}$ |
| Alpha channel | $1.57 \times 10^{-2} \pm 0.029 \times 10^{-2}$ | $1.76 \times 10^{-2} \pm 0.058 \times 10^{-2}$ |

Table 4.3 contains the measured total cross-sections for the proton and the alpha channels with the statistical uncertainties of one sigma. For the alpha channel, the S3B and S3F detector measurements agree within 10% and within 18% for the proton channel, possibly caused by the dominant background in the S3B detector. Thus, the measurement is consistent between the two detectors considering the systematic uncertainties. For the lower energies, only the S3F detector will be used due to the noise in the S3B detector.

### 4.1.3 Exploring a resonance structure around $E_{rel} = 3.2$ MeV

The striking feature of this energy region is that Spillane *et al.* data [9] shows a well defined resonance structure in the alpha channel, but not in the proton channel. They measured the cross-section using gammas only, thus, the proton channel at $E_\gamma = 440$ keV, is subject to Compton background contaminating the measurement. STELLA can provide better precision on the proton channel, employing gamma, particle and gamma-particle measurements. Six energies in this region have been investigated, namely $E_{rel} = 3.370, 3.283, 3.230, 3.128, 3.102, 3.054$ MeV.

The timing gates used for the measurements have been extracted independently for all energies investigated here, to increase the precision of the event selection, considering three sigmas acceptance.

The time inter-strip alignment method using multiplicity-two charge sharing events was developed at this energy ($E_{rel} = 3.370$ MeV). The figures 4.8 a and b show the resulting corrected gamma-particle timing fitted by gaussians defining the timing selection gates (parameters in the box) in the S3F detector. It can be observed that the $\sigma_t$ is quite large, with respect to the data at $E_{rel} = 3.755$ MeV. This might have several reasons ranging from the beam intensity, the focusing of the beam, the detector performance, and the time synchronization during data taking with periods of days. The parameters in the boxes of the Figures 4.8 a and b are used within a three sigma confidence interval, as statistics allows for a precise determination of the timing parameters, to determine the timing selection gate.

Figure 4.9 shows the angle in the laboratory frame *versus* the energy for the 24 strips of the S3F detector and their associated angular coverage at the energy $E_{rel} = 3.370$ MeV. The kinematic calculations of the available channels are displayed in red and black for protons and alphas, respectively. Blue line indicates the contaminant reaction with deuterium in the target. The nominal energy of elastic scattering with hydrogen contaminant (light green) and a combination of $\alpha_1$ with a proton from elastic scattering (dark green) are marked as well. The selected event for signal and noise evaluation are contained between the black crosses around the $\alpha_1$ kinematic line.

Table 4.4 shows the counts resulting from the event selection. The proton channel in the S3B detector is contaminated by background that prohibits a precise and consistent measurement. At this stage of the analysis, only S3F detector will be used to measure the cross-section.

The time alignment method using gamma-particles coincidences is based on the analysis of the energy point at $E_{rel} = 3.283$ MeV, where the time alignment is set for all the data using the same detectors. The time difference between gamma and charged particles, as already discussed in Section 3.3, allows to apply narrow selection gates. For the measurements around the resonance studied around 3.2 MeV,

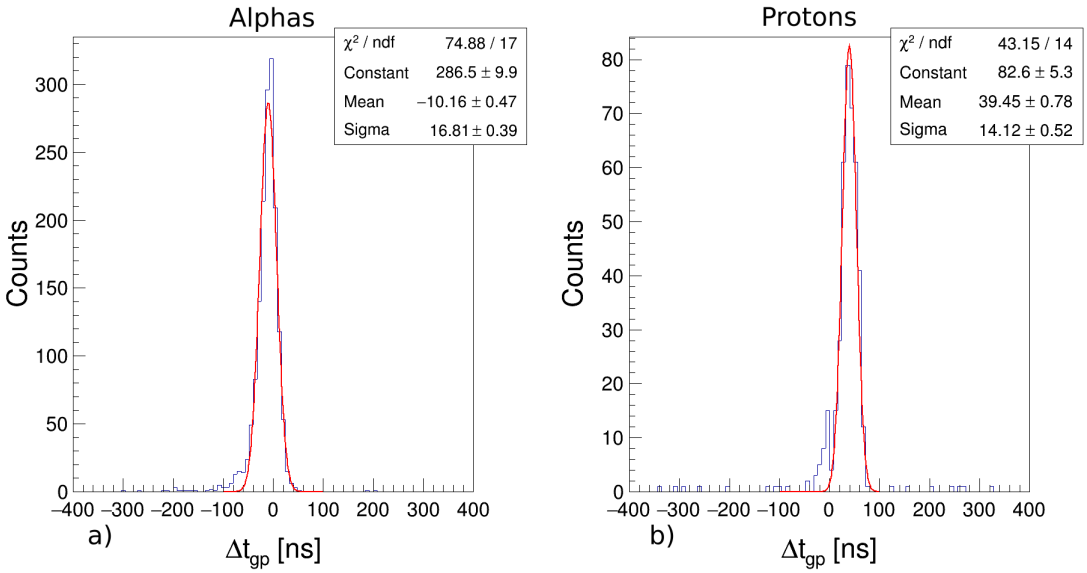


Figure 4.8: Corrected time difference spectrum between gammas and the charged particles in the 24 strips of S3F detector at $E_{\mathrm{rel}} = 3.370$ MeV for $\alpha_1$ and $p_1$, a) and b) respectively.

Table 4.4: Signal and background counts at $E_{\mathrm{rel}} = 3.370$ MeV.

| | $N$ | $B$ | $S = N - B$ |
|---|---|---|---|
| $p_1$ S3B | 768 | 671 | 97 |
| $\alpha_1$ S3B | 352 | 15 | 337 |
| $p_1$ S3F | 572 | 7 | 565 |
| $\alpha_1$ S3F | 1614 | 0 | 1614 |

time selection gate will be determined independently with mostly a three sigma range selection around the mean value.

A low number of counts is observed in the proton channel at $E_{\mathrm{rel}} = 3.230$ MeV (Table 4.5), and the events selection is then more sensitive to background events. Thus, to have a better precision on the background level observed, its evaluation in the analysis change from the other energy points on the resonance. The background analysis is evaluated in a wider range. Figure 4.11 shows a time difference spectrum between gamma and charged particles for the proton channel ($p_1$). The parameters from the gaussian fit in the box are subject to uncertainties stronger than the previous distribution observed, due to the lower statistic. As the measurement inside the selection gates, $N$ seen with the red arrow in Figure 4.11, contains also background $B$ (green arrow on the same Figure) with the fusion signal $S = N - B$, a good understanding of

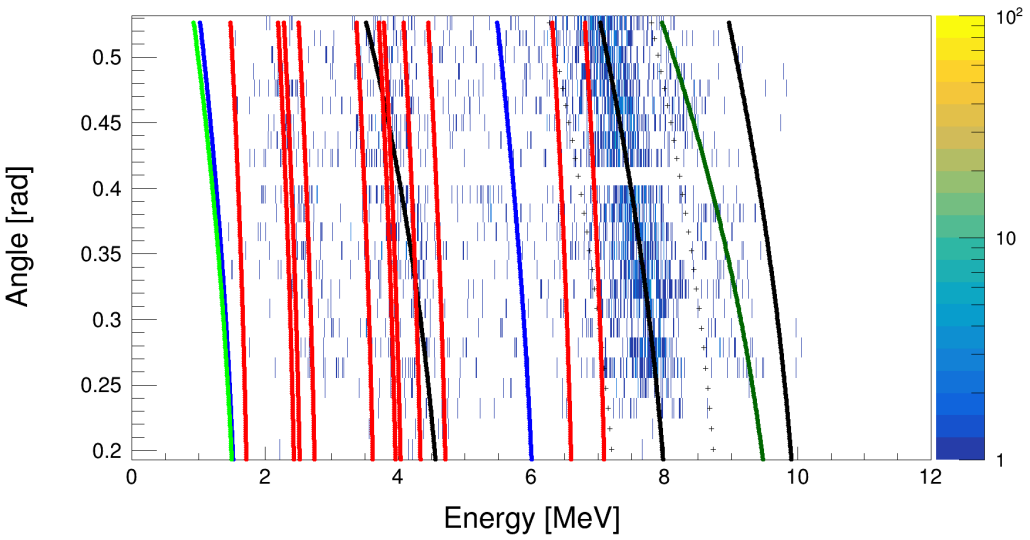


Figure 4.9: Angle in the laboratory frame *versus* the energy. The 24 strips of the S3F detector are presented with their associated angular coverage. The measurement is performed at $E_{\mathrm{cm}} = 3.370$ MeV and coincident events with $\alpha_1$ selection rules applied. The red, black and blue lines represent the calculated kinematic energy of the protons channels $p_i$, alpha channels $\alpha_i$ and protons from the deuterium contaminant $d_i$, respectively. The light and dark green curves represent the elastic scattering of $^{12}$C on $^{1}$H from water contaminant on the target, and a simultaneous measure of $\alpha_1$ and a proton from elastic scattering, respectively.

it is crucial. To optimise the signal and background evaluation, three sigma range of the gaussian are used to evaluate the signal, delimited by the red vertical lines on the plot. The background is evaluated outside this interval (red line) to the vertical green line. The background estimation is hence obtained in a six times wide range of the timing domain. It leads to 7 counts measured in six times the timing range evaluated, adding up to $B = 7/6 \approx 1$ count.

A strong drop of the counts number in the proton channel appears. Comparing the ratio between protons and alphas in S3F, 0.35 at $E_{\mathrm{rel}} = 3.370$ MeV, 0.15 at $E_{\mathrm{rel}} = 3.283$ MeV and 0.05 at $E_{\mathrm{rel}} = 3.230$ MeV (see Table 4.5). It seems that on the contrary, the resonance effect is reversed in the proton channel, as it goes up again with a ratio of 0.19 at $E_{\mathrm{rel}} = 3.128$ MeV, 0.37 at $E_{\mathrm{rel}} = 3.102$ MeV and 0.19 at $E_{\mathrm{rel}} = 3.054$ MeV, in Table 4.5.

The variation of the ratio is an indication that the contribution of the channels varies with respect to the energy and that the resonance might not be as strong in

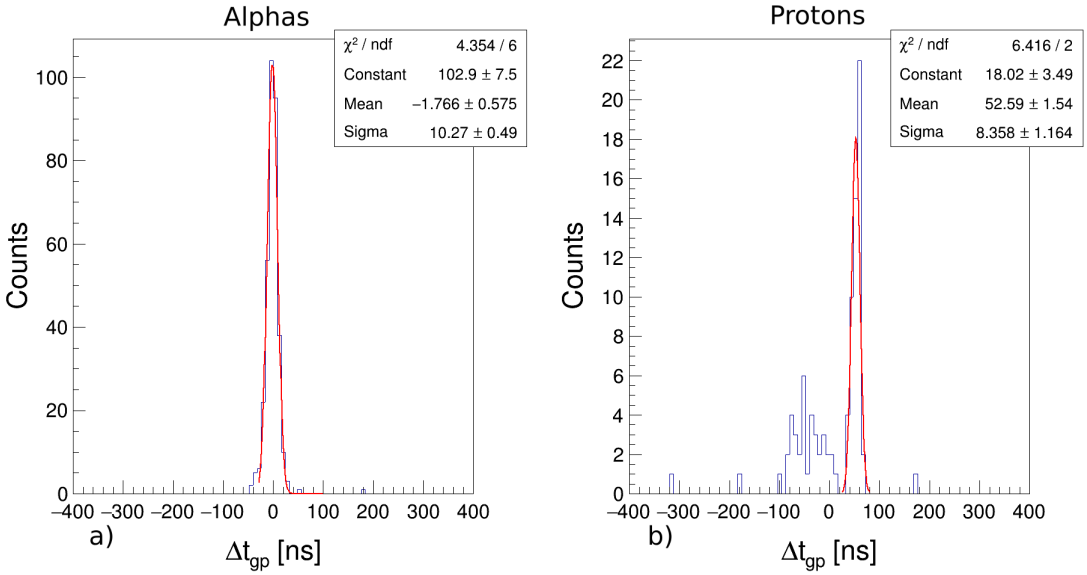


Figure 4.10: Corrected time difference spectrum between gammas and charged particles in the 24 strips of S3F detector at $E_{\mathrm{rel}} = 3.283$ MeV for $\alpha_1$ and $p_1$, a and b respectively.

Table 4.5: Signal and background counts at the energy investigated around the resonance structure at $E_{\mathrm{rel}} = 3.2$ MeV.

| $E_{\mathrm{rel}}$ [MeV] | Channel | $N$ | $B$ | $S = N - B$ |
|---|---|---|---|---|
| 3.283 | $p_1$ | 52 | 0 | 52 |
| | $\alpha_1$ | 338 | 0 | 338 |
| 3.230 | $p_1$ | 17 | 1.16 | 15.84 |
| | $\alpha_1$ | 352 | 1 | 351 |
| 3.128 | $p_1$ | 65 | 2 | 63 |
| | $\alpha_1$ | 336 | 0 | 336 |
| 3.102 | $p_1$ | 130 | 1 | 129 |
| | $\alpha_1$ | 348 | 0 | 348 |
| 3.054 | $p_1$ | 49 | 4 | 45 |
| | $\alpha_1$ | 239 | 0 | 239 |

both channels.

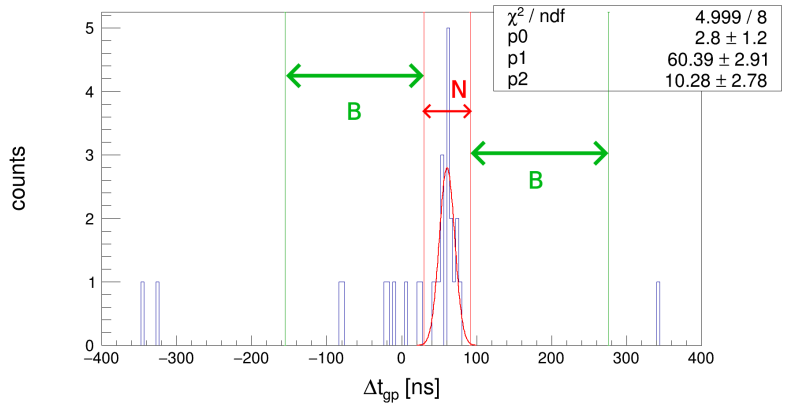


Figure 4.11: Corrected time difference spectrum between gammas and charged particles in the 24 strips of S3F detector at $E_{\mathrm{rel}} = 3.230$ MeV for $p_1$.

### 4.1.4 Low energy measurement: $E_{\mathrm{rel}} = 2.320$ MeV.

The aim of this measurement is to determine the cross-section at the base of a resonant structure possibly identified at $E_{\mathrm{rel}} = 2.14$ MeV by Spillane [9]. It has been investigated already by the STELLA collaboration (Fruet *et al.* [37]) at $E_{\mathrm{rel}} = 2.16$ MeV and at $E_{\mathrm{rel}} = 2.60$ MeV, giving a point in the alpha channel for the first energy and a limit for the second, and the inverse situation in the proton channel, namely a limit at the first energy and a point at the second one. To determine if there is a resonance or not, measuring at the tail of the resonance was mandatory. During this work, the goal was to obtain a data point with reasonable uncertainties, providing more information on the resonance structure and the global trend, i.e. if the hindrance is observed or not, considering that the measurement from STELLA in Fruet *et al.* [37] was in better agreement with the hindrance model [36] using a $\chi^2$ analysis.

The low energy measurement at $E_{\mathrm{rel}} = 2.320$ MeV took a large part of the beam time, but the cross-section is so small that the number of events does not allow to build distributions, only few counts that need to be identified whether they are signal or background.

For identifying fusion events as for the other points, the charged particle energy selection is taken reliable at a four sigma interval around the calculated kinematic energy. The gamma energy selection is considered at a three sigma range around the mean value of the nominal energy as the calibration is very reliable. The gamma-particle timing selection discussed in Section 3.3 is more difficult to restrict at this energy. It has been pointed that the timing gate might be drifting with time or energy. However, no systematic behaviour has been observed (see Figure 3.26 in Section 3.3).

Thus, the gate considered is set with a five sigmas interval from the parameters taken at the energy $E_{\text{rel}} = 3.283$ MeV. The background evaluation is based on the same method as the analysis of the point at $E_{\text{rel}} = 3.230$ MeV, considering six times the background starting at the limit of the gates to increase the statistical precision of the background estimated.

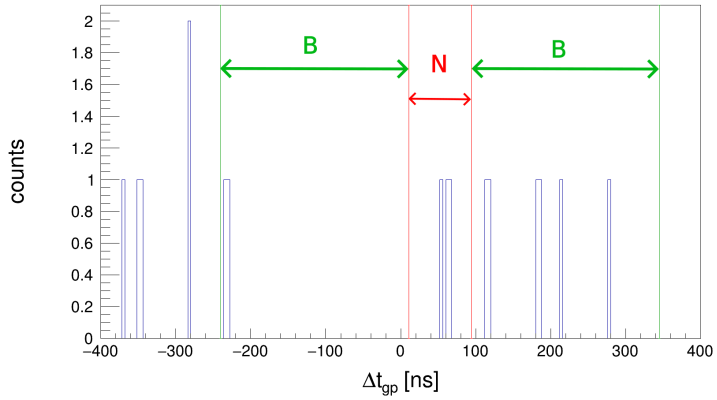


Figure 4.12: Corrected time difference spectrum between gammas and charged particles in the 24 strips of S3F detector at $E_{\text{rel}} = 2.320$ MeV for $p_1$.

Figure 4.12 shows the time difference spectrum between gammas and charged particles with energy gates on gamma and particle energy for the $p_1$ channel at $E_{\text{rel}} = 2.320$ MeV. The red lines are the upper and lower limits of the coincident event selection and the red lines the limit of the background evaluation. For this point, a conservative five sigma wide timing gate was applied, taking into account all possible drifts during the data taking, as the measurement of this point lasts more than six weeks. Three counts are measured inside the gates ($N = 3$) and eight counts are measured for the background over a six times wide gate ($B = 8/6$).

Figure 4.13 shows the time difference plot but for the $\alpha_1$ channel. Two counts are inside the gate and no count are outside. As already mentionned, the gamma energy selection is very effective for the $\alpha$ channel because the gamma energy, $E_\gamma = 1634$ keV is not subject to Compton background, reducing drastically the false coincidence's probability.

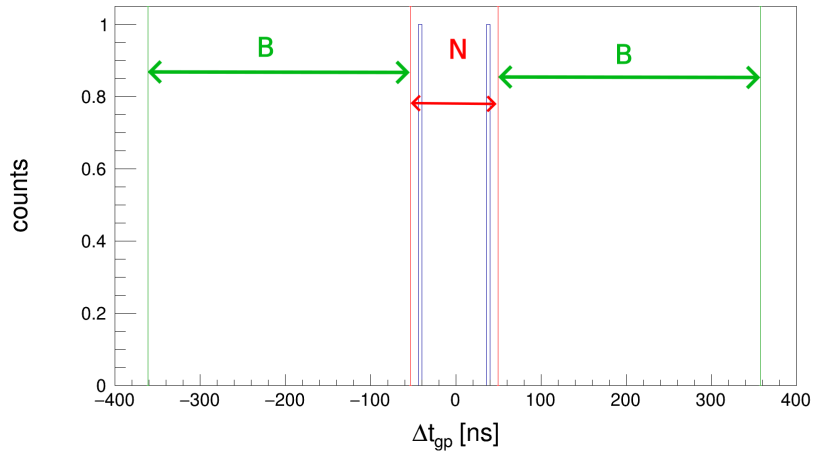


Figure 4.13: Corrected time difference spectrum between gammas and charged particles in the 24 strips of S3F detector at $E_{\mathrm{rel}} = 2.320$ MeV for $\alpha_1$.

Table 4.6: Signal and background measurement at $E_{\mathrm{rel}} = 2.320$ MeV.

| | $N$ | $B$ |
|---|---|---|
| $p_1$ | 3 | 1.33 |
| $\alpha_1$ | 2 | 0 |

## 4.2 Discussion: $S$-factor and astrophysics impact

### 4.2.1 Cross-sections and $S$-factor

The cross-sections resulting from the event selection described in Section 4.1 are presented in Table 4.7 with their associated energy along with the ratio $\sigma_p/\sigma_{\alpha+p}$ to compare the share of the total cross-section between the two channels. For all the measurements except the lowest one, the mid-target energy is a reasonable approximation considering the variation of the cross-section within the energy interval of the energy loss inside the target. It is slightly different at $E_{\mathrm{rel}} = 2.320$ MeV. Figure 4.14 shows the variation of the cross-section in the energy interval of the energy loss in the target, considering two models, hindrance and hindrance with a resonance at 2.15 MeV, both using parameters from Monpribat *et al.* [6] and Fruet *et al.* [37], respectively. It can be seen that the measurement falls at the tail of the resonance in agreement with both models. Therefore, alternative scenarios (e.g. additional resonance) can be ruled out putting confidence on the interpretation from Fruet *et al.* [37]. The determination of

the effective beam energy will be subject to a fit with a response function described in the same publication [37] in a further analysis.

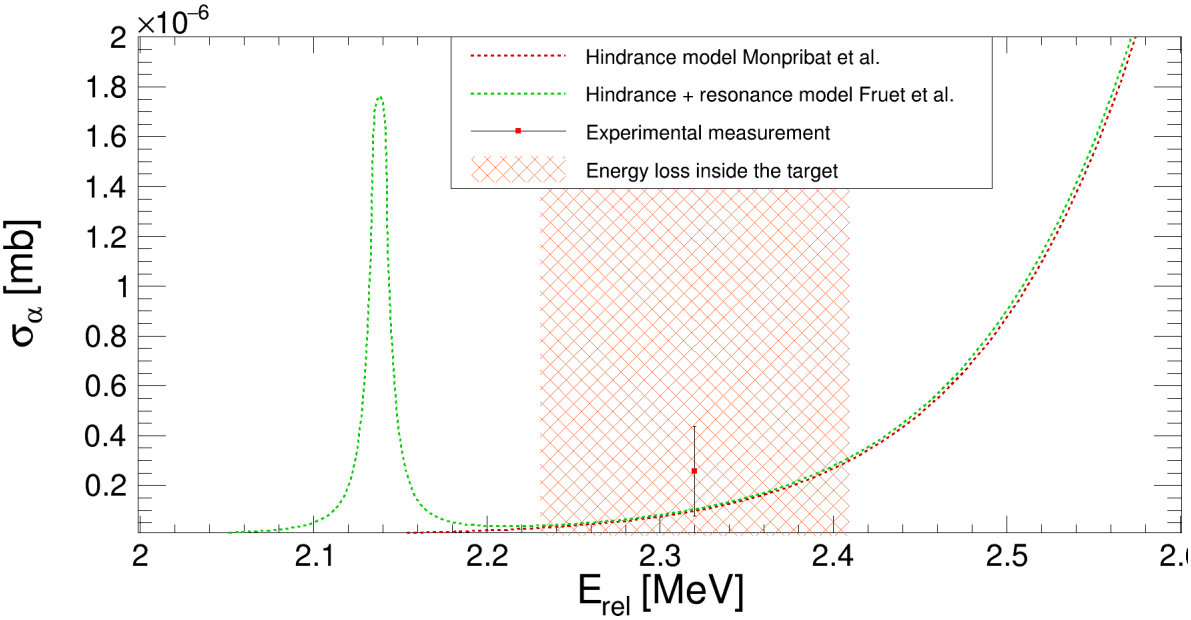


Figure 4.14: Evolution of the cross-section in the $\alpha$ channel. The red and green curves represent the hindrance and the hindrance plus resonance models, respectively, using the parameterization from Fruet *et al.* [37].

The $S$-factor is defined to reveal nuclear effects in the evolution of the cross-section offsetting the energy dependency of the exponential decrease of the cross-section caused by the tunneling effect through the Coulomb barrier. The formula of the modified $S$-factor $S^*$ is the following:

$$S^* = \sigma E \exp\left(2\pi\eta + gE\right), \tag{4.6}$$

with $\sigma$ the cross-section, $E$ the energy, $\eta = Z_1 Z_2 e^2/\hbar\nu$ the Sommerfeld parameter where $Z_1$ and $Z_2$ are the charge of the nuclei and $e$ the electrical charge, and $g = 0.122\sqrt{\mu R^3/Z_1 Z_2}$ the form factor derived for $l = 0$ states in $^{12}$C + $^{12}$C fusion reactions in a square-well potential of a radius $R$ and for a reduced mass $\mu$ [38, 59].

Figure 4.15 shows the modified $S$-factor in the alpha channel and measurements from this work are shown with the red dots. The blue ones are from the previous experimental campaigns with STELLA [37].

The results in the energy range of a resonance structure at $E_{\mathrm{rel}} = 3.2$ MeV are discussed with respect to the branching with alpha and proton emission. Spillane *et al.* [9] measured a resonance structure in the alpha channel with high accuracy.

Table 4.7: Cross-sections for the alpha and proton channel from measuring $\alpha_1$ and $p_1$. $E_{\text{beam}}$ is the energy in the center of mass system without energy loss in the target and $E_{\text{eff}}$ is the energy at the center of the target. $\sigma_p$ and $\sigma_\alpha$ are the cross-sections for the alpha and the proton channel, respectively, with associated statistical uncertainties.

| $E_{\text{beam}}$ [MeV] | $E_{\text{eff}}$ [MeV] | $\sigma_p$ [mb] | $\sigma_\alpha$ [mb] | $\sigma_p/\sigma_{\alpha+p}$ [%] |
|---|---|---|---|---|
| 3.820 | 3.755 | $3.03 \times 10^{-3} \pm 2.93 \times 10^{-4}$ | $1.57 \times 10^{-2} \pm 2.93 \times 10^{-4}$ | 16.2 |
| 3.470 | 3.370 | $5.18 \times 10^{-4} \pm 2.09 \times 10^{-5}$ | $1.90 \times 10^{-3} \pm 4.72 \times 10^{-5}$ | 21.4 |
| 3.40 | 3.283 | $1.51 \times 10^{-4} \pm 6.09 \times 10^{-6}$ | $1.29 \times 10^{-3} \pm 7.01 \times 10^{-5}$ | 10.5 |
| 3.302 | 3.230 | $3.02 \times 10^{-5} \pm 9.34 \times 10^{-6}$ | $8.62 \times 10^{-4} \pm 4.60 \times 10^{-5}$ | 3.4 |
| 3.200 | 3.128 | $6.57 \times 10^{-5} \pm 8.53 \times 10^{-6}$ | $4.51 \times 10^{-4} \pm 2.46 \times 10^{-5}$ | 12.7 |
| 3.200 | 3.102 | $8.36 \times 10^{-5} \pm 7.42 \times 10^{-6}$ | $2.90 \times 10^{-4} \pm 1.56 \times 10^{-5}$ | 22.4 |
| 3.130 | 3.054 | $3.40 \times 10^{-5} \pm 5.51 \times 10^{-6}$ | $2.33 \times 10^{-4} \pm 1.51 \times 10^{-5}$ | 12.7 |
| 2.405 | 2.320 | $1.70 \times 10^{-7} \pm 1.39 \times 10^{-7}$ | $2.56 \times 10^{-7} \pm 1.80 \times 10^{-7}$ | 39.9 |

The situation in the proton channel is less clear (see Figure 4.16). By measuring only gammas, the proton channel is strongly polluted by Compton background as discussed in Chapter 2. Also, at energies between 3.4 and 4 MeV, Spillane *et al.* and Becker *et al.* [17] are in good agreement but in the energy region of the resonance structure discrepancies start to appear. Becker *et al.* seems to observe a resonance structure too but shifted in energy by $\approx -80$ keV. This work is in good agreement with Spillane *et al.* at the basis of the resonance structure ($E_{\text{rel}} = 3.283$, 3.230 and 3.054 MeV). However, the two points measured in between ($E_{\text{rel}} = 3.128$ and 3.102 MeV) differ within two sigma range considering systematic uncertainties and there is unfortunately no data available in this work at the peak position to confirm a resonant structure in the alpha channel.

In the proton channel (Figure 4.16), Spillane *et al.* shows very large uncertainties in this region and no resonance structure can be identified. The excitation function of Becker *et al.* [17] has wider spacing in this energy region (100 keV), as compared to the measurements at higher energy (50 keV). This might be the results of a change of the experimental setup discussed in their publication. The proton channel cross-section in Becker *et al.* [17] also reveals a dip and an increase, but no clear resonant structure like in the alpha channel. Furthermore, those $S$-factors are systematically higher as compared to the measurements of Fruet *et al.* [37], Jiang *et al.* [39] and Spillane *et al.* [9]. The first one was measured with the STELLA experiment, and the second one is with a coincidence technique as well. Another measurement from Tan *et al.* [60] is

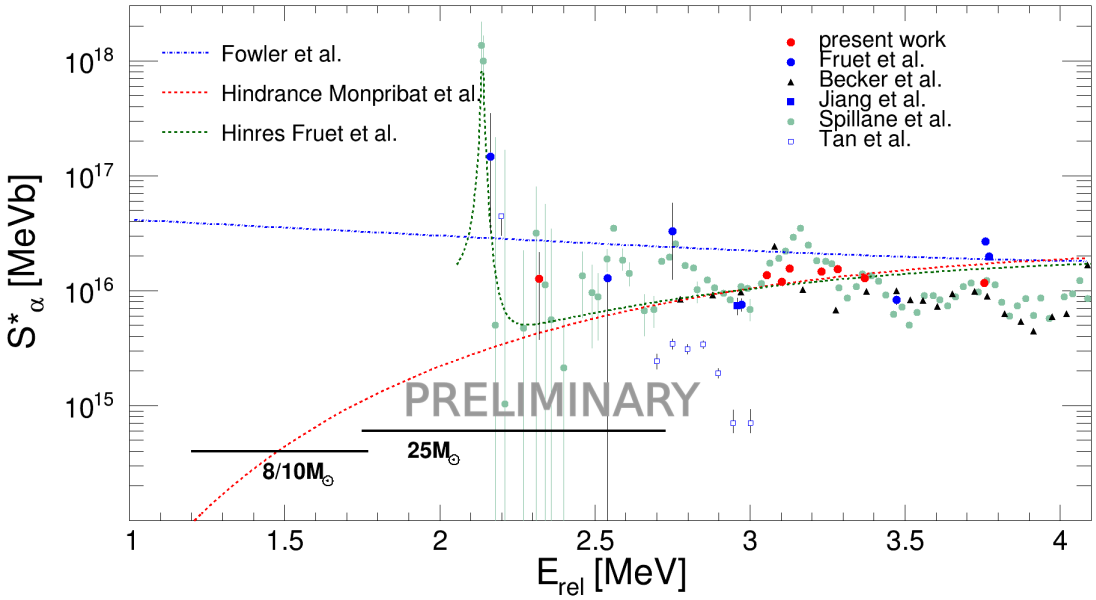


Figure 4.15: Modified $S$-factor in the alpha channel for the $^{12}C + ^{12}C$ fusion reaction. Only the statistical uncertainties are displayed. The present work is shown with the red dots, the blue ones are from the previous experimental campaign [37]. Work from other collaborations are displayed [39], [9], [60][17]. Three models are displayed, the hindrance model from Jiang *et al.* [28], but with parameterization from Fruet *et* [37] and Monpribat *et al.* [6]and a resonance at 2.14 MeV from Spillane *et al.* [9], and an optical potential fit from Fowler [61].

also using the coincidence technique, but with a thick target. Their results in $\alpha_1$ and $p_1$ are scaled with the branching extracted from Becker, the same way it is done in this work. This work with the STELLA experiment is in agreement with Spillane in the resonance region, but improves significantly the uncertainties thanks to the strong background suppression from the coincidence technique. The $S$-factor in the proton channel drops while a resonance structure in the alpha channel appears. The former seems to behave like an interference structure. Calculations with R-Matrix analysis are in progress to disentangle the phenomenon.

To sum up the $S$-factor measurement in this energy region, the results of this work is mostly consistent Spillane *et al.* improving the precision with smaller uncertainties in the proton channel allowing to observe and charcterize a possible interference structure.

The measurement at low energies from this work was performed to investigate if there is a single narrow resonance structure at $E_{\mathrm{rel}} = 2.14$ MeV or if the enhanced cross-sections are due to a global increase of the $S$-factor as predicted by the extrapolation from Fowler *et al.* [61]. In the case of the resonance, the presented interpretation

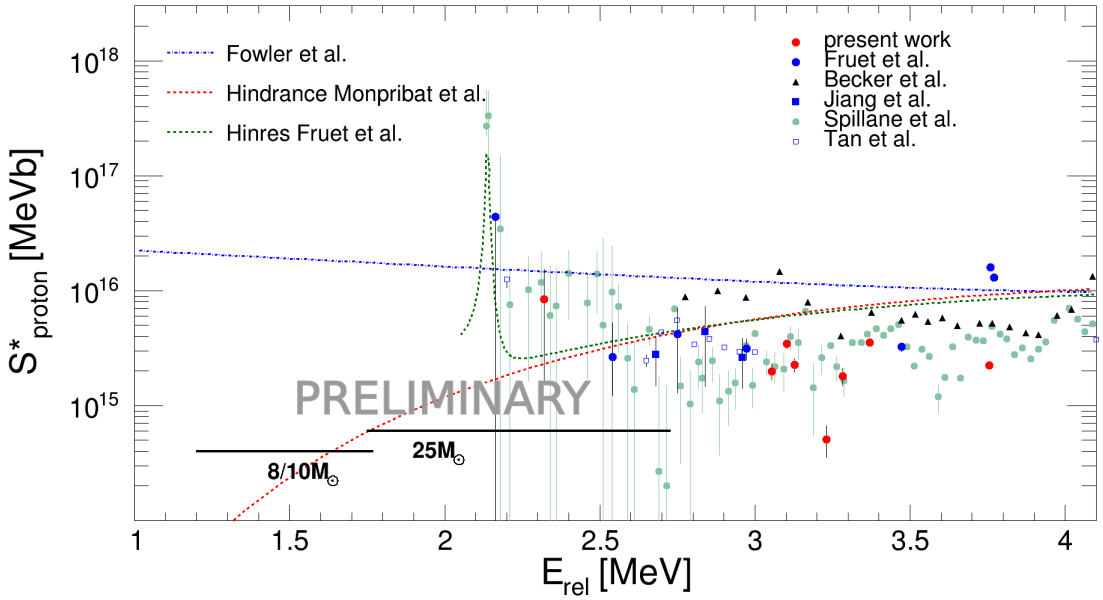


Figure 4.16: Modified $S$-factor in the proton channel for the $^{12}C + ^{12}C$ fusion reaction. Only the statistical uncertainties are displayed. The present work is shown with the red dots, the blue ones are from the previous experimental campaign [37]. Work from other collaborations are displayed [39, 9, 60, 17]. Four models are displayed, the hindrance model from Jiang *et al.* [28], but with parameterization from Fruet *et* [37] and Monpribat *et al.* [6] and a resonance at 2.14 MeV from Spillane *et al.* [9], and an optical potential fit from Fowler [61].

is based on the hindrance model with a resonance structure added to it. Previous measurements from the STELLA collaboration achieved a limit for the lowest measurement in the proton channel and a limit in the alpha channel on the second lowest measurement [37]. This work aims to obtain a data point at the tail of the resonance structure at around $E_{\mathrm{rel}} = 2.320$ MeV between those earlier measurements. This has been achieved with strongly improved uncertainties in both the alpha and the proton channel. In the alpha channel, the measurement shows good agreement with the hindrance model, but not with the Fowler calculation. The $S$-factor of the proton channel indicates a similar trend, but less clear. However, with the accuracy provided by the STELLA experiment, the picture of the $S$-factor in both channels has improved.

### 4.2.2 Astrophysical improper-fraction

The common model for carbon fusion used for stellar evolution and nucleosynthesis calculations is based on the Fowler extrapolation [61]. However, earlier work from Pignatari *et al.* [5] studied the implication of lower and higher reaction rates than the

Fowler model, multiplying and dividing them by a factor ten. The hindrance model and the hindrance with resonance at $E_{\mathrm{rel}} = 2.14$ model have been studied by Gasques *et al.* [7] and Monpribat *et al.* [6]. Both Pignatari *et al.* and Monpribat *et al.* used the GENEC code [62] for the stellar evolution calculations to study the impact of the changes of the rates. Gasques *et al.* on the other way used the FRANEC code

In a star, the amount of energy released with respect to time and mass is continuously counter balanced by expansion or contraction by reaching a hydrostatic equilibrium in the burning phase. The reaction rates of the active burning processes mostly control the adjustment of the core of the star. For example, with lower tendency of the reaction rates, the core will contract more to reach higher temperatures and thus higher relative energies between the nuclei reaching the reaction rate necessary to maintain the hydrostatic equilibrium.

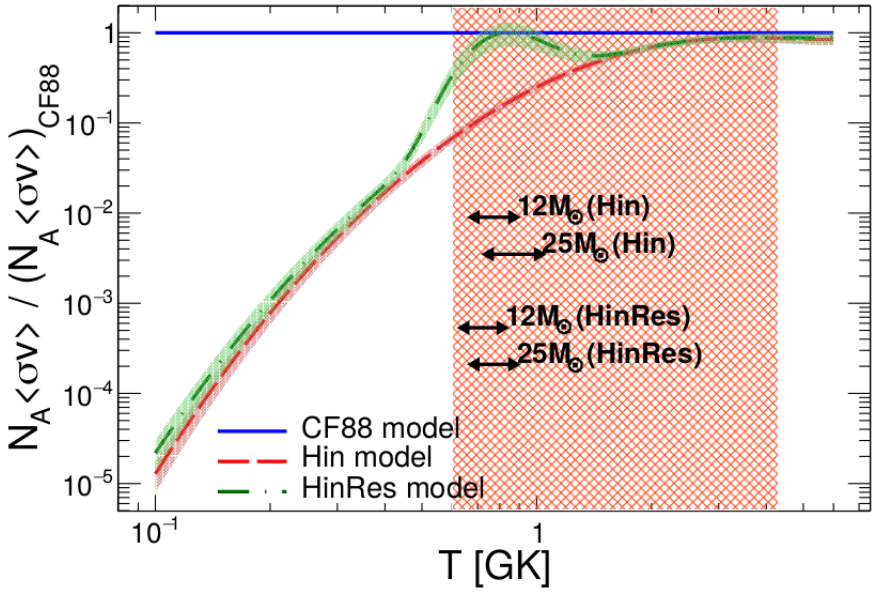


Figure 4.17: Reaction rates for the hindrance model and the hindrance plus resonance model [6] normalized to the Fowler reaction rates [61]

All the following analysis is compared with the Fowler model [61] (CF88) to highlight the changes of the studied models with respect to the most common one. Figure 4.17 shows the reaction rates for the hindrance and hindrance plus resonance model normalized to the Fowler rates. The ratio between the proton and the alpha channels with respect to the hindrance part of the total cross-section was fixed at 35% for the proton exit channel and 65% for the alpha one, and the parameters of the resonance were taken from Spillane *et al.* [9]. It has been studied for 12 and 25 $M_\odot$ stars, and for the hindrance model it shows an increase of the temperature of 10% during the carbon burning phase, shortening its duration by a factor of two [6]. This effect might

change the remnant at the end of the burning phase depending on the mass of the star.

For the hindrance plus resonance model, the results are closer to the CF88 reaction rates for the stars studied, indicating that the Gamow window for the hindrance plus resonance model falls in the energy interval of the resonance, where the reaction rates are comparable to the CF88 rates. Globally, the observed change of the reaction rate does not show major changes of the stellar evolution. However, two solar masses have been investigated and as the resonances in the $^{12}C + ^{12}C$ fusion reaction can be narrow, the temperature of the core of stars of other masses, very dependent on this parameter, can show different results. Further investigations are planned in the team to better understand the impact of hindrance and hindrance plus resonance models.

Gasques *et al.* [7] studied the effect of hindrance for $^{12}C + ^{12}C$ fusion reaction with the code FRANEC [63] focusing on massive late-type stars and carbon ignition in massive accreting white dwarfs and neutron stars. They observed in all cases pronounced effects with the hindrance models, in particular an increase of the carbon ignition temperature in white dwarf completely preventing it for inner temperature $T \leq 2 \times 10^8$ K.

The results of the present work are summarized in Table 4.7. In the last column, the ration $\sigma_p/\sigma_{\alpha+p}$, reveals a variation of the proton contribution from 39.9% to 3.4% with respect to the total cross-section. More locally, on the resonance structure around 3.2 MeV, it shows a variation of a factor seven in what could be an interference structure between the proton and the alpha channel. As most of the stellar evolution studies use a fixed ratio with 35% and 65% for the proton and alpha channel, respectively, an independent implementation of alpha and proton reactions rates might yield more precise predictions of the models.

Adsley *et al.* [4] studied specific states in the $^{24}Mg$ through the reaction $^{24}Mg(\alpha,\alpha')^{24}Mg$. They identified four $0^+$ states and associated them to a $^{12}C + ^{12}C$ cluster structure, where two of them are candidates for a resonance around $E_{cm} = 1.5$ MeV predicted by Cooper *et al.* [64], predominantly decaying through $\alpha$-particle emission with implications for the s-process in carbon burning shell. This finding is another argument that considering separate alpha and proton channels might improve the precision of the stellar models.

Pignatari *et al.* [5] provided a stellar evolution study of the variation of the reaction rate by globally multiplying or dividing them with a fixed number, but also by varying the ratio between the proton and the alpha channel with respect to the total cross-section over the entire energy range, up to a ratio of 0.95/0.05 for the ratio $R_\alpha/R_p$. They demonstrate that reducing the strength of the proton channel increases the amount of neutrons released in the star providing neutron seed for subsequent

processes. The $^{22}$Ne decay is mainly depleted through $(\alpha, n)$ and $(p, \gamma)$ during the carbon burning phase. With a strong reduction of the proton channel in the $^{12}$C + $^{12}$C reaction, the $^{22}$Ne$(\alpha, n)^{25}$Mg is thus favored releasing neutrons in the core and generating secondary reactions impacting the abundances. They observed for instance a variation of a factor 30 of Sr the abundances in the case of 0.95/0.05 ratio.

This work shows that the $S$-factor of a channel ($p$ or $\alpha$) is subject to strong variation ($R_\alpha/R_p$ of 0.966/.034) and the studies from Pignatari *et al.* [5] show that it can have a strong impact during the carbon burning phase. Based on the new data obtains in this work, further analysis could include more masses and more complex stellar evolution models (including rotations of the core *etc...*). The limit mass for stars to ignite carbon as well as matter ejection processes, could impact the global abundances. It is noteworthy mentioning that the studies described here only considered carbon burning to occur in the core. A further step would be to consider in-shell nucleosynthesis.

## 4.3 Résumé chapitre 4

Dans ce dernier chapitre nous proposons en premier lieu une discussion concernant les différentes contributions de bruit de fond, notamment la réaction $^{12}\mathrm{C} + d \rightarrow {}^{13}\mathrm{C} + p$ avec des protons et des deutons issus de l'eau contaminant la cible. Les protons ont une énergie similaire au canal $p_1$ notamment autour de $E_{\mathrm{cm}} = 2,3$ MeV, et une autre réaction dont la ligne cinématique dans le détecteur S3F semble se tenir entre les lignes $\alpha_0$ et $\alpha_1$ (Figure 4.2). Dans le premier cas, la ligne problématique dans la réaction est l'état fondamental et n'est donc pas accompanée d'émission gamma. Dans le second aucune émission gamma n'a été observée, la sélection en coïncidence permet donc de supprimer ces contributions.

Dans le jeu de données analysé, le détecteur S3B s'est avéré bruité, mais a tout de même permis de vérifier la cohérence des résultats en mesurant indépendament les sections efficaces entre S3F et S3B à l'énergie $E_{\mathrm{rel}} = 3,755$ MeV. Malgré le bruit de fond largement dominant dans le détecteur S3B, les sélections en énergie des gammas et la sélection temporelle réduisent drastiquement le bruit de fond, notamment pour $\alpha_1$ (Figure 4.5) et l'extraction des sections efficaces précise est possible. Comme seuls $\alpha_1$ et $p_1$ sont mesurés, pour extraire la section efficace totale des différents canaux, il faut tenir compte du rapport d'embranchement de ceux-ci, rapports tirés des travaux de Becker *et al.* [17]. Les incertitudes systématiques associées aux mesures sont de l'ordre de 16.5%. Les résultats dans S3F et S3B ont montrés une variation de 10% pour les alphas et 18% pour les protons. Cependant, considérant les incertitudes, ils montrent que l'analyse effectuée est cohérente.

Dans un second temps, nous avons cherché à analyser une résonance vers $E_{\mathrm{cm}} =$

3, 2 MeV où Spillane *et al.* [9] observent une structure forte dans le canal alpha qui n'apparait pas dans le canal proton. Cependant on observe que ce dernier, comme ils ne mesurent que les gammas, est sujet à des incertitudes assez importantes. A l'aide des coïncidences, nous avons pu mesurer avec davantage de précision. La première observation est une forte variation du rapport entre le nombre d'évènements mesurés pour les alphas et les protons. A tel point que pour le point à $E_{\text{rel}} = 3,230$ MeV, le bruit de fond a été évalué sur un intervalle temporel six fois supérieur à l'évaluation du signal, afin d'obtenir une meilleure estimation du bruit de fond présent dans notre signal. Ce procédé est décrit sur la Figure 4.11 et est celui utilisé pour la mesure à basse énergie à $E_{\text{rel}} = 2,320$ MeV. Cette énergie a été spécifiquement choisie car elle se trouve à la base d'une possible résonance à $E_{\text{rel}} = 2,14$ MeV où les mesures sont sujettes à de grandes incertitudes. L'idée ici est d'ajouter une un point de mesure réduisant les incertitudes.

Les résultats, montrés sous forme de facteur-$S$ (Figures 4.15 et 4.16), sont en accord général avec les mesures de Spillane *et al.* [9] dans le canal alpha en dehors de deux points dans la résonance à $E_{\text{cm}} = 3,2$ MeV, où un comportement résonant n'est pas spécifiquement observé dans nos données, cependant l'ajout d'un on de mesure au milieu aiderait à l'affirmer. Dans le canal proton en revanche, les données autour de cette énergie améliorent grandement les incertidues, où les données de Spillane sont peu précises, et une structure de type interférence apparait. De plus, dans cette région, les ratios de la section efficace proton sur proton plus alpha (colonne de droite Tableau 4.7) montrent une forte variation, où les protons ne représentent que 3,4% de la section efficace totale au plus bas de la structure d'interférence.

Le point de mesure à basse énergie montre des incertitudes réduites dans les deux canaux, et notamment dans le canal alpha on observe que le facteur-$S$ est en accord avec le modèle de suppression de la fusion de Jiang *et al.* [28] avec une résonance (paramètres de Spillane *et al.*) utilisant la paramétrisation de Fruet *et al.* [37] à un sigma, où le modèle de Fowler *et al.* [61] est en dehors des incertitudes à un sigma. De plus, les recherches sur l'effet de la suppression de la fusion et des résonances sur notre compréhension de l'évolution stellaire et de la nucléosynthèse ont montré des effets non négligeables.

Ainsi, Monpribat *et al.* [6] et Gasques *et al.* [7] ont étudié l'effet de la suppression de la fusion sur l'évolution stellaire en utilisant respectivement les codes GENEC [62] et FRANEC [63]. Ils ont notamment montré des différences dans les temps de vie de la phase de combustion du carbone dus à l'augmentation de la température nécessaire au cœur de l'étoile pour maintenir un taux de réaction assurant l'équilibre hydrostatique de l'étoile. De ce fait, la température limite pour assurer l'allumage de cette phase de combustion est plus important, empêchant un plus grand pannel d'étoile de la

démarrer. Ces modèles utilisent un ratio des contributions alphas et proton fixe de 65/35. Cependant Pignatari *et al.* [5] propose une étude utilisant également le code GENEC montrant que la variation de ce rapport, allant jusqu'à 95/5, pouvait avoir de grandes conséquences sur l'évolution stellaire et la nucléosynthèse, mettant en évidence la génération de neutrons dans le milieu créant des réaction secondaires importantes lorsque le canal alpha était plus favorisé. On voit néamoins dans notre analyse que ce ratio peut évoluer fortement. De plus, le travail récent de Adsley *et al.* [4] a mis en évidence des états moléculaires dans le $^{24}$Mg candidats pour une résonance à 1.5 MeV dans la réaction $^{12}$C + $^{12}$C qui favoriserait grandement une voie de sortie alpha. Ce qui confirme l'importance de considérer les résonances et des ratios alpha/protons évolutifs.

# Conclusion

The goals of this PhD work were firstly the cross-section measurement of the $^{12}C + ^{12}C$ fusion reaction focusing on a resonance structure appearing around $E_{cm} = 3.2$ MeV in the alpha channel of the measurement from Spillane *et al.* [9] but not in the proton channel, and improve the uncertainty of the latter exit channel. Secondly, it was attempted to investigate the tail of a supposed resonance structure at $E_{cm} = 2.14$ MeV, to improve the uncertainties in this energy region and understand if the $S$-factor is rising up as predicted by the CF88 model from Fowler *et al.* [61], or if it drops of the $S$-factor following the hindrance model from Jiang *et al.* [28] with isolated narrow resonances structure on top of it.

The measurements have been performed in a three months long experiment in 2019 where I learned all aspects of experimenting in nuclear astrophysics (stability, endurance, surveillance *etc...*). It allowed me to take the responsability of the full chamber of the STELLA (STELlar LAboratory) experiment considering all detectors, targets and pumping devices in the experimental campaign in 2022, with the commissioning and measurements with the additional detectors from PIXEL. The 2022 experiment started with five months of testing beginning with the vacuum and target engine, detectors and preamplifiers response and the implementation of PIXEL in the STELLA electronics.

The experimental setup allows for a synchronized measurement of gammas from the de-excitation of the daughter nuclei and evaporated charged particles. The former measured with UK-FATIMA (FAst TIMing Array) composed of 36 $LaBr_3(Ce)$ scitillators providing sufficient energy resolution with excellent energy calibration stability provided by the internal radioactivity and a timing response lower than nanoseconds. Charged particles inside the chamber are measured by silicon detectors protected by aluminum foils. The high angular granularity allows for precise measurement of angular distribution of the differential cross-section, improved by the addition of PIXEL detector, covering solid angles in an intermediate angular range. The time difference with coincident events is a major advantage of the STELLA apparatus, as it allows a three fold selection for events: the energy of gammas and charged particles, and the time difference between them, as described in Sections 3.3 and 4.1.

The analysis presented in this work focused on the experimental data of the 2019 campaign. A substantial part of the work was to reach the presented accuracy and to investigate paths towards even higher precision in the background suppression. In the charged particles detectors, I have performed an analysis of the contamination of the energy spectra through elastic scattering of contaminants in the target. The impact of parasitic reactions reduces with proper sorting of the multiplicity-two events (two strips triggering within a 400 ns interval), in order to separate charge sharing events from two strips triggered by two independent particles. The stability of the calibration has been verified and the energy selection gates on the charged particles detectos have been adapted to it. The timing has also been investigated and a time alignment has been performed through two different methods, reaching a precision of $\sigma_{\mathrm{gp}}$ of 8 to 15 ns. The timing gate monitored and lead us to adopt a careful and conservative approach of the analysis of the low energy point.

To increase the precision of data normalization, the target thickness measurement has been performed. We strongly improved the precision of the energy loss determination through electronic noise reduction with completing the Faraday cage and through reference signals to follow the changes of the preamplifier gain the temperature. A precision better than 10% has been reached for the thinner targets ($\sim$ 20 to 30 $\mu$g/cm$^2$) and the absence of target growth with beam irradiation has been verified.

The carbon fusion data analysis resulted in the detection of a possible interference structure in the proton channel in the energy region around $E_{\mathrm{cm}} = 3.2$ MeV, strongly improving the uncertainties compared to Spillane *et al.* [9] in this channel. R-Matrix calculations will be performed to interpret the data. The results at the low energy point measured at $E_{\mathrm{rel}} = 2.320$ MeV has improved the uncertainties of the available experimental data. The measurements agree with the hindrance model in the alpha channel within one sigma of the statistical uncertainties, while the CF88 model is beyond the one sigma range.

I am really thankfull for the opportunity to work on such a complex and complete experiment and for the trust to make me in charge of the STELLA chamber (pumping, target rotation engine, DSSSD's and monitors) during the 2022 experimental campaign. Considering the two experimental campaign and the work done on the target measurement station, I have been working on testing and improving experimental devices for one and half year during my four years of PhD, the rest was employed for the data analysis. Spending this time to optimise the data analysis the best I can was incredibly stimulating and the results reached personally very rewarding.

The STELLA experiment is permanently adapted to the relevant questions and developments are on the way to upgrade the reaction chamber. The collaboration aims to adapt the experimental setup to measure fusion cross-section for the fusion

reactions $^{12}C + ^{16}O$ and $^{16}O + ^{16}O$, which have more complex exit channels than the $^{12}C + ^{12}C$ fusion reaction. The data from the 2022 campaign are being analysed with the PIXEL detectors contributions to complete the $^{12}C + ^{12}C$ fusion cross-section picture. Impacts of the results given by the STELLA collaborations on astrophysics have been analyzed by Monpribat *et al.* [6] and further simulations should follow to gain better understanding of stellar processes during the carbon fusion and beyond.

This work of the Interdisciplinary Thematic Institute QMat, as part of the ITI 2021 2028 program of the University of Strasbourg, CNRS and Inserm, was supported by IdEx Unistra (ANR 10 IDEX 0002), and by SFRI STRAT'US project (ANR 20 SFRI 0012) and EUR QMAT ANR-17-EURE-0024 under the framework of the French Investments for the Future Program.

# Bibliography


[1] C. L. Jiang, H. Esbensen, K. E. Rehm, B. B. Back, R. V. F. Janssens, J. A. Caggiano, P. Collon, J. Greene, A. M. Heinz, D. J. Henderson, I. Nishinaka, T. O. Pennington, and D. Seweryniak, "Unexpected behavior of heavy-ion fusion cross sections at extreme sub-barrier energies," *Phys. Rev. Lett.*, vol. 89, p. 052701, Jul 2002.

[2] J.-P. Ebran, E. Khan, T. Nikšić, and D. Vretenar, "Nuclear clustering in the energy density functional approach," *Journal of Physics: Conference Series*, vol. 569, p. 012028, dec 2014.

[3] F. Hoyle, "On nuclear reactions occuring in very hot stars.i. the synthesis of elements from carbon to nickel.," *apjs*, vol. 1, p. 121, Sept. 1954.

[4] P. Adsley, M. Heine, D. G. Jenkins, S. Courtin, R. Neveling, J. W. Brümmer, L. M. Donaldson, N. Y. Kheswa, K. C. W. Li, D. J. Marín-Lámbarri, P. Z. Mabika, P. Papka, L. Pellegri, V. Pesudo, B. Rebeiro, F. D. Smit, and W. Yahia-Cherif, "Extending the hoyle-state paradigm to $^{12}$C+$^{12}$C fusion," *Phys. Rev. Lett.*, vol. 129, p. 102701, Sep 2022.

[5] M. Pignatari, R. Hirschi, M. Wiescher, R. Gallino, M. Bennett, M. Beard, C. Fryer, F. Herwig, G. Rockefeller, and F. X. Timmes, "The 12c + 12c reaction and the impact on nucleosynthesis in massive stars," *The Astrophysical Journal*, vol. 762, p. 31, dec 2012.

[6] Monpribat, E., Martinet, S., Courtin, S., Heine, M., Ekström, S., Jenkins, D. G., Choplin, A., Adsley, P., Curien, D., Moukaddam, M., Nippert, J., Tsiatsiou, S., and Meynet, G., "A new 12c + 12c nuclear reaction rate: Impact on stellar evolution," *A&A*, vol. 660, p. A47, 2022.

[7] L. R. Gasques, E. F. Brown, A. Chieffi, C. L. Jiang, M. Limongi, C. Rolfs, M. Wiescher, and D. G. Yakovlev, "Implications of low-energy fusion hindrance on stellar burning and nucleosynthesis," *Phys. Rev. C*, vol. 76, p. 035802, Sep 2007.

[8] M. Heine, S. Courtin, G. Fruet, D. Jenkins, L. Morris, D. Montanari, M. Rudigier, P. Adsley, D. Curien, S. Della Negra, J. Lesrel, C. Beck, L. Charles, P. Dené, F. Haas, F. Hammache, G. Heitz, M. Krauth, A. Meyer, Z. Podolyák, P. Regan, M. Richer, N. de Séréville, and C. Stodel, "The stella apparatus for particle-gamma coincidence fusion measurements with nanosecond timing," *Nuclear Instruments and Methods in Physics Research Section A: Accelerators, Spectrometers, Detectors and Associated Equipment*, vol. 903, pp. 1–7, 2018.

[9] T. Spillane, F. Raiola, C. Rolfs, D. Schürmann, F. Strieder, S. Zeng, H.-W. Becker, C. Bordeanu, L. Gialanella, M. Romano, and J. Schweitzer, "$^{12}$C +$^{12}$ C fusion reactions near the gamow energy," *Phys. Rev. Lett.*, vol. 98, p. 122501, Mar 2007.

[10] S. Basu and H. Antia, "Helioseismology and solar abundances," *Physics Reports*, vol. 457, no. 5, pp. 217–283, 2008.

[11] A. Maeder, *Physics, Formation and Evolution of Rotating Stars*. Springer, 2009.

[12] "Stellar evolution - cycles of formation and destruction : Introduction to the h-r diagram." "https://chandra.harvard.edu/edu/formal/stellar_ev/story/index3.html.

[13] C. Ilidadis, *Nuclear Physics of Stars*. WILEY-VCH, 2007.

[14] K. Lodders, H. Palme, and H.-P. Gail, "4.4 abundances of the elements in the solar system: Datasheet from landolt-börnstein - group vi astronomy and astrophysics · volume 4b: "solar system" in springermaterials (https://doi.org/10.1007/978-3-540-88055-4_34)."

[15] D. Tilley, C. Cheves, J. Kelley, S. Raman, and H. Weller, "Energy levels of light nuclei, a = 20," *Nuclear Physics A*, vol. 636, no. 3, pp. 249–364, 1998.

[16] R. Bass, *Nuclear Reactions with Heavy Ions*. Springer-Verlag, 1980.

[17] H. Becker, K. Kettner, C. Rolf, and H. Trautvetter, "the $^{12}$C + $^{12}$C reaction at subcoulomb energies (ii)*," *Z. Phys. A - Atoms and Nuclei*, vol. 303, pp. 305–312, August 1981.

[18] E. Almqvist, D. A. Bromley, and J. A. Kuehner, "Resonances in c$^{12}$ on carbon reactions," *Phys. Rev. Lett.*, vol. 4, pp. 515–517, May 1960.

[19] M. Chernykh, H. Feldmeier, T. Neff, P. von Neumann-Cosel, and A. Richter, "Structure of the hoyle state in $^{12}$C," *Phys. Rev. Lett.*, vol. 98, p. 032501, Jan 2007.

[20] E. Vogt and H. McManus, ""molecular" states formed by two carbon nuclei," *Phys. Rev. Lett.*, vol. 4, pp. 518–520, May 1960.

[21] K. Ikeda, N. Takigawa, and H. Horiuchi, "The Systematic Structure-Change into the Molecule-like Structures in the Self-Conjugate 4n Nuclei," *Progress of Theoretical Physics Supplement*, vol. E68, pp. 464–475, 07 1968.

[22] M. G. Mazarakis and W. E. Stephens, "Experimental measurements of the $^{12}$C + $^{12}$C nuclear reactions at low energies," *Phys. Rev. C*, vol. 7, pp. 1280–1287, Apr 1973.

[23] M. High and B. Čujec, "The 12c + 12c sub-coulomb fusion cross section," *Nuclear Physics A*, vol. 282, no. 1, pp. 181–188, 1977.

[24] E. F. Aguilera, P. Rosales, E. Martinez-Quiroz, G. Murillo, M. Fernández, H. Berdejo, D. Lizcano, A. Gómez-Camacho, R. Policroniades, A. Varela, E. Moreno, E. Chávez, M. E. Ortíz, A. Huerta, T. Belyaeva, and M. Wiescher, "New $\gamma$-ray measurements for $^{12}$C +$^{12}$ C sub-coulomb fusion: Toward data unification," *Phys. Rev. C*, vol. 73, p. 064601, Jun 2006.

[25] R. A. Dayras, R. G. Stokstad, Z. E. Switkowski, and R. M. Wieland, "Gamma-ray yields from 12 C + 13 C reactions near and below the coulomb barrier," *Nucl. Phys. A*, vol. 265, pp. 153–188, 1976.

[26] M. Notani, P. Davies, B. Bucher, X. Fang, L. Lamm, C. Ma, E. Martin, W. Tan, X. Tang, S. Thomas, and C. Jiang, "Study of the hindrance effect in sub-barrier fusion reactions," *Nuclear Physics A*, vol. 834, no. 1, pp. 192c–194c, 2010. The 10th International Conference on Nucleus-Nucleus Collisions (NN2009).

[27] H. Esbensen, X. Tang, and C. L. Jiang, "Effects of mutual excitations in the fusion of carbon isotopes," *Phys. Rev. C*, vol. 84, p. 064613, Dec 2011.

[28] C. L. Jiang, B. B. Back, H. Esbensen, R. V. F. Janssens, K. E. Rehm, and R. J. Charity, "Origin and consequences of $^{12}$**C** +$^{12}$ **C** fusion resonances at deep subbarrier energies," *Phys. Rev. Lett.*, vol. 110, p. 072701, Feb 2013.

[29] C. Y. Wong, "Interaction barrier in charged-particle nuclear reactions," *Phys. Rev. Lett.*, vol. 31, pp. 766–769, Sep 1973.

[30] C. L. Jiang, K. E. Rehm, R. V. F. Janssens, H. Esbensen, I. Ahmad, B. B. Back, P. Collon, C. N. Davids, J. P. Greene, D. J. Henderson, G. Mukherjee, R. C. Pardo, M. Paul, T. O. Pennington, D. Seweryniak, S. Sinha, and Z. Zhou,

"Influence of nuclear structure on sub-barrier hindrance in Ni + Ni fusion," *Phys. Rev. Lett.*, vol. 93, p. 012701, Jun 2004.

[31] C. L. Jiang, H. Esbensen, B. B. Back, R. V. F. Janssens, and K. E. Rehm, "Analysis of heavy-ion fusion reactions at extreme sub-barrier energies," *Phys. Rev. C*, vol. 69, p. 014604, Jan 2004.

[32] i. m. c. Mişicu and H. Esbensen, "Hindrance of heavy-ion fusion due to nuclear incompressibility," *Phys. Rev. Lett.*, vol. 96, p. 112701, Mar 2006.

[33] C. Simenel, A. S. Umar, K. Godbey, M. Dasgupta, and D. J. Hinde, "How the pauli exclusion principle affects fusion of atomic nuclei," *Phys. Rev. C*, vol. 95, p. 031601, Mar 2017.

[34] K. A. Brueckner, J. R. Buchler, and M. M. Kelly, "New theoretical approach to nuclear heavy-ion scattering," *Phys. Rev.*, vol. 173, pp. 944–949, Sep 1968.

[35] K. Godbey, C. Simenel, and A. S. Umar, "Absence of hindrance in a microscopic $^{12}$C +$^{12}$ C fusion study," *Phys. Rev. C*, vol. 100, p. 024619, Aug 2019.

[36] C. L. Jiang, K. E. Rehm, B. B. Back, and R. V. F. Janssens, "Expectations for $^{12}$C and $^{16}$O induced fusion cross sections at energies of astrophysical interest," *Phys. Rev. C*, vol. 75, p. 015803, Jan 2007.

[37] G. Fruet, S. Courtin, M. Heine, D. G. Jenkins, P. Adsley, A. Brown, R. Canavan, W. N. Catford, E. Charon, D. Curien, S. Della Negra, J. Duprat, F. Hammache, J. Lesrel, G. Lotay, A. Meyer, D. Montanari, L. Morris, M. Moukaddam, J. Nippert, Z. Podolyák, P. H. Regan, I. Ribaud, M. Richer, M. Rudigier, R. Shearman, N. de Séréville, and C. Stodel, "Advances in the direct study of carbon burning in massive stars," *Phys. Rev. Lett.*, vol. 124, p. 192701, May 2020.

[38] P. J.R., W. H., and Z. C.S., "Experimental investigation of the stellar nuclear reaction 12c + 12c at low energies," *apj*, vol. 157, p. 367, jul 1969.

[39] C. L. Jiang, D. Santiago-Gonzalez, S. Almaraz-Calderon, K. E. Rehm, B. B. Back, K. Auranen, M. L. Avila, A. D. Ayangeakaa, S. Bottoni, M. P. Carpenter, C. Dickerson, B. DiGiovine, J. P. Greene, C. R. Hoffman, R. V. F. Janssens, B. P. Kay, S. A. Kuvin, T. Lauritsen, R. C. Pardo, J. Sethi, D. Seweryniak, R. Talwar, C. Ugalde, S. Zhu, D. Bourgin, S. Courtin, F. Haas, M. Heine, G. Fruet, D. Montanari, D. G. Jenkins, L. Morris, A. Lefebvre-Schuhl, M. Alcorta, X. Fang, X. D. Tang, B. Bucher, C. M. Deibel, and S. T. Marley, "Reaction rate for carbon burning in massive stars," *Phys. Rev. C*, vol. 97, p. 012801, Jan 2018.

[40] G. Fruet, *Structure des ions lourds et nucléosynthèse dans les étoiles massives : la réaction* $^{12}$C + $^{12}$C. PhD thesis, 2018. Thèse de doctorat dirigée par Courtin, Sandrine Physique Strasbourg 2018.

[41] "Bb10 detector design from micron semiconductor ltd." "http://www.micronsemiconductor.co.uk/product/bb10/.

[42] "Super x3 detector design from micron semiconductor ltd." "http://www.micronsemiconductor.co.uk/product/super-x3/.

[43] F. D. et. al *Nucl. Phys*, vol. 58, p. 145, 1963.

[44] "Uhv design ltd.." "https://www.uhvdesign.com/.

[45] G. Blondiaux, M. Valladon, L. Quaglia, G. Robaye, G. Weber, and J. Debrun, "Study of the growth of carbon on targets during ion bombardment," *Nuclear Instruments and Methods in Physics Research Section A: Accelerators, Spectrometers, Detectors and Associated Equipment*, vol. 227, no. 1, pp. 19–23, 1984.

[46] M. Healy, "Minimising carbon contamination during ion beam analysis," *Nuclear Instruments and Methods in Physics Research Section B: Beam Interactions with Materials and Atoms*, vol. 129, no. 1, pp. 130–136, 1997.

[47] M. J. Eller, E. Cottereau, B. Rasser, E. Verzeroli, B. Agnus, G. Gaubert, X. Donzel, A. Delobbe, and S. Della-Negra, "Andromede project: Surface analysis and modification with probes from hydrogen to nano-particles in the mev energy range," *Nuclear Instruments and Methods in Physics Research Section B: Beam Interactions with Materials and Atoms*, vol. 365, pp. 367–370, 2015.

[48] M. Rudigier, Z. Podolyák, P. Regan, A. Bruce, S. Lalkovski, R. Canavan, E. Gamba, O. Roberts, I. Burrows, D. Cullen, L. Fraile, L. Gerhard, J. Gerl, M. Gorska, A. Grant, J. Jolie, V. Karayonchev, N. Kurz, W. Korten, I. Lazarus, C. Nita, V. Pucknell, J.-M. Régis, H. Schaffner, J. Simpson, P. Singh, C. Townsley, J. Smith, and J. Vesic, "Fatima — fast timing array for despec at fair," *Nuclear Instruments and Methods in Physics Research Section A: Accelerators, Spectrometers, Detectors and Associated Equipment*, vol. 969, p. 163967, 2020.

[49] J. Chen, "Nuclear Data Sheets for A=138," *Nucl. Data Sheets*, vol. 146, pp. 1–386, 2017.

[50] B. Milbrath, R. Runkle, T. Hossbach, W. Kaye, E. Lepel, B. McDonald, and L. Smith, "Characterization of alpha contamination in lanthanum trichloride scintillators using coincidence measurements," *Nuclear Instruments and Methods in*

*Physics Research Section A: Accelerators, Spectrometers, Detectors and Associated Equipment*, vol. 547, no. 2, pp. 504–510, 2005.

[51] S. Agostinelli, J. Allison, K. Amako, J. Apostolakis, H. Araujo, P. Arce, M. Asai, D. Axen, S. Banerjee, G. Barrand, F. Behner, L. Bellagamba, J. Boudreau, L. Broglia, A. Brunengo, H. Burkhardt, S. Chauvie, J. Chuma, R. Chytracek, G. Cooperman, G. Cosmo, P. Degtyarenko, A. Dell'Acqua, G. Depaola, D. Dietrich, R. Enami, A. Feliciello, C. Ferguson, H. Fesefeldt, G. Folger, F. Foppiano, A. Forti, S. Garelli, S. Giani, R. Giannitrapani, D. Gibin, J. Gómez Cadenas, I. González, G. Gracia Abril, G. Greeniaus, W. Greiner, V. Grichine, A. Grossheim, S. Guatelli, P. Gumplinger, R. Hamatsu, K. Hashimoto, H. Hasui, A. Heikkinen, A. Howard, V. Ivanchenko, A. Johnson, F. Jones, J. Kallenbach, N. Kanaya, M. Kawabata, Y. Kawabata, M. Kawaguti, S. Kelner, P. Kent, A. Kimura, T. Kodama, R. Kokoulin, M. Kossov, H. Kurashige, E. Lamanna, T. Lampén, V. Lara, V. Lefebure, F. Lei, M. Liendl, W. Lockman, F. Longo, S. Magni, M. Maire, E. Medernach, K. Minamimoto, P. Mora de Freitas, Y. Morita, K. Murakami, M. Nagamatu, R. Nartallo, P. Nieminen, T. Nishimura, K. Ohtsubo, M. Okamura, S. O'Neale, Y. Oohata, K. Paech, J. Perl, A. Pfeiffer, M. Pia, F. Ranjard, A. Rybin, S. Sadilov, E. Di Salvo, G. Santin, T. Sasaki, N. Savvas, Y. Sawada, S. Scherer, S. Sei, V. Sirotenko, D. Smith, N. Starkov, H. Stoecker, J. Sulkimo, M. Takahata, S. Tanaka, E. Tcherniaev, E. Safai Tehrani, M. Tropeano, P. Truscott, H. Uno, L. Urban, P. Urban, M. Verderi, A. Walkden, W. Wander, H. Weber, J. Wellisch, T. Wenaus, D. Williams, D. Wright, T. Yamada, H. Yoshida, and D. Zschiesche, "Geant4—a simulation toolkit," *Nuclear Instruments and Methods in Physics Research Section A: Accelerators, Spectrometers, Detectors and Associated Equipment*, vol. 506, no. 3, pp. 250–303, 2003.

[52] "Photomultiplier scheme from wikipedia." "https://en.wikipedia.org/wiki/Photomultiplier_tube#/media/File:PhotoMultiplierTubeAndScintillator.svg.

[53] "Midas." "http://npg.dl.ac.uk/MIDAS/.

[54] M. Pesaresi, M. B. Marin, G. Hall, M. Hansen, G. Iles, A. Rose, F. Vasey, and P. Vichoudis, "The fc7 amc for generic daq and amp; control applications in cms," *Journal of Instrumentation*, vol. 10, p. C03036, mar 2015.

[55] V. T. Jordanov, G. F. Knoll, A. C. Huber, and J. A. Pantazis, "Digital techniques for real-time pulse shaping in radiation measurements," *Nuclear Instruments and Methods in Physics Research Section A: Accelerators, Spectrometers, Detectors and Associated Equipment*, vol. 353, no. 1, pp. 261–264, 1994.

[56] O. J. Roberts, A. M. Bruce, P. H. Regan, Z. Podolyák, C. M. Townsley, J. F. Smith, K. F. Mulholland, and A. Smith, "A LaBr 3 : Ce fast-timing array for DESPEC at FAIR," *Nucl. Instrum. Meth. A*, vol. 748, pp. 91–95, 2014.

[57] P. Regan, "Precision measurement of sub-nanosecond lifetimes of excited nuclear states using fast-timing coincidences with labr3(ce) detectors," *Radiation Physics and Chemistry*, vol. 116, pp. 38–42, 2015. Proceedings of the 9th International Topical Meeting on Industrial Radiation and Radioisotope Measurement Applications.

[58] M. Heine, S. Courtin, G. Fruet, D. Jenkins, D. Montanari, L. Morris, P. Regan, M. Rudigier, and D. Symochko, "Gamma efficiency simulations towards coincidence measurements for fusion cross sections," *Journal of Physics: Conference Series*, vol. 763, p. 012005, oct 2016.

[59] C. Rolfs. and W. Rodney, *Cauldrons in the Cosmos*. Univ of Chicago Press, 1988.

[60] W. P. Tan, A. Boeltzig, C. Dulal, R. J. deBoer, B. Frentz, S. Henderson, K. B. Howard, R. Kelmar, J. J. Kolata, J. Long, K. T. Macon, S. Moylan, G. F. Peaslee, M. Renaud, C. Seymour, G. Seymour, B. Vande Kolk, M. Wiescher, E. F. Aguilera, P. Amador-Valenzuela, D. Lizcano, and E. Martinez-Quiroz, "New measurement of $^{12}$C +$^{12}$ C fusion reaction at astrophysical energies," *Phys. Rev. Lett.*, vol. 124, p. 192702, May 2020.

[61] W. A. Fowler, G. R. Caughlan, and B. A. Zimmerman, "Thermonuclear reaction rates, ii," *Annual Review of Astronomy and Astrophysics*, vol. 13, no. 1, pp. 69–112, 1975.

[62] P. Eggenberger, R. Hirschi, G. Meynet, A. Maeder, R. Hirschi, C. Charbonnel, S. Talon, and S. Ekström, "The geneva stellar evolution code," *Astrophysics and Space Science*, vol. 316, 2008.

[63] M. Limongi and A. Chieffi, "Evolution, explosion, and nucleosynthesis of core-colapse supernovar," *The Astrophysical Journal*, vol. 592, pp. 404–433, Jul 2003.

[64] R. L. Cooper, A. W. Steiner, and E. F. Brown, "Possible resonances in the 12c + 12c fusion rate and superburst ignition," *The Astrophysical Journal*, vol. 702, p. 660, aug 2009.

Jean Nippert

# Quantum tunneling fusion reaction with impact on massive stars with STELLA


## Résumé

La mesure de la réaction de fusion $^{12}C$ + $^{12}C$ aux énergies astrophysiques est nécessaire pour bien appréhender l'évolution stellaire. D'une part, la suppression de la fusion a été observée dans la majorité des systèmes mi-lourds, mais des doutes subsistent pour les systèmes mi-légers. Dans le cas du $^{12}C$ + $^{12}C$, des indices de suppression de la fusion ont été obervées mais une confirmation claire est toujours attendue. D'autre part, la présence de résonances dans la section efficace de fusion est une forte indication d'états moléculaires dans le $^{24}Mg$. Ces résonances peuvent également avoir un impact conséquent sur notre compréhension de l'évolution stellaire. La mesure précise de la la fusion aux énergies profondément sous-coulombiennes est très complexe, car sa section efficace est sous le nanobarn et largement dominée par le bruit de fond. Pour surmonter ces difficultés, l'expérience STELLA (STELlar LAboratory) combinée à l'ensemble de détection UK-FATIMA (FAst TIMing Array) permet la mesure en coïncidences des gammas et des particules chargées produits par la réaction de fusion pour supprimer efficacement le bruit de fond et permettre la mesure précise aux énergies profondément sous-coulombiennes, dans la région en énergie d'intérêt astrophysique. La première campagne expérimentale de STELLA a révélé des indices de suppression de fusion ainsi qu'une potentiele résonance à basse énergie. Ce document présente les données de la campagne expérimentale de 2019. Des détails sur le contexte astrophysique de la fusion $^{12}C$+$^{12}C$ et de la structure nucléaire impliquée, ainsi que sur le système expérimental et l'analyse de donnée associée sont être présentés. Enfin, les résultats e tleur interprétation sont exposés



## Résumé en anglais

The measurement of the $^{12}C$ + $^{12}C$ fusion reaction at astrophysical energies is crutial to well understand massive stars evolution. One one hand, fusion hindrance has been observed in most of medium-heavy fusion systems, while is still unclear if it affects also light-medium fusion reactions. In the case of the $^{12}C$ + $^{12}C$ hints of hindrance have been observed around the predicted *S*-factor maximum with hindrance and still need a clear confirmation. On the other hand, the presence of resonances in the cross-section of $^{12}C$ + $^{12}C$ fusions reactions, that can be a strong indication of molecular states in $^{24}Mg$, can also have an impact on our understanding of stellar evolution. Precise measurements at deep sub-barrier energies are highly challenging, as the cross-section is in the sub-nanobarn range far below ambient background. To tackle this challenge, the STELLA (STELar LAboratory) experiment combined to UK-FATIMA (FAst TIMing Array) employs coincident measurement of gammas and charged particles products of the fusion reaction with nanoseconds timing to efficiently suppress the background and to take precise measurements at deep sub-Coulomb-barrier energy, right in the astrophysical region of interest. The first experimental campaign in 2016/2017 reavealed hints of hindrance and a potential resonance at low energy. This contribution will present data from an experimental campaign in 2019. Details on the astrophysical and nuclear structure context will be given as well as on the experimental setup and the data analysis, and exclusive *S*-factors will be presented and discussed in the context of the excitation function.